Doctoral theses at NTNU, 2021:94

Ahmad Shamsulizwan Bin Ismail

Modeling the dynamic evolution of drop size density distribution of the oil-water emulsion in turbulent pipe flow

Doctoral thesis

NTNU
Norwegian University of Science and Technology
Thesis for the Degree of
Philosophiae Doctor
Faculty of Natural Sciences
Department of Chemical Engineering

NTNU
Norwegian University of
Science and Technology

Ahmad Shamsulizwan Bin Ismail

Modeling the dynamic evolution of drop size density distribution of the oil-water emulsion in turbulent pipe flow

Thesis for the Degree of Philosophiae Doctor

Trondheim, March 2021

Norwegian University of Science and Technology
Faculty of Natural Sciences
Department of Chemical Engineering

NTNU
Norwegian University of
Science and Technology

NTNU
Norwegian University of Science and Technology

Thesis for the Degree of Philosophiae Doctor

Faculty of Natural Sciences
Department of Chemical Engineering

ISBN 978-82-326-5407-9 (printed ver.)
ISBN 978-82-326-5403-1 (electronic ver.)
ISSN 1503-8181 (printed ver.)
ISSN 2703-8084 (online ver.)

Doctoral theses at NTNU, 2021:94

Printed by NTNU Grafisk senter

Preface

This thesis is submitted in partial fulfilment of the requirements for the degree of Philosophiae Doctor (PhD) at the Norwegian University of Science and Technology (NTNU). This doctorial work has been performed at the Department of Chemical Engineering in the Faculty of Natural Sciences with Associate Professor Dr. Brian Arthur Grimes as supervisor and Professor Dr. Hugo Atle Jakobsen as the co-supervisor.

I completed my Master's degree in Engineering (Petroleum) with a research project on multiphase flow in pipeline at Universiti Teknologi Malaysia (UTM) in September 2014. I was accepted as the Ph.D. candidate in the chemical engineering department and carried out the Ph.D. work between March 2015 and April 2018. My PhD program is sponsored by the Ministry of Education (Malaysia) and Universiti Teknologi Malaysia (UTM).

Acknowledgement

First and foremost, I would like to thank God for the strengths, patience, endurance, and blessing upon me in completing this thesis. This project was not my effort alone but, several people have involved in making this project a success. In this opportunity, I would like to express my sincere gratitude and appreciation to my honourable supervisor, Associate Professor Dr. Brian Arthur Grimes for invaluable advices, excellent guidance and supervision, endless encouragement, constructive ideas, pedagogical excellence, and continuous support to ensure the success of this study. I am also very honoured and grateful to have Professor Dr. Hugo Atle Jakobsen as my co-supervisor, for his endless support and precious advices throughout my PhD studies.

Secondly, I would like to thank the Ministry of Higher Education of Malaysia for the sponsorship program of my PhD studies under the Skim Latihan Akademik Bumiputra (SLAB). I am also grateful to the Universiti Teknologi Malaysia (UTM) for their continuous and generous financial support throughout my PhD studies as well as giving me the opportunity to pursue my study abroad. Last but not least, my special thanks to the Department of Chemical Engineering, Norwegian University of Science and Technology (NTNU), particularly to the Head of Department, Professor Dr. Jens-Petter Andreassen for the additional financial assistance I received towards the end of my PhD studies.

Aside that, I am grateful to all the past and present students in the Colloid and Polymer Chemistry Research Group (Ugelstad Laboratory) for all the support, caring, and companion. In particular to my officemates, Dr. Sulalit Bandyopadhyay and Mr. Karthik Raghunathan as well as my former officemate Dr. Sirsha Putatunda and Dr. Gurvinder Singh, thank you for all the support, encouragements, motivation, scientific inputs, and words of wisdom. I enjoy all the time we spent together especially with my colleagues Dr. Sulalit and Dr. Sirsha who are now husband and wife. Thank you for being a constant source of help during the three and half years of my research and I hope our friendship remains. To my colleagues, Aleksandar Mehandzhiyski, Yuanwei Zhang, Eirik Helno, Muh Kurniawan, Ardi Hartono, Sreedhar, Mandar, Torstein, Greg, and to everyone else in the research group or in the department of chemical engineering, thanks a million for the fruitful and thoughtful discussions, impartial supports, kind assistances, excellent cooperation and invaluable

advices at various occasions either in programming, simulation, (Fortran or Matlab), or daily life experiences. Their views, tips, and contributions are truly useful and highly appreciated.

Finally, on my personal note, I would like to express my heartfelt appreciation to my dearly beloved wife, Ili Atiqah Abdul Wahab for her untiring support, unfailing love, and unconditional care and friendship during this toughest moment of my life. Without her I would not have the strength and perseverance in completing this study. Thank you for all the selfless and countless sacrifices you did during my pursuit of PhD degree that made the completion of this thesis possible. To my little caliph (son), Mohammad Adam Al-Thaqif, and to my little princess, Nur Aisyah Medina, I am truly sorry for not being able to accompany you both and witness your every step of growing up in the first three years of your life. You both have grown up watching me study and juggle with family and work. Thank you for cheering me up and being the joy of my life, and indeed, my love, my prayers and my longing for you both are beyond words. Most importantly to my beloved mother, Mrs. Chek Nah Bte Don for the prayers, words of wisdom, and unconditional support that always enlighten me and help me gaining my spiritual right on track and to my late father, Mr. Ismail, thank you for every support that you have given to me, without a doubt you are always in my heart and prayers forever. To all my family members: brothers, sisters, nieces, nephews, cousins, uncles, aunties, especially to my father in-law and mother in-law, Mr. Abdul Wahab and Mrs. Siti Rohayah, thank you for all the prayers and being extremely supportive.

Last but not least to Faheem and family, Rose Wollan and family, Romit, Rahman, and to all my fellow Malaysian in Trondheim either in past or present, Abu Ali, Siti Salwa and family, Liyana and family, Suriani, Albert Lau and wife, Jimmy Ting and family, Rais, Izzat, Faidzul, and others, thank you for helping me and my family to feel like home and settling down in the beautiful and serene city of Trondheim. With all the humility, I would like to thank them all for their noble gesture and splendid support during our time in Trondheim, Norway.

Abstract

The thesis presents a modelling approach to calculate and fit the evolution of the drop size distributions of oil and water emulsions under turbulent flow in pipes. A simulation model is developed to investigate coalescence and breakage phenomena of droplets in liquid-liquid dispersion over a long-distance pipeline under a fully dispersed flow regime and compared to experimental data to fit the model parameters. In this simulation work, the experimental data are supplied by Statoil. The experimental measurements took place at two different positions along the length of the pipeline using Focused Beam Reflectance Method (FBRM). The first location is at the inlet of the pipeline and the final location is near the outlet of the pipe. The mathematical model employed the population balance equation (PBE) approach to predict the volume and number density distribution functions, mean radii, standard deviations as well as breakage and coalescence rates over various distances in pipes. A new alternative solution to the complex PBE in the form of volume density distribution has been introduced using orthogonal collocation method for the case of fully developed turbulent oil-water pipe flow. Several breakage and coalescence models are assessed and compared in order to understand the behavior of the model. In addition, the model is also studied under various parametric effects particularly on dispersed volume fraction, ϕ and energy dissipation rate, ε. The study also involved minor modifications on the coalescence and breakage closures to account the correction factor of damping effect at high dispersed phase fraction, ϕ. The model employed the newly modified energy dissipation rate, ε by Jakobsen (2014) that considers the shear wall as the primary source of turbulence in pipes. The results showed that the model has successfully fitted the model proportionality constants accordingly at the final measurement locations (in good agreement with experimental data at final location). The regressed proportionality constants studied in the model did not vary significantly over the range of engineering parameters investigated.

List of manuscripts

(These manuscripts have been prepared for submissions to international peer-reviewed journal)

1st Manuscript

"Regression of Experimental Pipe Flow Data with Population Balance Modelling. Part I: Model formulations and solutions"

Ahmad Shamsul Izwan Ismail and Brian Arthur Grimes

2nd Manuscript

"Regression of Experimental Pipe Flow Data with Population Balance Modelling. Part II: Parametric Effects and Model Behaviour"

Ahmad Shamsul Izwan Ismail

3rd Manuscript

"Regression of Experimental Pipe Flow Data with Population Balance Modelling. Part III: Comparison to experimental of oil-water emulsions in turbulent pipe flow"

Ahmad Shamsul Izwan Ismail

Table of Contents

List of Tables

List of Figures

List of Symbols

D	Diameter of the pipe [m]
f_n	Number density distribution [m^{-3} m^{-1}]
f_v	Volume density distribution [m^{-1}]
g	Breakage frequency function for droplets [s^{-1}]
$\bar{g}$	Dimensionless breakage frequency function for droplets [-]
G_r	Growth rate [m^{-3} m^{-1} s^{-1}]
k_ω	Fitting parameter for coalescence frequency [-]
k_ψ	Fitting parameter for coalescence efficiency [-] and [m^2] for Coulaloglou and Tavlarides, (1977) model.
k_{g1}	Fitting parameter for breakage frequency [-]
k_{g2}	Fitting parameter for the exponential term of the breakage frequency function [-]
L	Length of the pipe [m]
N	Normalize number density distribution [-]
N_d	Total number density of droplets at any axial position, z in the pipe [m^{-3}]
M_B	Ratio of breakage mass balance [-]
M_C	Ratio of coalescence mass balance [-]
r_c	Rate of coalescence in volume [m^3 s^{-1}]
$\bar{r}_c$	Dimensionless rate of coalescence in volume [-]
r	Droplet radius [m]
r'	Radius of primary parent droplet [m]
r''	Radius of secondary parent droplet [m]
R_{C_b}	Coalescence rate of birth [m^{-3} m^{-1} s^{-1}]
R_{C_d}	Coalescence rate of loss [m^{-3} m^{-1} s^{-1}]

R_{B_b} Breakage rate of birth [m^{-3} m^{-1} s^{-1}]

R_{B_d} Breakage rate of loss [m^{-3} m^{-1} s^{-1}]

R_{max} Maximum droplet radius of the system [m]

Re_m Reynolds number of the mixture (oil and water) phase [-]

U Average velocity of the mixture fluid in pipe [m s^{-1}]

t Time [s]

v Volume of the droplet [m^3]

ν Kinematic viscosity [m^2 s^{-1}]

V_{max} Maximum drop volume from dimensionless formulation [m^3]

z Axial coordinate of the pipe [m]

Greek letters

α New coordinate system defined for coalescence birth integral in the simulation grid [-]

α_b New coordinate system defined for breakage birth integral in the simulation grid [-]

β Breakage size distribution function [m^{-1}]

$\bar{\beta}$ Dimensionless breakage size distribution function [-]

ξ Dimensionless droplet radius [-]

ε Energy dissipation rate [m^2 s^{-3}]

$\overline{f_n}$ Dimensionless number density distribution [-]

$\overline{f_v}$ Dimensionless volume density distribution [-]

$\bar{f}_{n_p}$ Dimensionless interpolated number density distribution [-]

$\overline{f_v}_p$ Dimensionless interpolated volume density distribution [-]

l_n Length of element defined for every spectral element, n in new coordinate system [-]

ϕ Local volume fraction at any axial position, z in the pipe [-]

ϕ_v Total volume density function at any axial position, z in the pipe [-]

ρ_c Density of the continuous phase [kg m^{-3}]

ρ_d Density of the dispersed phase [kg m^{-3}]

μ_c Viscosity of continuous phase [kg m^{-1} s^{-1}]

μ_d Viscosity of dispersed phase [kg m^{-1} s^{-1}]

μ_N Average radius of the number distribution in the pipe [m]

μ_V Average radius of the volume distribution in the pipe [m]

$\bar{\mu}_N$ Dimensionless average radius of the number distribution in the pipe [-]

$\bar{\mu}_V$ Dimensionless average radius of the volume distribution in the pipe [-]

σ_N Standard deviation of the number distribution in the pipe [µm]

σ_V Standard deviation of the volume distribution in the pipe [µm]

$\bar{\sigma}_N$ Dimensionless standard deviation of the number distribution in the pipe [-]

$\bar{\sigma}_V$ Dimensionless standard deviation of the volume distribution in the pipe [-]

σ Interfacial tension of the droplets [kg s^{-2}]

$\bar{v}$ Dimensionless drop volume [-]

ω_c Collision frequency function [m^3 s^{-1}]

$\bar{\omega}_c$ Dimensionless collision frequency function [-]

ψ_E Coalescence efficiency function [-]

$\bar{\psi}_e$ Dimensionless coalescence efficiency function [-]

λ Dimensionless axial coordinate in pipe [-]

Subscripts

0 denotes the initial condition

CHAPTER 1

1 INTRODUCTION

1.1 Motivation

Liquid-liquid dispersions are prevalent in many industrial processes particularly for transportation and production of petroleum fluids. When an oil-water mixture in pipes accelerates at high velocity and the relative motion becomes large enough, the flow inherently turns turbulent and the fluids undergo highly disordered motion characterized by velocity fluctuations and chaotic changes in pressure. These include the configurations of the pipe such as valves, pipe bends, fittings and chokes. The energy dissipated in such flows and pipe configurations lead to the formation of an emulsion where the one liquid phase is dispersed as droplets into the dominant liquid called continuous phase. In this respect, the droplets from the dispersed phase undergo continuous oscillations from the turbulent eddies by the dynamic process occurring within the system. Depending on the physicochemical properties of the oil and water as well as the relative volumes ratios, the oil-water mixture can be in the form of water-in-oil emulsion (w/o) or oil-in-water emulsion (o/w) as illustrated in Fig. 1.1, and is also encountered in the petroleum industry with applications at many stages in terms of petroleum recovery, transportation, and processing (Becher 2001, Schramm 1992). The type of oil-in-water emulsion (w/o) flow is favorable in the case of heavy crude oil transportation due to the fact that water continuous emulsions should have a low viscosity compared to the heavy crude oils.

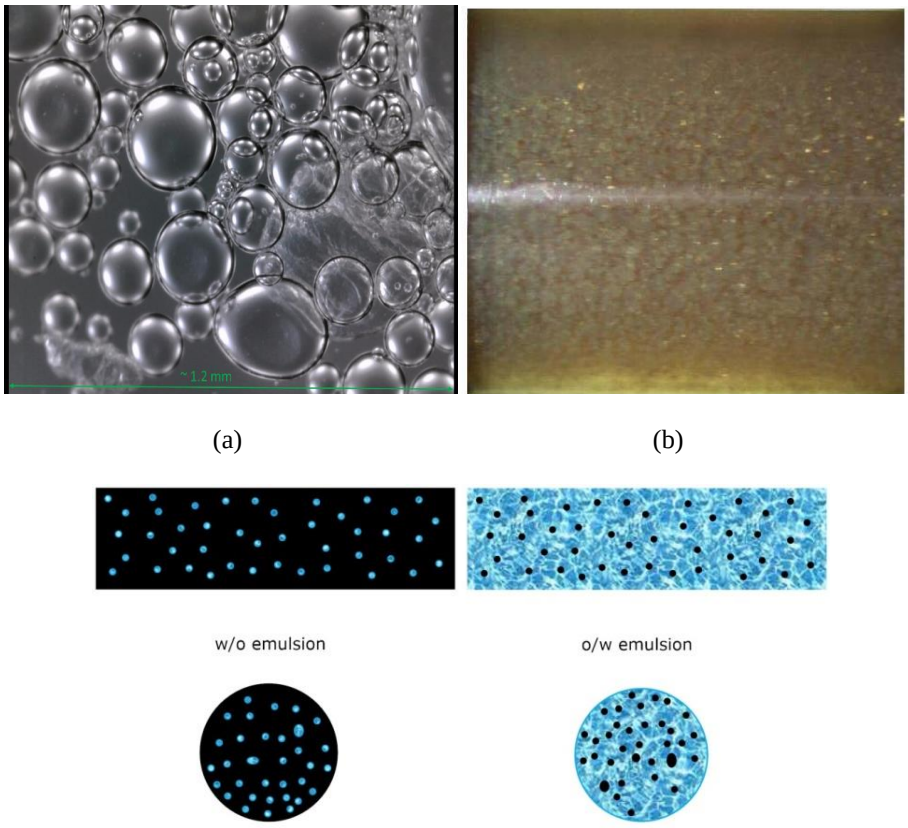

Figure 1.1 Images of oil-water mixture (a) water-in-oil emulsion, w/o under microscopic image by Gavrielatos et al., (2017), (b) oil-in-water emulsion, o/w in pipe flow by Vuong et al., (2009) and (c) typical structures for respective emulsion.

The properties of a dispersion of oil and water mixture in two phase turbulent flow are associated with the drop size distribution. In general, the drop size distribution defines the interfacial area, which has a major influence on mass and/or heat transfer rates between one or more phases (Hesketh et al., 1991; Luo and Sevendsen, 1996). In pipe flow, the drop size distribution can greatly influence the rheological behaviour of the emulsions and the flow properties such as the effective viscosity, pressure gradient and the holdup fraction of the

mixture liquids (Arirachakaran et al., 1989; Schümann, 2016). Hence, a detailed and properly parameterized model that can provide accurate predictions of the dynamic evolution of the drop size distribution of oil-water emulsion could be valuable for production optimization, particularly in the design of critical equipment such as multiphase separators and transport pipelines. Although there have been a plethora of studies on liquid-liquid dispersion from theoretical to experimental over the past years (Solsvik et al., 2015; Maaß et al., 2011; Raikar et al., 2010; Maaß and Kraume, 2012; Vankova et al., 2007; Alopaeus et al., 2002; Alopaeus et al., 1999; Chen et al., 1998; Chesters, 1991; Luo and Sevendsen, 1996; Nere and Ramkrishna, 2005; Coulaloglou and Tavlarides, 1977; Hsia and Tavlarides, 1980), the topic still remains one of the difficult and least understood mixing problems in turbulent flow (Azizi and Al Taweel, 2011; Kostoglou and Karabelas, 2007). In this respect, any small changes in the chemical composition of the system will greatly affect its performance (Paul et al., 2004). A majority of the research work on drop behaviour modelling for liquid-liquid systems were found to be focused on stirred tank and gas column, compared to liquid-liquid pipe flow which has significant differences in parametric effects, geometrical setup, and physical configurations. One of the notable differences is the formation of the turbulent energy. For instance, in the stirred tank setup, the turbulent is uniformly distributed to the fluids by the static mixing element. However, in the pipe flow the turbulent is formed due to continuous oscillation (the energy is primarily supplied by the pumps) of the liquid phases (oil and water). Furthermore, turbulent disperse systems involve numerous parameters including hydrodynamics, turbulence, and physiochemical effects (Briceño et al., 2001). Besides that, liquid-liquid system has a relatively small density ratio between the phases as compared to gas-liquid system. Therefore, the various concepts and results related to gas-liquid flows such as prediction of pressure drop cannot be simply or readily applied to liquid-liquid systems.

From the complexity of the problem as aforementioned, a detailed understanding and accurate knowledge are needed in order to predict the dynamic evolution of the drop size distribution in turbulent pipe flow. There is a significant relevance in applications such as designing the nuclear reactors, chemical reactors, multiphase separators, oil sand extraction and processing, water and wastewater treatment (Liao and Lucas, 2010; Azizi and Al Taweel, 2010). These have been the driving force behind the extensive research work on the understanding of droplets behaviour. Therefore, theoretical study has been conducted to investigate the droplet size behaviour under the liquid-liquid fully dispersed flow in isotropic turbulence in the fully dissipative regime. In this study, the experimental pipe flow data are supplied by Statoil. They employed the method of Focused Beam Reflectance Measurement (FBRM) at two different positions of measurement along the length of the pipeline to acquire the drop size distributions. The first location is at the inlet of the pipeline and the final location is near the outlet of the pipe. Three different data sets of drop size distributions are collected at various velocities (detailed in section 3). In this present work, to determine the drop size distribution two major events named coalescence and breakage are studied. Both the processes of drop coalescence and breakage profoundly influence the dynamic evolution of drop sizes. Hence, it is essential to accurately characterize and choose breakage and coalescence models that best represent the behavior of petroleum emulsions. One of the suitable methods to predict the dynamic evolution of drop density distribution in turbulent pipe flow is using the population balance equation (PBE) approach. PBE is a rigorous mathematical framework that employs a physical description of the two drop processes from breakage due to flow field and coalescence due to collisions in terms of various physical parameters and operating conditions and provides the evolution of the drop size distribution with time and space. However, the solution of a PBE model can be a challenge and often complicated due to the large number of equations involved, numerical complications,

accuracy of the system, computational efforts and/or efficiency, mechanisms governing the drop size evolution in liquid-liquid dispersions, and inclusion of particle growth due to breakage and coalescence events (Pinar et al., 2015; Rehman and Qamar, 2014; Korovessi and Linninger, 2004; Gunawan et al., 2004; Alexopoulos et al., 2004; Sing and Ramkrishna, 1977). Hence, to address these issues, a new possible methodology is proposed to solve the PBE. The methods have been discussed thoroughly in the next chapters of this thesis (see Chapter 3). Minor modification for several breakage and coalescence kernels are also implemented to account for high volume fraction (dispersed phase). The system equation in this present work is formulated in terms of volume density distribution instead of number density distribution that allows the model to have a stable magnitude over time and consistent convergence criterion in numerical calculations. Finally, the model formulations are compared with experimental data under different breakage and coalescence models. Following the research strategy, the objectives of this research work are focused on three aspects as follows:

1.2 Objectives of the research

1) To propose new alternative solution method to the PBE and discuss possible breakage and coalescence models for the dynamic evolution of drop size density distribution of the oil-water emulsions in turbulent pipe flow. The study includes model formulation and numerical solution for the PBE.
2) To study the various parametric effects and interplay on the evolution of the drop density distribution functions in turbulently flowing liquid-liquid emulsions. The parameters investigated include volume fraction of the dispersed phase, ϕ, the energy dissipation rate, ε, the pipe length, L, and all four fitting parameters, k_{ω}, k_{ψ}, k_{g_1}, and k_{g_2}.

3) To compare the model formulated with the experimental results (regression analysis) obtained for oil-water emulsion in turbulent pipe flow as well as to compare the applicability of various coalescence and breakage models.

1.3 Scopes of the research

The study is focused on formulating a model to describe the evolution of the drop size distribution of a liquid-liquid emulsion under turbulent pipe flow over long distances. The model is built upon population balance equation breakage and coalescence into account. Comparing the performance of various coalescence and breakage models against experimental data could allow us to predict and fit the drop distribution for long distance emulsion transport. The model is formulated to simulate: (i) the evolution of number and volume density distributions, (ii) the average radii of number and volume distributions, (iii) standard deviations of the number and volume density distributions, (iv) the length and time to establish equilibrium between coalescence to breakage, (v) the evolution of breakage and coalescence in terms of birth and death rates, and (vi) regression (fit) on final volume density distribution. Apart from that, in order to formulate the model and reduce the amount of computational efforts, certain simplifications are necessary to make the problem tractable. Some conditions have to be assumed such as isotropic turbulent and the droplet size is within the inertial subrange eddies $l_e \geq 2r \geq \eta$ (i.e., l_e is the integral length scale for large eddies and η is the Kolmogorov scale for small eddies). In this case, the viscous effect is negligible, and deformation of drops occurs primarily from turbulent fluctuations. Other assumptions made are written in details in chapter 3 of this thesis (research methodology).

1.4 Outline of the thesis

This thesis is written in the form of monograph with a detailed description on every topic and consists of extended theoretical part to provide an overview and comprehensive knowledge of the topic. It is organized in various chapters as follows:

Chapter 1 introduces the topic and provides an overview of liquid-liquid dispersions which include the objectives and scope of the research work. Chapter 2 discusses the important literature on coalescence and breakage models in detail. In Chapter 3, the proposed method to solve this problem is discussed and presented. The results and findings are discussed in Chapter 4 and Chapter 5. The conclusion is written in Chapter 6 and finally, the recommendations for future work is addressed Chapter 7.

1.5 Chapter summary

This chapter provides a description and overview of the research project on drop size density distribution in turbulent liquid-liquid flow, the challenges or problems encountered in liquid-liquid dispersion system, the significances and importance of the research work (i.e., the relevant applications). A new possible solution method for complex PBE in a fully developed oil-water turbulent pipe flow is proposed. To address these issues the objectives and scopes of the research were outlined. The details of the literature review and theory are discussed in the following section of Chapter 2.

CHAPTER 2

2 BACKGROUND

2.1 Oil-water emulsion in turbulent pipe flow

The turbulent flow of oil and water is considered a ubiquitous and inherent phenomenon in many natural and industrial processes, particularly during the production or transportation of petroleum fluids. At high shear rate, the fluids undergo highly disordered motion characterized by velocity fluctuations and chaotic changes in pressure. Under such circumstances, emulsions of oil and water appear where droplets from one liquid disperse into another liquid phase. The formation of emulsions is influenced by many factors namely, interfacial tension between liquids, shear and geometrical properties of liquids (Schümann, 2016). From the phenomenon known as phase inversion, the emulsion can be found in the form of oil-in-water (o/w) or water-in-oil (w/o) depending on various parameters such as volume fraction, pH and salinity, viscosities of fluids, interfacial compositions and turbulence (Piela et al., 2006). In general, droplets form as a result of instability at the interface between the liquids mixture due to continuous oscillations in the flow. Figure 2.1 shows the types of flow patterns in pipelines in the case of laminar (Fig.2.1a) and turbulent dispersed flows (Fig.2.1b). As a result of intense turbulent kinetic energy, the oil phase begins to detach from its surface forming small droplets and are dragged by the continuous phase (water) in the pipe as shown in Fig. 2.1. In the petroleum industry, for certain operations, emulsions are required during the drilling assignments in order to lift the drill cuttings to the surface as well as better hole cleaning (Werner et al., 2017). But in some situations, such as during the petroleum recovery process, emulsions are unwanted because they can accumulate and plug the pipelines as well as the production well-head. In the case of heavy crude oils, the high

viscosity hinders the efficient transportation of the fluids through pipelines to surface facilities (Hart, 2014). Hence, reducing the viscosity is the best alternative or having the type of oil-in-water (o/w) emulsion in oil-water pipe flow is preferable because it could reduce the pumping requirements as o/w emulsion could have lower viscosity than the heavy crude.

(a) (b)

Figure 2.1 Example of oil-water flow behaviour in a pipeline (a) under laminar flow (b) under dispersed flow (Ismail et al., 2015a)

The drop size distribution from the liquid-liquid dispersions is important for characterizing the emulsions (Chen et al., 1998). According to Opedal et al., 2009 and Otsubo and Prud'homme, 1994, the drop size distribution affects the rheology and the stability of the emulsion. In an experimental investigation by Pal, (1996), he observed that the effective viscosity increases as the droplet sizes reduce for both oil-in-water (o/w) as well as water-in-oil emulsions (w/o). In pipe flow for instance, the drop size distribution significantly affects the rheological behaviour and the pressure gradient of the liquids as reported by Arirachakaran et al., (1989) in their analysis of oil-water flow phenomena in horizontal pipes. Angeli and Hewitt, (1999) also discovered that the droplet size affects the drag reduction in oil-water flow due to turbulent fluctuations in the pipes. Therefore, an experimentally validated theoretical model for emulsion drop size of liquid-liquid dispersions is crucial due

to its significant effects and contributions particularly on processes related to transport and separation of liquid-liquid dispersions (Schümann, 2016).

2.2 Population balance equation (PBE)

One of the preferred methods to predict the drops evolution of oil-water emulsions under turbulent flow regime is using the population balance equation (PBE) approach. PBE is a useful tool that takes into account the processes from breakage due to the flow field, and coalescence due to collisions. The PBE method is generally applicable to particle growth processes such as crystallization, precipitation, flocculation, cell growth, mixing, multiphase flow, reaction etc. as reported in review article by Ramkrishna and Singh, (2014). The work on population balance was started as early as 1917 by von Smoluchowski who studied a poly-dispersed particle dynamic. von Smoluchowski (1917) is considered the pioneer in deriving aggregation kernel from Brownian motion and has proposed a set of nonlinear differential equation for the aggregation of particles (Solsvik and Jakobsen, 2015; Ramkrishna and Singh, 2014). However, the works on population balance have been widely considered to have been derived simultaneously by Hulburt and Katz (1964) along with Randolph (1964). Both have suggested a generic expression for the population balance in terms of integro-differential equations for the number density of the particles in the phase space. Hulburt and Katz (1964) introduced population balance equation as a tool to model liquid-liquid dispersions. They developed a model that used differential equations to show the variation of particle sizes in the dispersed flow system. Later, Coulaloglou and Tavlarides (1977) employed the model established by Hulburt and Katz (1964) and developed an improved set of breakage and coalescence models under turbulent flow field for liquid-liquid dispersion. Since then, there have been numerous studies and discussions on the population balance equations as reported comprehensively in review article by Jakobsen, (2008); Solsvik and Jakobsen (2015); Liao

and Lucas (2009, 2010); Abidin et al., (2015); Deju et al., (2015); Sajjadi et al., (2013); Rigopoulos, (2010); and Omar and Rohani, (2017).

A vector is used to describe these changes in the system of states during the particle interactions (Ramkrishna and Singh, 2014) or also known as particle phase space by Solsvik and Jakobsen, (2015). The vector is composed of internal coordinates that indicate the properties concerning the particle such as the particle charge, lifetime, or size (i.e., radius, diameter, volume, and mass) and the external coordinates, representing the physical spatial location of the particle. In a nutshell, the phase space vector consists of location and property spaces of the particle. The PBE also accounts for the birth and death of the particle during either coalescence or breakage processes as well as provides the evolution of the drop size distribution with time and space. It is important to take into account the breakage and coalescence processes during the dispersion of liquid-liquid flow because the final drop sizes distributions are produced from the competition between both processes (DeRoussel et al., 2001). Normally, PBEs are solved via numerical or statistical methods (Abidin et al., 2015). There are several numerical solutions techniques proposed to solve the PBE in literature and the most common methods used are finite difference method, weighted residuals method, discretization techniques, and Monte Carlo (Mesbah et al., 2009). Generally, PBE formulations are derived from the concept of Boltzman transport equation, continuum mechanical principles, and probability principles (Liao and Lucas, 2009; Solsvik and Jakobsen, 2015; Randolph and Larson, 1988). PBE can be illustrated as particles entering and leaving a control volume and those accumulating within it are balanced. According to Vennerker et al., (2002), the general form of population balance equation from Ramkrishna (1985) can be written as:

$$\frac{\partial f_n(\boldsymbol{z},\boldsymbol{r},t)}{\partial t} + \nabla_z . \dot{\boldsymbol{z}} f_n(\boldsymbol{z},\boldsymbol{r},t) + \nabla_r . \boldsymbol{u} f_n(\boldsymbol{z},\boldsymbol{r},t) = S(\boldsymbol{z},\boldsymbol{r},t) \tag{2.1}$$

Where, $f_n(\boldsymbol{z},\boldsymbol{r},t)$ is the number density distribution function that represents the number of fluid particles per unit volume as a function of property vector $\boldsymbol{z}$ (internal coordinate) and physical position of the particle $\boldsymbol{r}$ (external coordinate) with time, t**.** The terms $\dot{\boldsymbol{z}}$ and $\boldsymbol{u}$ are growth rate and velocity of the particle respectively. While, $S(\boldsymbol{z},\boldsymbol{r},t)$ is the generalized source term for birth and death of particle due to coalescence and breakage processes and can be expressed as follows:

$$S(\boldsymbol{z},\boldsymbol{r},t) = B(\boldsymbol{z},\boldsymbol{r},t) - D(\boldsymbol{z},\boldsymbol{r},t) \tag{2.2}$$

In Eqn. (2.2), the two terms on the right-hand side represent the birth and death rates of particles at particular state $(\boldsymbol{z},\boldsymbol{r})$ at time t. The birth rate $B(\boldsymbol{z},\boldsymbol{r},t)$ is the number of droplets formed from breakage of larger droplets or coalescence of smaller droplets. The death rate $D(\boldsymbol{z},\boldsymbol{r},t)$ is the number of droplets that breakup into smaller drops and small drops that coalesce into larger drops. The birth and death processes from coalescence and breakage are illustrated in Fig. 2.2. The mechanistic derivation of the PBE source term $S(\boldsymbol{z},\boldsymbol{r},t)$ is explained in detailed by Solsvik and Jakobsen, (2015). By substituting Eqn. (2.2) into the generalized PBE equation in Eqn. (2.1) and becomes:

$$\frac{\partial f_n(\boldsymbol{z},\boldsymbol{r},t)}{\partial t} + \nabla_z.\dot{\boldsymbol{z}}f_n(\boldsymbol{z},\boldsymbol{r},t) + \nabla_r.\boldsymbol{u}f_n(\boldsymbol{z},\boldsymbol{r},t) = B(\boldsymbol{z},\boldsymbol{r},t) - D(\boldsymbol{z},\boldsymbol{r},t) \tag{2.3}$$

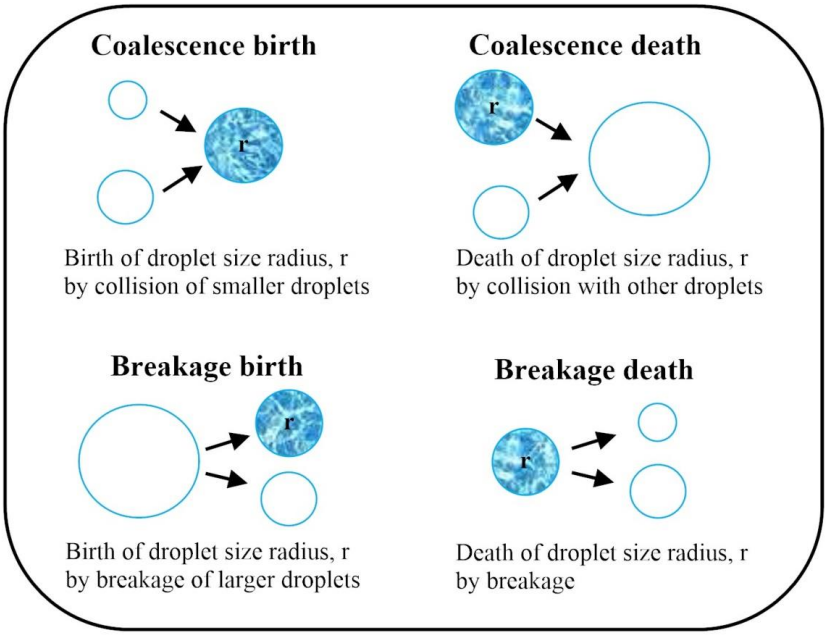

Figure 2.2 Illustration of birth and death processes due to breakage and coalescence

The PBE model requires appropriate functions to describe the breakage and coalescence phenomena. Presently, there are numerous models proposed in the literature on drop size predictions in turbulent flow, many of which have been discussed thoroughly in the review article by Liao and Lucas, (2009 and 2010), Abidin et al., (2015), Solsvik et al., (2013), Sajjadi et al., (2013) and Deju et al., (2015). The functions are developed based on four specific requirements namely breakage rate, daughter size distribution, collision frequency, and coalescence efficiency. Several of the breakage and coalescence models are discussed in the following sections.

2.3 Review of breakage models

Normally, breakage occurs when turbulent fluctuations from the flow force the particle in the dispersed phase to breakup, although, more precisely, the turbulent kinetic energy is said to have exceeded the surface energy of the droplet. In this respect, the surface of the particle is exposed to the "bombardment" of eddies promoting instabilities and eventually causing the droplet to deform (split). Extensive effort has been spent in developing the model for breakage process. Among the earliest studies on this subject are the ones by Valentas et al., (1966) and Narsimhan et al., (1979). Valentas et al., (1966) developed an empirical model for a specific drop breakage, while Narsimhan et al., (1979) proposed a binary drop breakage that accounts for the number of eddies arriving with different scales at the surface of the droplet.

There are several models introduced to elucidate the drop breakage in literature, with particular attention to the model developed by Coulaloglu and Tavlarides (1977). They proposed a phenomenological model in the population balance equation to describe the breakage process based on drop formation and breakup under the influence of local pressure fluctuations in a locally turbulent isotropic field. They assumed that the droplet sizes are within the inertial subrange and the breakup will take place if the turbulent kinetic energy transmitted from collision of eddies is greater than the surface energy of the droplets that keeps them physically intact. The breakup process in PBE can be described using two terms namely breakage frequency, $g(r)$ and daughter size distribution (probability of droplets formed after breakup). Detailed descriptions of both terms are elucidated in the following sections.

2.3.1 Breakage frequency functions, $g(r)$

There are a number of mechanisms proposed in literature to elucidate the breakage process. In general, the breakage mechanisms can be classified into four categories as follows:

(i) Breakup of droplet due to turbulent fluctuations.

(ii) Breakup of droplet due to viscous shear stress.

(iii) Breakup of droplet due to shearing off process.

(iv) Breakup of droplets due to interfacial instabilities.

Typically, the breakage frequency functions available in literature are developed based on these four suggested mechanisms. Fig. 2.3 shows the illustrations for each of the mechanisms that contribute to droplet breakup or deformation process (Liao et al., 2015). The most popular and preferred mechanism is from turbulent fluctuations where more work is found to be based on this mechanism as shown in the model classification flow chart in Fig. 2.4.

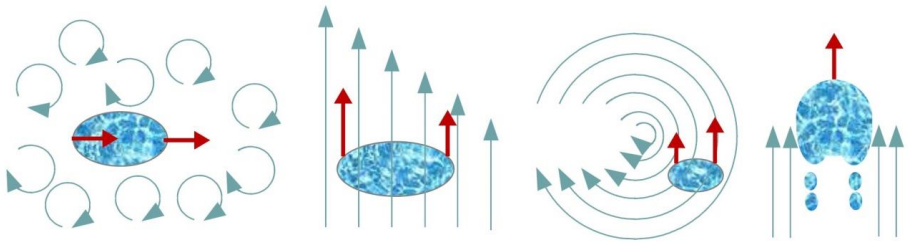

(a) (b) (c) (d)

Figure 2.3 Type of mechanisms that promote the breakup and rupture of droplets: (a) breakup due turbulent fluctuations, (b) breakup due to viscous shear force, (c) breakup due to shearing-off process, and (d) breakup due to interfacial instabilities (Liao et al., 2015).

2.3.1.1 Breakup of droplets due to turbulent fluctuations

In this type of mechanism, the breakup of droplet is assumed to occur when there is an imbalance between the dynamic forces (turbulent pressure fluctuations) and surface stresses (surface energy) of the droplets. Based on this assumption, several criteria have been proposed in the literature as follows:

- Turbulent kinetic energy being greater than surface energy
- Velocity fluctuation across the surface of the droplet
- Turbulent kinetic energy from fluctuating eddies being greater than surface energy
- Inertial force of the fluctuating eddies

The details of these criteria have been discussed in depth by Liao and Lucas, (2009), Abidin et al., (2015), Solsvik et al., (2013) and Solsvik et al., (2014). Nevertheless, the pioneer of the breakup model based on the criteria of turbulent kinetic energy being greater than surface energy was proposed by Coulaloglou and Tavlarides (1977) and the model has been widely used in literature. The criteria postulated that when the turbulent kinetic energy supplied from turbulent eddies is large enough to overcome the critical value owned by each individual droplet (the critical value in this context refers to the surface energy of the droplet). Hence, the chaotic changes in velocity manifest the turbulent fluctuations and eventually promote the particle-eddy collisions along the surface of the droplet. The continuous process of turbulent fluctuations caused the droplet surface to become unstable. At higher oscillations, the process leads to elongation and rupture of droplet into two or more daughter droplets. Hence, from the assumptions discussed above, Coulaloglou and Tavlarides (1977) formulated the drop breakage function as follows:

$$g(r) = \left(\frac{1}{breakage\ time}\right)\left(\begin{matrix} fraction\ of \\ drops\ breaking \end{matrix}\right) \approx \frac{1}{t_b} exp\left(-\frac{E_\sigma}{E_k}\right) \tag{2.4}$$

Where, t_b denotes the breakage time, E_σ and E_k are the drop surface energy and kinetic energy respectively. However, Lasheras et al., (2002) disagreed in general with the breakage efficiency (the exponential term as shown in Table 2.1) proposed by Coulaloglou and Tavlarides (1977) as they suggested that the breakup should be dependent more on continuous phase density, ρ_c. Vankova et al., (2007) has extended the model by Coulaloglou and Tavlarides (1977) and proposed drop breakage characterized by drop Reynolds number (Re_d) that accounts for both continuous phase density, ρ_c and dispersed phase density, ρ_d.

2.3.1.2 Breakup of droplets due to viscous shear stress

In this mechanism, the breakup of bubbles is assumed to occur when there is an imbalance of forces between the external viscous stresses from the continuous fluid and surface stresses of the droplets in the air-water mixture. In this respect, the viscous shear stress from continuous fluid induced by the velocity gradient across the interface of the droplet ultimately leads to droplet deformation. However, the deformation of the droplet is based on the force balance characterized by the Capillary number, Ca. If Ca is large enough and above the critical value, the interfacial forces can no longer hold the particle intact and eventually break the droplet into two or more daughter droplets.

2.3.1.3 Breakup of droplets due to shearing off process

In this mechanism, the breakage (erosive breakage) is assumed to occur when the small bubbles are sheared off from the larger bubbles (Liao and Lucas, 2009). This process is characterized by the imbalance of forces between the viscous shear force and surface tension at skirts of the cap/slug bubble. For instance, in the case of viscous gas-liquid in turbulent flows, the high relative velocity induces the bubble skirts to become unstable and disintegrates them from larger droplets. This leads to generation of large number of small

droplets at the rim (i.e., boundary). The velocity difference around the interface of the particle is the major contribution of this process (Fu and Isshi, 2002). Nevertheless, this mechanism is the major concern only in case of air-water mixtures (gas-liquid flows) and was found to be limited in the literature compared to turbulent fluctuations and viscous shear stress (Yeoh et al., 2014).

2.3.1.4 Breakup of droplets due to interfacial instabilities

In this mechanism, the breakage is assumed to occur without the presence of net flow where continuous fluid characteristics are insignificant. According to Liao and Lucas (2009) and Solsvik et al., (2013 and 2014), breakage can still take place in a motionless liquid for instance, the rise and fall of bubbles in continuous gas or immiscible liquids due to the interfacial instabilities. This can be expressed in Rayleigh-Taylor instability wherein the low-density fluid travels rapidly into a high-density fluid. In the case of density ratio approaching unity, the breakage process is taking the Kelvin-Helmholtz instability.

Several models of breakage frequency functions $g(d)$ are derived from four different criteria or mechanisms (see section 2.3.1.1) for droplets break process. For instance, Coulaloglou and Tavlarides (1977) proposed a model for breakage frequency function mainly on turbulent fluctuations. They assumed breakage rate to be a product of the fraction of breaking drops and the reciprocal time needed for the drop breakup to occur as a result of collision with turbulent eddy. They further added the factor of $(1 + \phi)$ to account for the damping effects on the local turbulent intensities at high hold up fractions. Chen et al. (1998) introduced a mechanistic model for breakage rate function that accounts for interfacial tension and viscosity. They also employed the effect of turbulent intensities at high holdup fraction as suggested earlier by Coulaloglou and Tavlarides (1977). Rather simplistic, Cristini et al., (2003) introduced a direct proportionality model or linear dependence based on sub-

Kolmogorov drops in terms of drop volume(v), $g(v) \approx kv$. Some of the breakage frequency models in the literature are described in the Table 2.1. Majority of the proposed breakage models are found to neglect the correction factor for dampening of turbulent intensities at high dispersed phase fraction $(1 + \phi)$ as suggested by Coulaloglou and Tavlarides (1977).

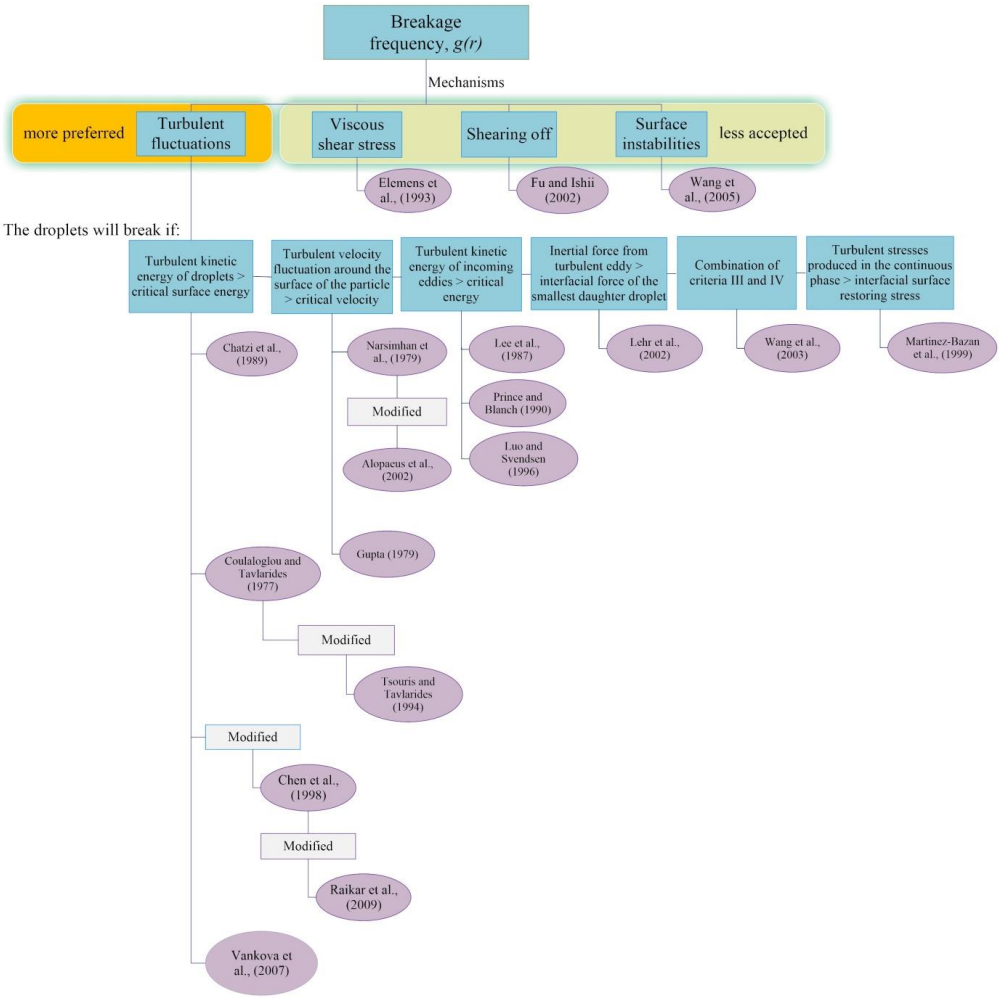

Figure 2.4 Mechanisms for breakage frequency

Table 2.1 Breakage frequency functions, $g(r)$

Authors	**Breakage frequency (rate) functions, $g(r)$**	**Assessments of the model**
Coulaloglou and Tavlarides, (1977)	$g(r) = k_{g_1} \frac{\varepsilon^{1/3}}{r^{2/3}(1+\phi)} \exp\left[-k_{g_2} \frac{\sigma(1+\phi)^2}{\rho_d \varepsilon^{2/3} r^{5/3}}\right]$	Predicts maximum drop breakage frequency as the drop diameter increases. Developed based on mechanism of turbulent fluctuations and damping effect $(1+\phi)$ for a liquid-liquid system with high dispersed fraction. The experimental data are correlated satisfactorily with the addition of damping factor in the breakage model. However, for gas-liquid system, this breakage model predicts breakup rate lower than experimental results (Prince and Blanch 1990). This is due to the fact that, in gas-liquid mixture, the density is lower than the density of liquid-liquid dispersions. Hence, density (ρ_d) in the breakage model should be replaced by density of continuous phase, ρ_c
Chen et al., (1998)	$g(r) = k_{g_1} \exp\left[-\frac{k_{g_2}\sigma(1+\phi)^2}{\rho_d r^{5/3} \varepsilon^{2/3}} - \frac{k_{g_3}\mu_d(1+\phi)}{\rho_d r^{4/3}\varepsilon^{1/3}}\right]$	Mechanistic model which incorporates interfacial tension, dispersed density and viscosity. The model is a function of local energy per unit mass. This model considers the viscous effect and surface energy in breakup frequency of droplets.

		In this premise, a fluid with high viscosity will be subjected to deformation and stretch as internal viscous force of the droplet increases which results in thin liquid formation until it reaches a critical thickness before breaking/splitting and producing more smaller droplets (Andersson and Andersson, 2006). The breakage time is assumed to be constant ($1/t_B = k_{g_1}$).
Alopaeus et al., (2002)	$g(r) = k_{g_1}\varepsilon^{1/3}\,\mathrm{ercf}\left(\sqrt{\frac{k_{g_2}\sigma(1+\phi)^2}{\rho_c r^{5/3}\varepsilon^{2/3}} + \frac{k_{g_3}\mu_d(1+\phi)}{\sqrt{\rho_c\rho_d}\,r^{4/3}\varepsilon^{1/3}}}\right)$	Accounts for damping effect at high phase fraction $(1+\phi)$ as suggested by Coulaloglou and Tavlarides, (1977). The model is developed based on the concept of velocity fluctuation theory. The model is the modification from the work of Narsimhan et al. (1979). They have added the drop breakage model by accounting the dependency on dissipation rate and viscous force which has been neglected in most previous work (Liao and Lucas, 2009). The effect of the drop breakup will depend on the magnitude of the surface tension and dispersed phase viscosity as well as the fitting parameters, k_{g_1}, k_{g_2} and k_{g_3}.

Luo and Svendsen, (1996)	$g(r)$ $= k(1-\phi)\left(\frac{\varepsilon}{2r^2}\right)^{1/3} \int_{\xi_{min}}^{1} \frac{(1+\xi)^2}{\xi^{11/3}} \exp\left(-\frac{12 c_f \sigma}{\beta \rho_c \varepsilon^{2/3} r^{5/3} \xi^{11/3}}\right) d\xi$ Where, $k = \frac{15\pi^{1/3}}{8 \times 2^{2/3} \Gamma(1/3)} \beta^{1/2}$	The model is derived based on extension of the classical kinetic theory of gases. The model assumes that the turbulence consists of an array of discrete eddies. The model does not predict a maximum breakage frequency due to no limit in the lower breakup size or reference on the amount of breakup. The model does not include any adjustable parameter and depends strongly on the choice of integration limit which is common in the work of Prince and Blanch, (1990) and Tsouris and Tavlarides, (1994). The determination of lower and upper integral limits involves indirectly two unknowns (Liao and Lucas, 2009) and the model is highly dependent upon discretization of bubble size, and has neither limit for the lower breakup size nor any reference on the amount of breakup (Wang et al., 2003; Hagesaether et al., 1999). The model has received numerous disagreements (Sajjadi et al., 2013).
Chatzi and Lee, (1987); Chatzi et al., (1989)	$g(r) = k_{g_1} r^{-2/3} \varepsilon^{1/3} \left(\frac{2}{\sqrt{\pi}}\right) . \Gamma\left(\frac{3}{2}, \frac{k_{g_2} \sigma}{\rho_d \varepsilon^{2/3} r^{5/3}}\right)$	Developed from turbulent fluctuations theory. The difference between the other models is the probability density function of the turbulent kinetic energy is expressed by Maxwell's law. The

		daughter droplet size distribution is estimated from normal function model. However, the model received critics from Luo and Svendsen, (1996) since the Maxwell's law is appropriate for free gas molecular motion, thus, may not suitable for imaginary eddies. The model does not account the damping effect, $(1+\phi)$ as suggested by Coulaloglou and Tavlarides, (1977) and not suitable for gas-liquid system (Sajjadi et al., 2013)
Martínez-Bazán et al., (1999)	$g(r) = k_{g_1} \frac{\sqrt{k_{g_2}(\varepsilon r)^{2/3} - 6\frac{\sigma}{\rho_c r}}}{r}$	The model is based on purely kinematic ideas for fully developed turbulent flows. The model assumed that surface of a droplet must be deformed for a droplet to break. In this premise, sufficient energy must be available by the turbulent stresses in the surrounding continuous fluid. This model is similar to other models wherein, the droplet will break if the turbulent kinetic energy in continuous phase is greater than a critical value. The differences between other models are that this model neglect the probability theory for the distribution density of kinetic energy or velocity fluctuations as well as discard the damping effect at high dispersed fraction $(1+\phi)$.

Lehr et al., (2002)	$g(r) = \frac{2^{5/3}}{2} \frac{r^{5/3} \varepsilon^{19/15} \rho_c^{7/5}}{\sigma^{7/5}} exp\left(-\frac{\sqrt{2}\sigma^{9/5}}{8r^3 \rho_c^{9/5} \varepsilon^{6/5}}\right)$	The model developed based on force balance between the inertial force of the eddy and the interfacial force of the daughter drops. The model is the improved version from Lehr and Mewes, (1999). This model proposed the breakup probability based on the concept that kinetic energy of the eddy must exceeds the critical energy. This has to be obtained from force balance equation. One unique feature of this model is that, the probability of the bubble to break into two daughter droplets and its complimentary part is computed by differentiating the total breakup probability of the parent droplet. The model discounted the angle under which the eddy hits the droplets (Liao and Lucas, 2010) and the damping effect at high volume fractions $(1 + \phi)$.
Vankova et al., (2007)	$g(r) = k_{g_1} \frac{\varepsilon^{1/3}}{r^{2/3}} \sqrt{\frac{\rho_c}{\rho_d}} exp\left[-k_{g_2} \frac{\sigma}{\rho_d r^{5/3} \varepsilon^{2/3}}\right]$	The model is expressed in terms of turbulent fluctuations that affects the internal motion of drop in liquid. The model assumed that the eddies with size comparable to the drop dimeter, d , are most efficient in causing drop breakage, because the smaller eddies have much lower energy and the larger eddies are

		believed to have drag the droplet instead of deforming it. The model also utilizes the relationship between the Reynolds number in the drops with the velocity of the liquid inside the drops to estimate the deformation time. The model depends on the ratio of the density between continuous and dispersed of less viscous fluids and discounts the damping factor of $(1+\phi)$ at high dispersed fraction. The main parameters controlling rate of breakage of this model are energy dissipation rate, ε and interfacial tension, σ.

2.3.2 Daughter size distribution (breakage probability), $\beta(r, r')$

In order to have a complete description of the breakage sub-process, it is necessary to consider the daughter size distribution in terms of the number of drops formed and their distribution. The model has to be developed separately from the breakage frequency. The main goal of this function is to determine the probability of a certain size of droplets formed as a result of bigger droplets being ruptured. The daughter size distribution is composed of a probability density function and the number of drops formed after the breakage process. Most of the modelling works describe breakage as a series of binary breakage processes (Raikar, 2010). There are limited numbers of experimental and modelling studies for daughter size distribution with multiple and/or unequal size daughter droplets or combination of equal and unequal size daughter droplets to account for breakage event (Abidin et al., 2015). In general, the average number of daughter droplets formed depends on the forces applied, diameter, and the interfacial tension of the parent droplet (Hsia and Tavlarides, 1980). Based on these requirements, the daughter size distribution can be classified into three categories namely, empirical, statistical, and phenomenological.

2.3.2.1 Empirical model

Empirical model is formulated based on observation and experiment. Hence, it is considered as case specific (i.e., for a specific application and system). Thus, the model is normally not considered or preferred for the droplet size distribution. According to Solsvik et al., (2013), the empirical model limits the range of applications and is incapable of extrapolating outside of the operational conditions for which the model parameters were determined. In this respect, generalized model is more applicable where the number and size of droplets formed from a breakage event can be decently described regardless of the conditions (i.e., liquid-liquid or gas-liquid, stir tank or pipe flow). Hesketh et al., (1991) developed an empirical

model to determine the daughter size distribution in their study of bubble breakage in air-water pipeline flow.

2.3.2.2 Statistical model

In statistical approach, the size of the daughter droplets is usually described by the random variable and its probability distribution function proposed satisfies a simple expression. The common expressions used are as follows:

- Normal or Gaussian distribution
- Beta (β) distribution
- Uniform distribution

The normal density function was first introduced by Valentas et al., (1966) which later became widely used for investigations such as Coulaloglou and Tavlarides (1977), Chatzi et al., (1989), Lasheras (2002), and Raikar (2010). On the other hand, beta (β) distribution has been proposed by Hsia and Tavlarides in 1980 by modifying their earlier work. One of the advantages of beta (β) distribution is preventing zero probability for the evolution of equal-sized droplets as compared to other models (Azizi and Taweel, 2011). Nevertheless, Narsimhan et al., (1979) and Randolph, (1969) suggested that a random (uniform) distribution for binary breakage could be used to describe the droplets formed from the breakage event in agitated liquid-liquid dispersions. There has been disagreement reported from this assumption by Sajjadi et al., (2013) and Liao and Lucas, (2009) because nature does not split liquid volumes at random (Villermaux, 2007).

2.3.2.3 Phenomenological model

In the phenomenological model, the underlying concept is to relate empirical observations of important phenomena that corresponds to fundamental theory but is not directly derived from

the theory. In this respect, the underlying theory of such phenomena is not fully understood and may not yet have been discovered (Liao and Lucas, 2009) or the mathematics to describe such phenomena are too complex (Solsvik et al., 2013). From the shape of the daughter size distribution, the proposed phenomenological models are comprised of functions that are generally classified as U-shaped, Bell-shaped, and M-shaped. As reported by Abidin et al., (2015), the most widely used phenomenological model for the daughter size distribution is from the bimodal U-shaped function developed by Tsouris and Tavlarides, (1994). This is a model with highest probability density when one of the daughters has a minimum diameter (parent droplet unlikely to break) and lower probability density for two daughter droplets of same size. The model was developed based on the energy requirements for the daughter drops formation. In comparison to beta (β) distribution function, this model by Tsouris and Tavlarides, (1994) yielded minimum probability at equal size breakage while, beta (β) function produced maximum probability at equal size breakage which is the opposite of this model. However, the advantage of beta distribution model is that it predicts zero probability for daughter droplets with size equal to parent droplet and for droplets infinitely small (Abidin et al., 2015). In addition, the beta (β) distribution function is also capable to account for the total volume of droplets within the lower and upper limits of droplet size (Abidin et al., 2015). Luo and Svendsen, (1996) also proposed the U-shaped model for the daughter size distribution for drop breakage. The model has similar criteria with Tsouris and Tavlarides, (1994) where the probability is minimum at equal size breakage at maximum the volume fraction approaches zero or unity. Furthermore, the model has a non-zero minimum and mainly relies on the size of the parent droplet (Liao and Lucas, 2009). All the models discussed above for daughter size distribution are presented in the diagram as shown in Fig. 2.5 below.

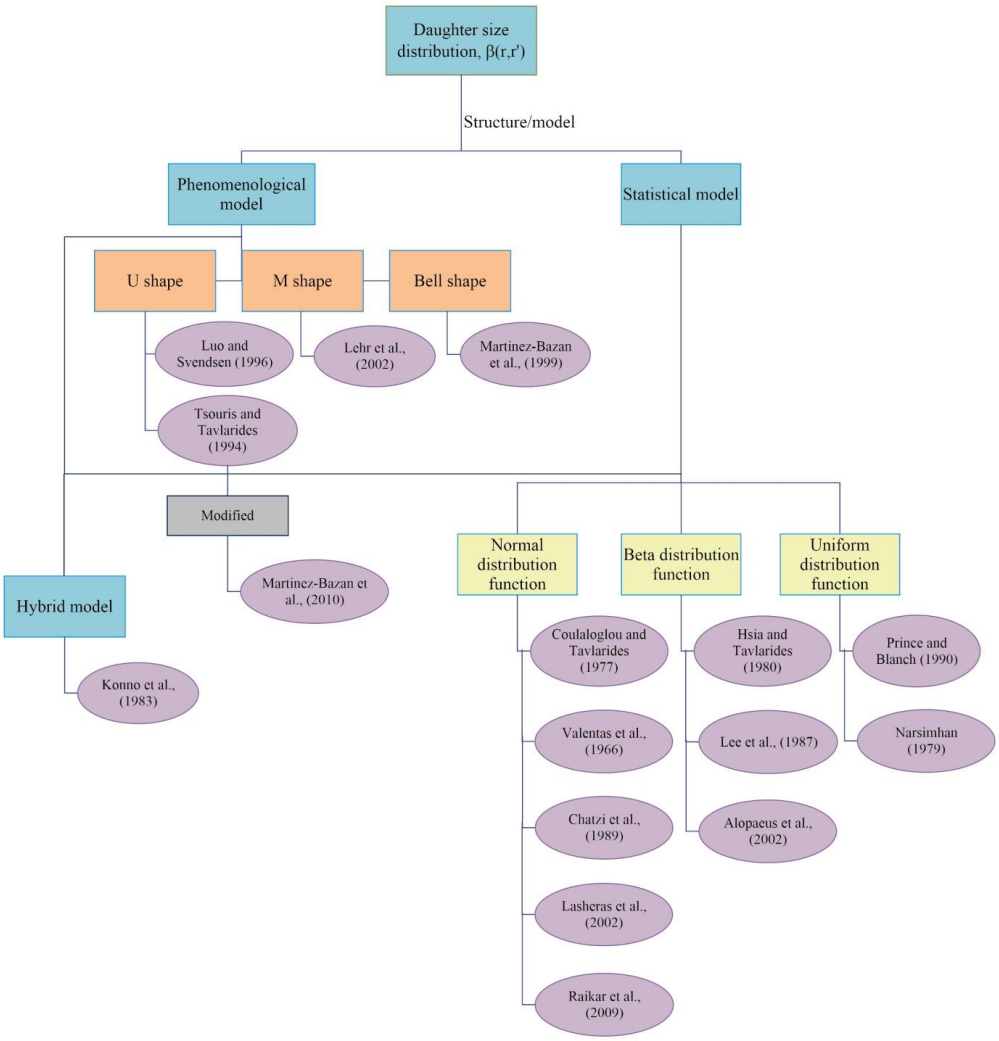

Figure 2.5 Type of models proposed for daughter size distribution, β

Additionally, Table 2.2 provides an insight and overview of several mathematical models developed and available in literature for breakage size distribution, $\beta(r, r')$ in terms of drop radius, r. Most of the models proposed in the literature are developed from the stirred tanks setup for liquid-liquid dispersions.

Table 2.2 Breakage size distribution function (daughter size distribution), β

Authors	**Breakage daughter size functions, $\boldsymbol{\beta(r, r')}$**	**Assessments of the model**
Narsimhan et al., (1979) and Randolph (1969)	$\beta(r, r') = \frac{1}{2r'^3} \times 3r^2$	The model assumes binary breakage with a uniform (random) distribution. This infers that parent bubbles break up into daughter droplets of any size with equal probability. They applied the model for droplets in agitated lean liquid-liquid dispersions and a mixed suspension crystallizer. $\beta(r, r') = 1/V_{r'}$. Lasheras et al., (2002) argued that, there are no physical grounds for selecting a uniform model since turbulent fluctuations are not uniform over all scales. Thus, this suggested that statistical models apply only to system that having stochastic characteristics (Liao and Lucas, 2009).
Hsia and Tavlarides, (1980)	$\beta(r, r') = 45 \frac{r^2}{r'^3} \left(\frac{r^3}{r'^3}\right)^2 \left(1 - \frac{r^3}{r'^3}\right)^2$	This model is developed based on a beta probability density function by assuming binary breakup with a two-parameter model. The model prevents zero probability for the evolution of equi-sized drops and

		droplets infinitely small. The model can take a variety of droplet shapes. It is also able to fit wider range of data compared to a truncated normal distribution as well as accounting the total volume of droplets within the lower and upper limits of droplet size (Abidin et al., 2015). This model parameters depend on flow condition and should be measured from experimental data. This model is believed to be considered only limited parameters and dependence on experimental operations increases with number of parameters (Sajjadi et al., 2013).
Tsouris and Tavlarides, (1994)	$\beta(r, r_{min}) = \frac{4r_{min}^2 + (1-2r_{min})^{2/3} - 1 + 2^{1/3} - 4r^2 - (1-8r^3)^{2/3}}{\int_{r_{min}}^{r_{max}} \left[4r_{min}^2 + (1-2r_{min})^{\frac{1}{3}} - 1 + 2^{\frac{1}{3}} - 4r^2 - (1-8r^3)^{\frac{2}{3}}\right] dr}$	The model is developed based on phenomenological model with a bi-model U shaped distribution. This model accounts probability density at low and high-volume fraction. Tsouris and Tavlarides, (1994) introduced the minimum particle size, r_{min} and defined arbitrarily to prevent the singularity present in the model. The model is derived by assuming that there is a linear

		relation between energy requirements for the formation of daughter droplets and daughter size distribution function, and minimal energy is required for drop breakage (Sajjadi et al., 2013). This model also avoids equal breakage and predicts the minimum probability for daughter droplets with equal size breakage and highest probability for very large droplets. Independent of parent size and flow conditions, however the breakage kernel does not satisfy the symmetry condition and preserve the volume (Solsvik et al., 2013).
Martínez-Bazán et al., (2010)	$$\beta(r, r_{min}) = \frac{\left[\left(4r_{min}^2 + (1-8r_{min}^3)^{\frac{2}{3}} - 1\right) + 2^{\frac{1}{3}} - 4r^2 - (1-8r^3)^{\frac{2}{3}}\right] 4r^2}{\int_{r_{min}}^{r_{max}} \left[\left(4r_{min}^2 + (1-8r_{min}^3)^{\frac{2}{3}} - 1\right) + 2^{\frac{1}{3}} - 4r^2 - (1-8r^3)^{\frac{2}{3}}\right] 4r^2 dr}$$	The model is based from phenomenological condition that relates empirical observations of phenomenon to each other. Martínez-Bazán et al., (2010) derived the daughter size distributions as a function of bell-shape distribution from stress balance. Hence, from the model, formation of daughter droplets with equal size have the highest probability, while one large and one

		small daughter droplets have the lowest probability (Asiagbe, 2018). This model is an improved model from Tsouris and Tavlarides, (1994) for binary equal size distribution. The model satisfies both the symmetry condition and volume conservation. However, the model is found to be inconsistent with experimental data by Hesketh et al., (1991) as reported by Liao and Lucas, (2010).
Konno et al., (1983)	$\beta(r,r') = \frac{\Gamma(12)}{\Gamma(3)\Gamma(9)}\left(\frac{r'}{r}\right)^8\left(1-\frac{r'}{r}\right)^2$	It is a hybrid model between statistical and phenomenological models. By applying a standard range of viscosity and different eddies scale for the energy distribution, they assumed that the daughter droplets are to be formed due to interaction between parent droplets and turbulent eddies of the same size. After the breakup, the model predicts three droplets with similar sizes from breakage event instead of two droplets as common in many studies, and this assumption is not in agreement with numerous experimental

		investigations (i.e., Hesketh et al., 1991; Andersson and Andersson, 2006). The model also is not volume conserved, hence is not accurate modelling of liquid dispersions (Solsvik et al., 2013).
Coulaloglu and Tavlarides, (1977)	$\beta(r,r') = \frac{0.3}{r'^3}\exp\left[-4.5\ \frac{(16r^3 - 8r'^3)^2}{(2r')^6}\right]$	The model is developed based on statistical approach by assuming that the function is normally distributed similar to Chatzi et al., (1989) and Valentas et al., (1966). The model assumes binary breakage and provides maximum probability breakage for equal size daughter droplets. They also fixed the standard deviation, σ_V such that $>$ 99.6% of the particle formed were within the volume range $V_r \in [0, V_{r'}]$ when $c = 3$ (Liao and Lucas, 2009; Solsvik et al., 2013).
Lee et al., (1987)	$\beta(r,r') = \frac{\Gamma(a+b)}{\Gamma(a)\Gamma(b)}\left(\frac{r'}{r}\right)^{a-1}\left(1-\frac{r'}{r}\right)^{b-1}$	The model developed is based on beta distribution for binary breakage and almost similar to the distribution proposed by Konno et al., (1983). The authors emphasized that the model is best fitted for multi-breakage model (Solsvik et al., 2013). The parameters a and b

		are determined empirically with experimental data of bubble breakage obtained from an airlift column. According to Lee et al., (1987), for binary breakage the best value for a and b is 2.0. However, the model is found to apply for a multi-breakage model in which number of daughter particles did vary with the mother particle size (Solsvik et al., 2013).
Lehr et al., (2002)	$\beta(r,r') = \frac{1}{\sqrt{\pi\left(\frac{r'^3}{r^3}\right)}} \cdot \frac{\exp\left\{-\frac{9}{4}\left[\left(\frac{2^{2/5}\rho_c^{3/5}\varepsilon^{2/5}}{\sigma^{3/5}}\right)\right]\right\}}{\left\{1+erf\left[\frac{3}{2}\ln\left(\frac{2^{1/15}\rho_c^{3/5}\varepsilon^{2/5}}{\sigma^{3/5}}\right)\right]\right\}}$	This model is based on phenomenological model with M-shaped distribution. In this model, the daughter droplet distribution is dependent on the parent size as such, the probability of small and large daughter droplets increases significantly with the parent size. They assumed that only eddies that are bigger than the smallest daughter droplet are able to carry the daughter droplet away. The model distribution changes from mono-modal to bi-modal with the increase of the parent droplet size. They reported that by increasing the parent droplet diameter, the

		probability of producing equal daughter droplet size decreases and unequal breakage is preferred. Thus, it becomes M-shaped for bigger drops and finally U-shaped for very big mother droplets (Sajjadi et al., 2013). The model predicts the equal-size breakage is more likely at small droplets than big droplets. However, so far there is no experimental evidence or theoretical support presented (Liao and Lucas, 2010).
Hesketh et al., (1991)	$\beta(r,r') = \left[\frac{1}{\left(\frac{r}{r'}\right)^3 + B} + \frac{1}{1-\left(\frac{r}{r'}\right)^3 + B} - \frac{2}{B+\frac{1}{2}}\right] \times \frac{A}{2r'^3} r^2$ $\frac{1}{A} = 2\left[ln(1+C) - ln(D) - \frac{1-2\left(\frac{r_{min}}{r'}\right)^3}{B+0.5}\right]$ $C = B - \left(\frac{r_{min}}{r'}\right)^3, \qquad D = B + \left(\frac{r_{min}}{r'}\right)^3$	Hesketh et al., (1991) developed the model based on the experiment performed on bubble breakage in turbulent pipe flow. They compared several daughter size distribution functions which include, binary equal-volume breakage, random breakage, $1/X$-shaped breakage, and attrition. The attrition breakage is described as a breakage in which a very small bubble and a bubble of nearly the same size as the breaking bubble is formed. While, $1/X$-shaped (as depicted in this Table 2.2) is a breakage function

		similar to attrition but allows bubbles size of any size less than, r' to be formed. They found that, the random breakage overpredicted the daughter droplets and attrition breakage overpredicted the formation of small daughter droplets. The best fit model with the experimental data is $1/X$-shaped breakage. This model produces higher probability for unequal size droplets than equal size droplets. However, the model parameter values will vary with different flow conditions and with initial droplet size (Lasheras et al., 2002). Thus, this model has no physical justification and is considered as empirical model but can be used for comparison with the phenomenological model (Solsvik et al., 2013).
Valentas et al., (1966)	$\beta(r,\bar{r}) = \frac{1}{\sigma_d\sqrt{2\pi}} exp\left(-\frac{2(r-\bar{r})^2}{\sigma_d^2}\right)$	Based on normal (Gaussian) distribution. This model was first to be developed by Valentas et al., (1966) from truncated normal probability density function. The model assumes that the daughter

		droplet diameters from the breakup of the parent droplet are normally distributed about a mean value, $\bar{r} = r/\acute{\eta}(r)$. Where $\acute{\eta}$ is number of droplets formed per breakage and $\sigma_d = \bar{r}/c$ in the function denotes the standard deviation and c is the tolerance. They believed that it is reasonable to expect that the daughter size distribution be normal or approximately normal because the breakage kernel is a composite of a large number of independent random events in which individually contribute only slightly to the final distribution.

2.4 Review of coalescence model

Apart from breakage process, coalescence is also responsible for the evolution of droplets in liquid-liquid or gas-liquid flows. In general, coalescence is a process when two or more droplets are merging to form a droplet. In this respect, the process is typically associated with contact and collision between droplets. In turbulence, the coalescence process is considered complex (Chesters, 1991) due to the interactions of droplets with surrounding continuous liquid and alongside other droplets. The coalescence model is normally expressed as the product of collision frequency, ω_C and coalescence efficiency functions, ψ_E. There are several models proposed in literature to calculate the collision frequency, ω_C and coalescence efficiency functions, ψ_E. Among the earliest models studied on coalescence are the ones by von Smoluchowski, (1917) who investigated the aggregation of particles by Brownian motion and Valentas and Amundson, (1966) that proposed mathematical descriptions for coalescence based on a film drainage process. The most widely applied modeling approach for coalescence is the film drainage model (Liao and Lucas, 2010). Film drainage is a process in which when the droplets collide, they will trap a small film of liquid between them. As they remain in contact, the liquid film separating the droplets slowly drains out to a critical thickness and eventually ruptures due to film instabilities which lead to formation of a single new droplet. In this section, a number of proposed models will be reviewed in the following sections:

2.4.1 Collison frequency function, $\boldsymbol{\omega_C(r', r'')}$

In turbulent flow, there are numerous mechanisms that could contribute to collision between droplets. These include the turbulent induced collision that forces the random motion of droplets during a chaotic turbulent flow, the eddy-induced collision in which the droplets that are captured in the same eddy may collide due to the shear rate in the eddy, the

velocity-induced collision where droplets from a region of relatively high velocity field may collide with a droplet at a region of relatively low velocity field, the buoyancy-induced collision such that the droplets of different sizes collide due to different sedimentation/creaming velocities and finally the wake effect that promote the collision of droplets due to the rise velocity of different size droplets. Fig. 2.6 shows the illustrations for each of the mechanism that contribute to coalescence process from Liao et al., (2015).

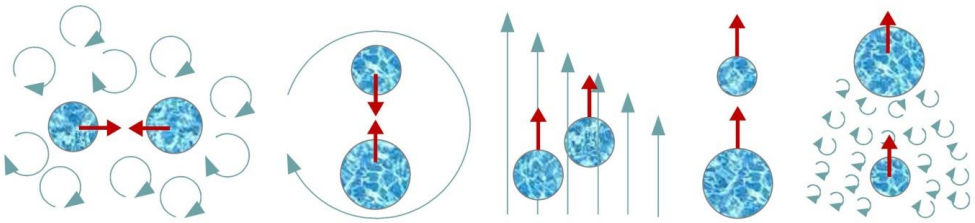

(a) (b) (c) (d) (e)

Figure 2.6 Types of collision mechanisms for droplets in turbulent flow: (a) Turbulent-induced collisions, (b) Droplets capture in an eddy, (c) Velocity gradient-induced collisions, (d) Buoyancy-induced collisions, and (e) Wake interactions-induced collision (Liao et al., 2015)

2.4.1.1 Turbulent-induced collisions

Turbulent-induced collision is the most important and dominant mechanism in describing the coalescence phenomenon (Abidin et al., 2015; Sajjadi et al., 2013). The collision between droplets occurs due to fluctuations of the turbulent velocity in the surrounding liquid and consequently induces a random motion to the liquid droplet. In this respect, the random movement of the liquid droplet is assumed to be analogous to the kinetic theory for collision between two gas molecules. All droplets in this mechanism are always

assumed to be within the inertial subrange of isotropic turbulence. The criteria for inertial subrange are as follows (Prince and Blanch, 1990; Luo, 1993):

$$k_e \ll k_b \ll k_d \ , \qquad r_e \gg r_b \gg r_d \tag{2.5}$$

In expression (2.5) above, k_e denotes the wave number of the large size (r_e) energy containing eddies, k_b represents the wave number related to the droplet size (r_b), and k_d and r_d are the wave number of eddies where viscous dissipation occurs. Apart from that, it also considers that very small eddies are having less energy to significantly affect the droplet motion and larger eddies in which bigger than the droplet size, transport the droplets without significantly affect the relative motion between droplets (Prince and Blanch, 1990). In terms of length scale, the largest length scale, r_e is considered the radius of the physical system (i.e., pipe, impeller) and the smallest length scale, r_d is the Kolmogorov microscale [i.e., $r_d = (\nu/\varepsilon)^{1/4}$]. In this mechanism, the collision frequency is generally expressed as the effective volume swept by the moving droplet per unit time (Liao and Lucas, 2009):

$$\omega_C(r', r'') = A_{r,r'}\left(u_{t,r}^2 + u_{t,r'}^2\right)^{1/2} \tag{2.6}$$

Where, A is the cross sectional of the colliding droplets and u_t is the turbulent velocity. The cross-sectional area is given by (Prince and Blanch, 1990):

$$A_{r,r'} = \pi(r' + r'')^2 \tag{2.7}$$

While, to determine the turbulent velocity u_t one must consider that the droplets are within the turbulent inertial subrange, hence it can be approximated by applying the classical turbulent theories (Luo, 1993):

$$u_{t,r}^2 = k_c 2^{2/3} (\varepsilon r)^{2/3} \tag{2.8}$$

Substitute both equations (2.7) and (2.8) into (2.6), the collision frequency becomes (Luo, 1993, Prince and Blanch, 1990, Coulaloglou and Tavlarides, 1977):

$$\omega_C(r', r'') = k_c \pi \varepsilon^{1/3} 4\sqrt[3]{2}(r' + r'')^2 \left(r'^{2/3} + r''^{2/3}\right)^{1/2} \tag{2.9}$$

This expression has been employed by many researchers some of which are Hsia and Tavlarides (1980), Lee et al., (1987), Kamp et al., (2001), Colin et al., (2004), and Wang et al., (2005). In a study of drop coalescence by Prince and Blanch (1990), they also postulated that the eddy motion due to turbulent fluctuations is primarily responsible for the random motion between droplets. The model proposed is similar to the one by Coulaloglou and Tavlarides, (1977), however the main differences are they discounted the effect of local turbulent intensities at volume fraction $(1 + \phi)$ and probability efficiency of complete mobile surfaces between droplets instead of immobile surfaces proposed by Coulaloglou and Tavlarides, (1977).

2.4.1.2 Velocity gradient-induced collisions

The mechanism of velocity gradient-induced collision is usually applied for gas-liquid system where the densities of bulk and droplet can be distinguished significantly. In this respect, the droplet movements are mainly dictated by their size and collisions are caused by

the relative sedimentation/creaming velocities between droplets. According to Pumir and Wilkinson, (2016) collision between droplets due to velocity gradient can be illustrated by two events: (i) from the gravitational effect in bubble column where larger bubble overtakes another bubble of small size, and (ii) shear flow effect where bubble (low-density phase) collides with bubble (high-density phase) as they are transported together. This is also agreed by Friedlander (1977) who explained that velocity gradient in laminar shear flow can contribute to collisions of droplets. They proposed a function to express the frequency of shear-induced collisions and can be applied in any case related to velocity gradient-induced collision (Liao and Lucas, 2009). Prince and Blanch, (1990) employed the function by Friedlander (1977) to describe the drop coalescence in the case of high gas rates in air-sparged bubble columns.

2.4.1.3 Droplet capture in an eddy

The third mechanism that contributes to collision is droplet capture in turbulent eddies. In this respect, the droplet size and eddy size can significantly influence the collision frequency. In turbulent flow, the collision frequency is predominantly viscous or inertial depending on the size of the particles. Chesters (1991) explained that in turbulent flow, when a droplet has a smaller size compared to energy dissipation eddies, the collision frequency is predominantly viscous and the force governing the collision is inertial if the particles are larger than Kolmogorov scale. Hence, in this case the drop velocity will be directly influenced by the eddies. In terms of density difference, Kocamustafaogullari and Ishii (1995) elucidated that in a system where the density of the drop is similar to the density of the continuous phase, the droplet velocities will be approximately close to the velocity of the continuous phase. Therefore, the collision frequency will be described by local shear of flow in turbulent eddies similar to laminar shear flow as expressed below (Liao and Lucas, 2010):

$$\omega_C(r', r'') = 0.618(r' + r'')^3\sqrt{\varepsilon/\nu} \quad (2.10)$$

Where, $\sqrt{\varepsilon/\nu}$ is a rate of strain characteristic of flow in the smallest eddies (Chesters, 1991). In comparison to laminar shear flow, the term $\sqrt{\varepsilon/\nu}$ is often used referred as the turbulent shear rate. Under this circumstance, the collision mechanism is known as eddy-capture (Liao and Lucas, 2010).

2.4.1.4 Buoyancy-induced collisions

The buoyancy-induced collisions are similar to the explanation by Pumir and Wilkinson (2016) where the collisions are resulted by the gravitational effect or the difference in rise velocity of the droplets having different sizes (Prince and Blanch, 1990). Friedlander (1977) has expressed the general function to determine collision frequency from the buoyancy-induced collision mechanism which is similar in Eqn. (2.6) except the turbulent velocity is replaced by the rise velocity due to gravitational body forces (Liao and Lucas, 2009). The rise velocity can be calculated from the Fan-Tcuchiya equation or Clift et al., (1978) as reported by Wang et al., (2005) and Prince and Blanch (1990).

2.4.1.5 Wake entrainment

The wake-induced collisions is produced by a liquid moving with uniform velocity under turbulent flow over the bubbles particularly during the free-rise of gas bubbles in vertical column. The wake entrainment collision is only important for gas-liquid systems with large fluid particles (Parente and De Wilde, 2018). During the event of free-rise of gas bubbles, the smaller fluid particles close to the wake can be accelerated, carried up and brought to collide with the leading fluid particles, thus generating the wake (Sun et al., 2004). According to Komosawa et al., (1980) the wake plays a significant role in promoting the

collisions between bubbles. Fu and Ishii, (2002) considered that coalescence due to wake entrainment as one of the five major bubble interactions. Karn et al., (2016) found that when bubbles are entrained into the wake region of a leading bubble, the smaller bubbles undergo acceleration in comparison to the larger bubbles and may collide with the preceding bubbles at higher speed than the velocity of the liquid. The same phenomenon was also encountered and explained before by Bilicky and Kestin (1987) in their study on transition criteria for air-water system in vertical upward flow. By taking into account the frequency between a trailing bubble in the wake and its leading bubble, Kalkach-Navarro et al., (1994), suggested the following expression for collision frequency:

$$\omega_C(r', r'') = k_c(V' + V'')\left(V'^{1/3} + V''^{1/3}\right)^2 \tag{2.11}$$

Where, k_c has the unit of rate per unit area (1/s.m^2) and is to be determined experimentally.

The classifications of mechanisms for collision frequency are illustrated in flow chart as shown in Figure 2.7. In general, there are various mechanisms that could contribute to particles collision. Hence, it is difficult to decide which mechanism plays the most significant role in certain collision cases (Liao and Lucas, 2010). However, if the particles size is within the inertial subrange of turbulence, the most important mechanism for collision will be the turbulent fluctuations (Liao and Lucas, 2010). This is due to the fact that, particles are exposed to random motion of eddies from all directions and most likely will result in collision between the particles. Due to this reason, turbulent fluctuation has been the preferred mechanism for drop formation and breakup as many research works are found to be based on this mechanism (shown in Fig. 2.7). Additionally, Table 2.3 depicts several of the proposed collision frequency models available in literature. It is observed that, majority of the

suggested coalescence models neglect the damping effects/factor $(1 + \phi_d)$ on the local turbulent intensities at high dispersed fraction in a similar way to breakage model. The author believes that, the inclusion for the effect of high dispersed phase in local turbulent intensities is critical in both breakage and coalescence models because for dispersed fluid flowing at low viscosity, the size of the droplet increases with increasing dispersed phase fraction as a result of turbulence hindering (Maaß et al., 2012). From liquid-liquid dispersion study by Coulaloglou and Tavlarides (1977), it is found that, they are not successful in the first attempt to correlate the theoretical and experimental size distributions over the range of dispersed phase between $0.025 \leq \phi \leq 0.15$. However, the experimental data are correlated successfully when they accounted the damping effects $(1 + \phi_d)$ at high dispersed fraction in turbulent flow field.

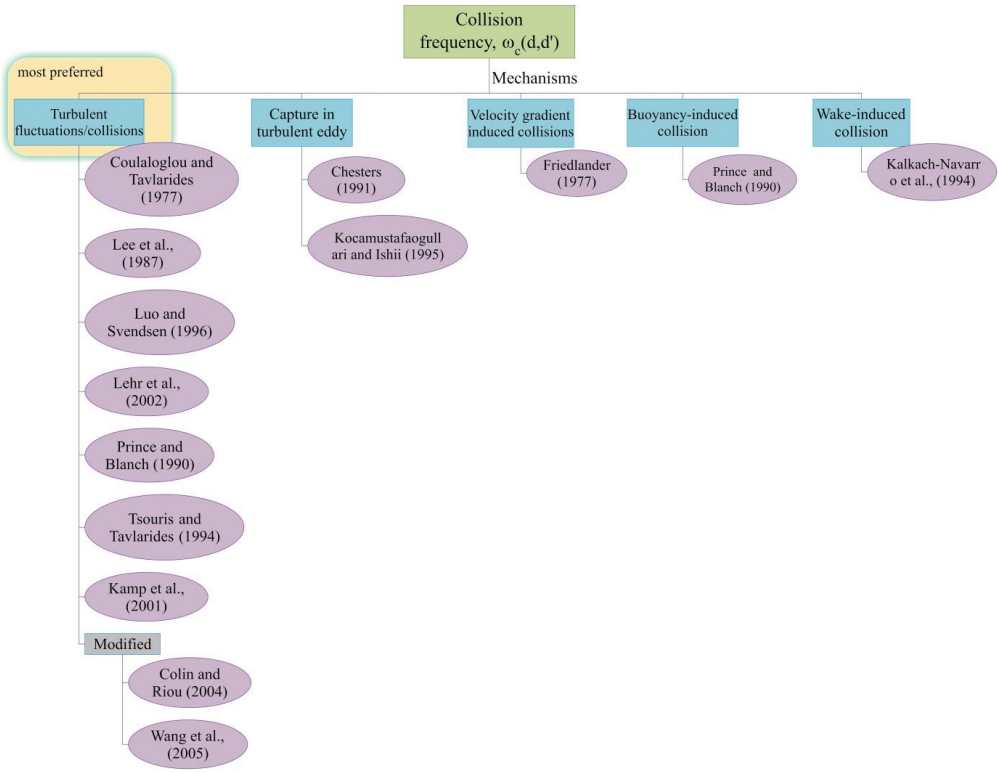

Figure 2.7 Type of mechanisms for collision frequency ω_C models

Table 2.3 Collision frequency functions, ω_C

Authors	**Collision frequency functions, $\omega_C(r', r'')$**	**Assessments of the model**
Coulaloglu and Tavlarides, (1977)	$\omega_C(r', r'') = k_\omega \frac{4\varepsilon^{1/3}}{1+\phi} \sqrt[3]{2}(r' + r'')^2 \left(r'^{2/3} + r''^{2/3}\right)^{1/2}$	This model is derived by assuming that the mechanism of collision between droplets in a locally isotropic flow field is analogous to collision between gas molecules as in kinetic theory of gases. However, the base of this concept is questionable because fluid particle collisions are either elastic nor rigid (Luo and Svendsen, 1996). The model is also further assumed that binary collision of equal-size droplets will occur under uniform energy distribution. All droplets are arbitrarily assumed to be in inertial subrange in isotropic turbulence. The model considers the turbulent random motion-induced collisions (turbulent fluctuations) and droplets with immobile interfaces**.** The model includes the damping effect on the local turbulent intensities at high holdup fractions $(1 + \phi)$. The model is able to

		correlate satisfactorily with the experimental data. However, this model has two limitations: 1) the assumption that all droplets have the same velocity as equal-sized eddies and 2) the assumption that all droplets have the inertial subrange arbitrarily (Sajjadi et al., 2013).
Prince and Blanch, (1990), Lee et al., (1987); Luo, (1993)	$\omega_C(r', r'') = k_\omega \pi\varepsilon^{1/3}\sqrt[3]{2}(r' + r'')^2\left(r'^{2/3} + r''^{2/3}\right)^{1/2}$	The model is developed based on turbulent induced-collision mechanism in which the primary cause of droplet collisions is the fluctuating turbulent velocity of the liquid phase. The model assumes that very small eddies do not contain enough energy to significantly affect the droplet motion, while eddies much larger than the droplet size transport groups of droplets without leading to significant relative motion. The model further assumes that the turbulence is isotropic and the droplet size within the inertial subrange, which is similar to Coulaloglu and Tavlarides, (1977). The model does not consider the correction factor, $(1 + \phi)$ for damping

		turbulence at high volume fractions. Note that, Prince and Blanch, (1990) found k_ω is in the range of 0.28 - 1.11.
Kocamustafaogullari and Ishii, (1995)	$\omega_C(r', r'') = k_\omega \, 8(r' + r'')^3 \sqrt{\varepsilon/\nu}$	The model is developed based on the mechanism of bubble capture in a turbulent eddy for gas-liquid dispersions. The model employs the shear flow to express the velocity averaged collision frequency due to the fact that velocity varies with the drop sizes and subsequently affecting the drop collision. They reported that drop size relative to the turbulent eddy will affect the collision frequency function. At which, small droplets will significantly be affected by the eddies if the size is smaller than turbulent eddies. However, if the drop density is equal to the density of the continuous phase, the drop velocity will be very close to the velocity of the continuous phase flow field, thus the collision frequency will be determined by the local turbulent flow characteristics.

Collin et al., (2004)	$\omega_C(r', r'') = \frac{1}{2}\left(\frac{8\pi}{3}\right)^{1/2} \frac{k_\omega}{\sqrt{1.61}\sqrt[3]{2}} 2^{7/3}(r' + r'')^{7/3}\varepsilon^{1/3}$ for $(r' < l_e; r'' < l_e)$ $\omega_C(r', r'') = \frac{1}{2}\left(\frac{8\pi}{3}\right)^{1/2} \frac{4k_\omega}{\sqrt{1.61}} 2^{1/3}(r' + r'')^2 r'^{1/3}\varepsilon^{1/3}$ for $(r' < l_e; r'' > l_e)$	The model is the improved version of Lee et al., (1987) and Luo, (1993). The model is proposed by taking into account the relationship between the droplet sizes and eddy sizes. The model considers droplets within and outside the inertial subrange. For droplets larger than turbulent eddies, it is assumed that the drop motion is mainly due to mean of shear flow. The droplets are assumed to remain spherical and are characterized by their radius, r. They assumed that if a droplet with radius, r' coalesce with a droplet of radius, r'' then a new droplet results with radius $(r'^3 + r''^3)^{1/3}$. Colin et al., (2004) reported that if the droplets are larger than the integral length scale, l_e turbulent eddies are not efficient to move the droplets and the relative droplet motion is mainly due to mean shear of the flow (Liao and Lucas, 2009). These two different scales suggested are to account the droplets acceleration and

		deceleration in turbulent collisions. They reported that generally, the droplet accelerates faster than the liquid which induces the turbulent fluctuation and decelerates as the droplets approach each other closely due to an increase in their coefficient of virtual mass (Kamp et al., 2001).
Chesters, (1991)	$\omega_C(r', r'') = k_\omega \, \varepsilon^{1/3} 2^{7/3} (r' + r'')^{7/3}$	This model assumes that when the drop density is very close to the density of the continuous phase flow field, the density difference between the drop and continuous phase will be very small. At this condition, the collision frequency is described by local shear flow in turbulent eddies. This is similar to when droplet size is smaller than the size of energy dissipating eddies found in turbulent flow (Sajjadi et al., 2013). Chesters (1991) applies this concept and developed collision frequency by assuming that the force governing the collision is predominantly viscous at internal microscopic flow field. The

		model applies for droplets that are within the inertial subrange turbulence. However, the model neglects the hydrodynamic interaction during the collision event between droplets. The model also discounts the effect local turbulent intensities at high volume fraction as suggested by Coulaloglou and Tavlarides, (1977). The model weakness is that it cannot predict coalescence kinetics accurately (Sajjadi et al., 2013).
Wang et al., (2005)	$\omega_C(r', r'') = k_\omega \varphi \Pi \varepsilon^{1/3} 4\sqrt[3]{2}(r' + r'')^2 \left(r'^{2/3} + r''^{2/3}\right)^{1/2}$ φ and Π are two modification factors; $\varphi = \frac{\phi_{max}}{\phi_{max} - \alpha}$ where ϕ_{max} is maximum volume fraction and α is phase holdup. $\Pi = exp\left[-\left(\frac{h_b}{l_{bt}}\right)^6\right]$ Where h_b is mean distance between bubble and l_{bt} is mean turbulent path length scale, m.	The model considers the turbulent random motion-induced collisions and is the improved model from Prince and Blanch, (1990). The model assumes that when the distance between droplets is larger than path length, thus, no collision should be counted. In this premise, decreasing factor Π is proposed. Both modification factors φ and Π play a similar role in which both are related to the volume fraction ϕ or the number density of droplets. The influence of volume fraction in the

		proposed collision frequency is obvious and important, however, the definition of φ and Π are still needed to be investigated thoroughly (Liao and Lucas, 2010). The model predicts small collision frequency for small droplets because the mean distance between small droplet is larger than big droplets if droplet number is equal (Liao and Lucas, 2009). The model also does not account the damping effect proposed by Coulaloglou and Tavlarides, (1977) for high turbulent intensities at high dispersed fraction.
Carrica et al., (1999)	$\omega_C(r', r'') = \left(\frac{3\varepsilon}{10\pi v}\right)^{1/2}\left[\left(\frac{4\pi r'^3}{3}\right)^{1/3} + \left(\frac{4\pi r''^3}{3}\right)^{1/3}\right]^3$ for $(r' < l_e; r'' < l_e)$ $\omega_C(r', r'') = 5.6\varepsilon^{1/3}\sqrt[3]{2}(d' + d'')^2 d'^{1/3}$ for $(r' < l_e; r'' > l_e)$	The model is derived from the turbulent-induced collisions and only binary collision event is considered. The model is proposed for gas-liquid system. They reported that during collision between droplets, coalescence may not happen however, momentum transfer between colliding droplets does occur. Hence, in regions where gas volume fraction is high the presence of surfactant can inhibit

		coalescence. They also assumed that the coalescence between droplets is due to relative motion or velocity between the droplets. The one feature about this model is that it is expressed in terms of large-scale turbulence and small scale turbulent as they believed that small eddies can also contribute to the collision rate. But so far, no experimental evidence to support the small eddies assumption by Carrica et al., (2004). However, the model is found to neglect the damping effect proposed by Coulaloglou and Tavlarides, (1977) for high turbulent intensities at high dispersed fraction.

2.4.2 Coalescence efficiency function, $\psi_E(r', r'')$

The model for coalescence efficiency or coalescence probability is introduced due to the fact that not all the droplets that collided coalesce and some fractions of the droplets are found to be separated after the collisions. In general, coalescence efficiency models are determined based on three major approaches namely energy model, critical velocity model, and film drainage model (Liao and Lucas, 2010; Solsvik and Jakobsen, 2014).

2.4.2.1 The energy model

The coalescence efficiency model based on energy approach was first introduced by Howarth in 1964 in his study on coalescence of droplets in a turbulent flow field. From the model proposed, it was found that, the efficiency of coalescence significantly increases with increasing energy of collision. Experimental evidence from Park and Blair, (1975) proved that the coalescence is most likely to occur when the turbulence energy increased. To express this phenomenon, Sovova, (1981) introduced the coalescence efficiency model that incorporates with kinetic collision energy (E_k) and surface energy (E_σ) as written below:

$$\psi_E(d, d') = exp\left(-k_c \frac{E_\sigma}{E_k}\right) \tag{2.12}$$

From the expression in Eqn. (2.12) shows that the probability of coalescence (ψ_E) from drop collision increases if the kinetic collision energy is greater than the surface energy holding the droplet together (i.e., $E_k > E_\sigma$). Simon, (2004) proposed coalescence efficiency model based on similar principles as Sovova, (1981) but using momentum balance expression to determine the kinetic energy during collision. Nevertheless, the model discounted the effect from the drainage and rupture of intervening film between droplets.

2.4.2.2 The critical velocity model

On the other hand, the critical velocity model approach is developed based on the opposite principles to the energy model approach. In this respect, the coalescence of droplets is observed to favour gentle collisions instead of high velocity collisions as proposed in the energy model (Liao and Lucas, 2010). In this model, the result of coalescence efficiency mainly relies upon the approach velocity of the colliding droplets. Lehr et al., (2002) proposed a simple expression to describe the coalescence efficiency in terms of critical approach velocity in bubble columns as follows:

$$\psi_E(r, r') = min\left(\frac{u_{crit}}{u_{rel}}, 1\right) \tag{2.13}$$

In Eqn. (2.13) above, the u_{crit} denotes the critical velocity and u_{rel} is the relative velocity between the droplets. This model is considered empirical owing to the fact that u_{crit} has to be determined experimentally.

2.4.2.3 The film drainage model

The film drainage model is the most accepted and widely used theory to determine the coalescence efficiency and has become the reference for all subsequent models (Liao and Lucas, 2010; Sajjadi et al., 2013). The film drainage model is developed based on two characteristic time scales known as contact time, $t_{contact}$ between colliding droplets and drainage time, $t_{drainage}$ for the intervening film to reach the critical thickness and rupture. To achieve coalescence, the collided drops must remain in contact for sufficient time until the liquid film thins to its critical thickness. In short, the contact time must be longer than the drainage time $\left(t_{contact} > t_{drainage}\right)$ for coalescence to occur as shown in Fig. 2.8 (Kamp et

al., 2017). Hence, through a constant force from the turbulence, the film will rupture and drop coalescence will occur.

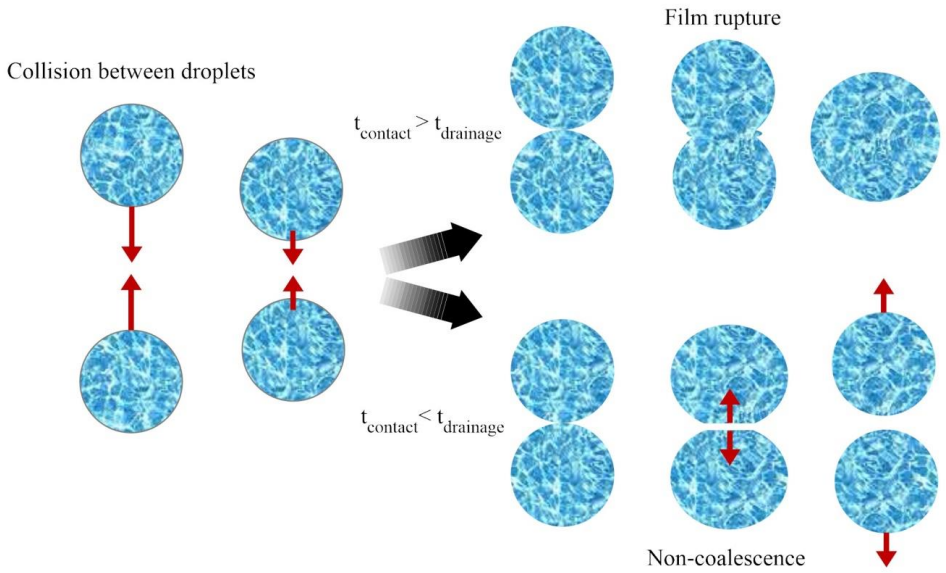

Figure 2.8 Coalescence efficiency events from the film drainage model

It is understood that the model is primarily dependent on the droplet size and the turbulent energy. Hence, the larger size droplets will have greater contact areas and high turbulent energy will increase the probability of an eddy to separate two droplets in contact (Prince et al., 1989). Coulaloglou and Tavlarides, (1977) introduced an expression that encompasses the two characteristic time scales as follows:

$$\psi_E(r, r') = exp\left(-\frac{t_{drainage}}{t_{contact}}\right) \tag{2.14}$$

In this expression, an increase in contact time over drainage time will increase the probability of coalescence and vice versa. The film drainage model has been investigated extensively

with a large number of models proposed in the literature are established from this concept as shown in the flow chart of Fig. 2.9. However most of the models proposed are subjected to specific criteria (i.e., drop rigidity and mobility interfaces) and the main difference between these models are in the expression for the drainage time, $t_{drainage}$ and contact time, $t_{contact}$.

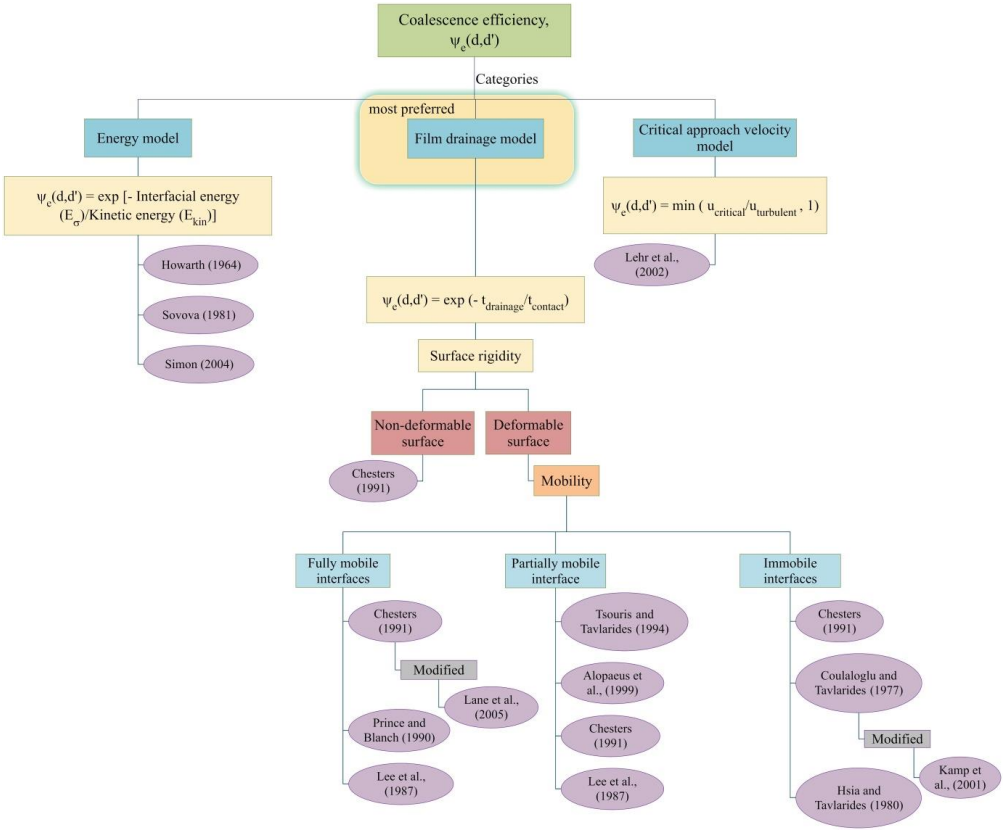

Figure 2.9 Type of coalescence efficiency models proposed in literature

The drainage time $t_{drainage}$ plays an important role in probability of successful coalescence. Hence it has been the subject to various investigations (Lee and Hodgson, 1968; Jeffreys and Davis, 1971; Lee et al., 1987; Coulaloglou and Tavlarides, 1977; Prince and

Blanch, 1990; Tsouris and Tavlarides, 1994; Luo, 1993; Chesters, 1991; Saboni et al., 1995; Simon, 2004; Lane et al., 2005). Most of the researchers agreed that in film drainage model the drainage time $t_{drainage}$ depends on the rigidity of the droplet surfaces as well as mobility of the contact interfaces (Lee and Hodgson, 1968; Chesters, 1991; Liao and Lucas, 2010; Sajjadi et al., 2013; Abidin et al., 2015). Analytical solution for $t_{drainage}$ exist is only for the case of non-deformable drops with immobile interfaces (Chesters, 1991). The contact time, $t_{contact}$ is also important for the calculation of the coalescence time in a turbulent system. There have been numerous studies and models proposed for the contact time in literature (Schwartzber and Treybal, 1968; Chesters, 1991; Luo, 1993; Coulaloglou and Tavlarides, 1977; Kamp et al., 2001; Tsouris and Tavlarides, 1994) and most of the models developed used the expression from Levich (1962) that are based on dimensional analysis.

2.4.2.3.1 Rigidity of droplet surfaces: non-deformable

The non-deformable droplets apply to the case where the droplets are far away from each other or the droplets are physically small in size for instance, the drop size diameter, $d < 1.0$ mm and the droplets have higher viscosity than the continuous phase (Simon, 2004, Liao; Lucas, 2010). In this respect, the droplets are assumed to be spherically rigid and non-deformable. Chesters (1991) proposed a model to describe the drainage time, $t_{drainage}$ under these circumstances for two equal-sized droplets with non-deformable surfaces via the Poiseuille relation. However, most researchers disagree with non-deformable surfaces theory due to the fact that the model only applies for very small droplets ($d < 1.0$ mm) wherein practically larger droplets also existed and should be considered during the collision (Simon, 2004).

2.4.2.3.2 Rigidity of droplet surfaces: deformable

Nearly all the film drainage models available in literature consider that the droplet surfaces are deformable. This is true considering the droplets in real conditions are present in the form of bigger and smaller sizes. Hence, deformable surfaces should be considered if one is investigating the coalescence efficiency based on the film drainage model. Kamp et al., (2017) explained that the collision between two droplets mostly occurs with deformable droplet surfaces as shown in Fig. 2.13 that subsequently resulted in coalescence. Liao and Lucas, (2010) argued that the complex film drainage with deformable surfaces depends on the mobility of the colliding interfaces. In this respect, the film drainage model can be divided into three regimes known as the deformable droplet with immobile, partially mobile, and fully mobile interfaces. These regimes are controlled by either inertial force dominate, or viscous force dominate in the draining film (Chesters, 1991). In the case where highly viscous dispersed phase is present in the liquid-liquid system, the drainage is mainly dominated by viscous force.

The rigidity of the droplet surfaces can be classified into two categories namely, deformable and non-deformable surfaces as shown in Fig. 2.10. While the mobility of the contact interfaces is divided into three types such as immobile interfaces, partially mobile interfaces, and fully mobile interfaces as depicted in Fig. 2.11 from Simon (2004) and Sajjadi et al., (2013) and Fig. 2.12 from Lee and Hodgson, (1968). Analytical solution for $t_{drainage}$ exist only for the case of non-deformable drops with immobile interfaces (Chesters, 1991).

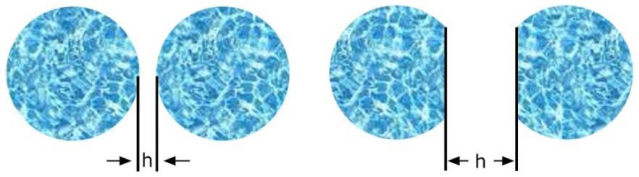

Figure 2.10 Rigidity of the droplet surfaces: (a) Non-deformable and (b) Deformable from Simon, (2004) and Chesters, (1991).

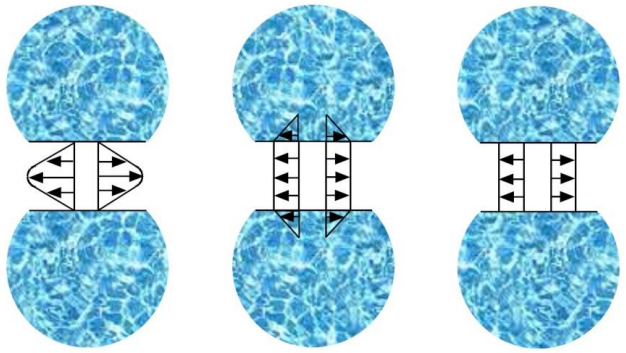

(a) (b) (c)

Figure 2.11 Mobility of the droplet interfaces: (a) Immobile interfaces, (b) Partially mobile interfaces, (c) Fully mobile interfaces, from Simon, (2004) and Sajjadi et al., (2013).

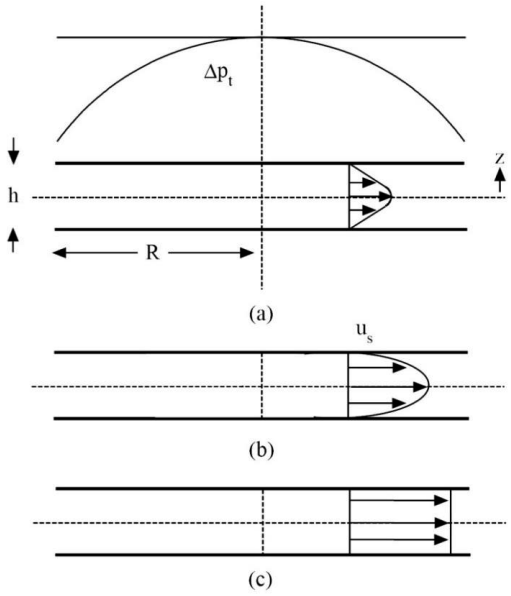

Figure 2.12 Mobility of the droplet interfaces at plane film (Lee and Hodgson, 1968): (a) Immobile interfaces, (b) Partially mobile interfaces, and (c) Fully mobile interfaces. The pressure distribution is shown at the top (a).

On the other hand, if the continuous phase has a low viscosity (i.e., inviscid), the drainage is dominated by the inertial force where the film deformed due to acceleration and continuous movements at the interfaces. Apart from that, in the deformable surfaces of the droplets, Derjaguin and Kussakov (1939) found that there is a dimple on the surfaces which indicates the presence of pressure gradient across the surfaces of the deformable droplets as shown Fig. 2.11. In this respect, the film layer is not flat and needs to be converted to a curved shape in order to accommodate the pressure gradient. However, due to simplicity, most of the drainage models proposed in literature discounted the dimple but instead considered a parallel (flat) model such that the thickness layer of liquid film is smaller than the radius of the droplets (Kamp et al., 2017). From this assumption, several models have been proposed while taking into account the mobility of the droplet interfaces.

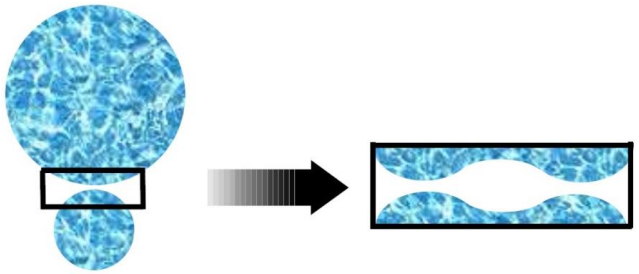

Figure 2.13 Deformable surfaces of droplets (Kamp et al., 2017)

2.4.2.3.2.1 Interface mobility: deformable with immobile interfaces

Droplets with immobile interfaces are generally applied to systems with a very viscous dispersed phase or systems with very specific surfactant soluble concentration in the continuous phase (Saboni et al., 1995; Liao and Lucas, 2010). In this respect, the deformable droplet with immobile interfaces (i.e., contact surfaces) is influenced by the viscous thinning or thinning rate of the film. The contact surfaces can be another droplet, a wall or the interface of the continuous fluid (Æther, 2002). According to Lee and Hodgson (1968), the immobile interfaces mean that there is a sufficiently large surface shear stress existing to oppose the viscous shear stress of the droplet or in other words, the droplet can support an infinite high shear stress (Æther, 2002). This occurs due to the presence of surfactant or impurities to immobilize the surface (Æther, 2002; Lee and Hodgson, 1968). The film at this condition will drain very slowly in comparison to the fully mobile case (Æther, 2002). The underlying theory for this model assumes that continuous flow in the liquid film is laminar and the inertial effects are negligible (Tsouris and Tavlarides, 1994). No slip at the surface and velocity profile as depicted in Fig. 2.11(a) indicates that the film is having maximum velocity at the centre and no velocity at the contact surfaces. Furthermore, the forces at the interfaces are assumed normal, hence, the Van der Waals, tangential, and double layer stresses are all negligible. The interaction between the film drainage and the movement

within the particles are separated. Colaloglou and Tavlarides, (1977) presented thorough synthesis of how coalescence occurs in liquid-liquid dispersion when the intervening liquid film drains to a critical thickness with deformable droplets at immobile interfaces.

2.4.2.3.2.2 Interface mobility: deformable with partially mobile interfaces

Droplets with partially mobile interfaces are generally applied to the system with intermediate viscosity, which is less than immobile case and greater than fully mobile case. It can also apply to a system where the impurities or the surfactants are swept away from the interfaces (Æther, 2002). In general, the drainage in liquid-liquid system is controlled by the motion of the film surface. Hence, if there is a presence of additional flow within the film due to prevailing pressure gradient being much smaller, the event is known as partially immobile interfaces (Chesters, 1991; Æther, 2002). Since film drainage model for drops with partially mobile interfaces is an intermediate case between immobile and fully mobile interfaces, partial mobility can be considered complicated case due to the fact that the drainage process is controlled by both inertia and viscous forces. Hydrodynamic force, F_y and compressing force, F_c are introduced to describe the interaction forces at the contact surfaces between the two droplets in terms of resisting (F_y) and attracting (F_c) forces. Both forces are assumed to occur during the film drainage and play an important role to develop the expression for the drainage time in terms of deformable drops with partially mobile interfaces and fully mobile interfaces. Davis et al., (1989) approximated the interaction forces, F_y and F_c to determine the drainage time, $t_{drainage}$ for drop with partially mobile interface and later employed by Tsouris and Tavlarides, (1994). On the other hand, Chesters (1991) also proposed the film drainage model for drops with partially mobile interfaces by assuming a quasi-steady creeping flow and Lee et al., (1987) employed the model from Sagert and Quinn (1976) to express the model for drops with partially mobile case.

2.4.2.3.2.3 Interface mobility: deformable with fully mobile interfaces

Deformable droplet with fully mobile interfaces is the case where the dispersed phase having a very low viscosity (i.e., inviscid). In this respect, the drainage is no longer controlled by the viscous stress as in partial mobility and immobile interfaces but instead by the resistance occurred in the film due to deformation and acceleration (Chesters, 1991). Therefore, the inertial forces are controlling the process of film drainage. As shown in Fig. 2.12 (c), the fully mobile has the uniform velocity profile which indicates that the film will drain fast at this condition compared to immobile case (Æther, 2002). In general, Chesters, (1991) and Chan et al., (2011) defined the deformable drops with fully mobile interfaces as a shear-stress free case or when the surface could not withstand the shear stress and move with the flow (Æther, 2002). In this respect, the system is either pure fluids (i.e., no impurities or surfactants) or the surfactant and impurities are swept away from the interface from the partial mobility. On the other hand, Davis et al., (1989) described the process to be influenced by the viscous force and approximated the resisting hydrodynamic force for fully mobile interfaces in terms of dispersed phase viscosity. Luo, (1993) proposed the film drainage model from the inertia-controlled limit for the case involving gas bubbles in turbulent flow. Chesters, (1991) proposed the drainage model by using the parallel-film model approach and taking into account the both terms which is viscous and inertial stresses. Lee et al., (1987) proposed the model for a system having a pure inviscid dispersed phase liquid ($\mu < 10$mPa.s) and Prince and Blanch, (1990) suggested the improved model from Oolman and Blanch, (1986) by discounting the Hamaker contribution due to the small influence on overall coalescence time. Several numbers of coalescence efficiency models proposed in the literature which are based on the three discussed mechanism are depicted in Table 2.4.

Table 2.4 Coalescence efficiency functions, ψ_E

Authors	**Coalescence efficiency functions, ψ_E**	**Assessment of the model**
Coulaloglu and Tavlarides, (1977)	$\psi_E(r', r'') = \exp\left[-k_\psi \frac{16\mu_c\rho_c\varepsilon}{\sigma^2(1+\phi)^3}\left(\frac{r'r''}{r'+r''}\right)^4\right]$	This coalescence efficiency model is developed based on two different characteristic time scales; drainage time scales and contact time scales. The coalescence is assumed to occur if the contact time between two droplets is longer than thinning time of the intervening film to reach critical thickness or referred to as drainage time (contact time > drainage time). The model also assumes that the droplet is deformable with immobile interfaces. Whilst the initial and critical film thickness are lumped into the constant parameter. The drainage time developed based on mobility of the colliding interface (i.e., immobile, partially mobile, or fully mobile). The coalescence time for mobile interfaces is shorter than immobile interface

		(Liu and Li, 1999). The interface mobility is associated with surface tension gradient and viscosity of the droplets, wherein increase in these parameters leads to immobility of the interfaces and decreases the coalescence efficiency. The model considers the damping correction factor $(1+\phi)$ to take into account the high dispersed volume fractions.
Luo, (1993)	$\psi_E(r', r'') = \exp\left[-k_\psi \frac{4u_{\text{rel}}\rho_c r'^2}{\sigma(1+\delta)^3}\sqrt{\left(\frac{0.75(1+\delta^2)(1+\delta^3)\sigma}{8\left(\rho_d/\rho_c + C_{VM}\right)\rho_c r'^3}\right)}\right]$ Where, $\delta = r'/r''$, $u_{\text{rel}} = 2.41^{1/2}\varepsilon^{1/3}\sqrt[3]{2}\left(r^{2/3} + r'^{2/3}\right)^{1/2}$	The model was developed based on turbulent random motion-induced collisions and film drainage model. Suitable for both partially and fully mobile interfaces. Luo, (1993) criticized the simplicity of Levich (1962) expression and suitability for unequal-sized liquid droplets as adopted by Chesters, (1991) in his coalescence efficiency derivation. In this premise, Luo, (1993) derived more reasonable and fundamental model for the interaction time based on simple parallel film model as

		depicted in Table 2.4. He added the mass coefficient, C_{VM} of the droplets in the expression similar to Luo and Svendsen (1996b) model. However, it is observed that C_{VM} is determined during the approach process (Kamp et al., 2001). According to the work by Jeelani and Hartland, (1991), the parameter C_{VM} is normally taken to be a constant between 0.5 and 0.8.
Luo and Svendsen, (1996b) and Wang et al., (2005)	$\psi_E(r', r'') = \exp\left[-\frac{\left(0.75(1+\delta^2)(1+\delta^3)\right)^{1/2}}{\left(\rho_d/\rho_c + C_{VM}\right)(1+\delta)^3} We_{d'd''}{}^{1/2}\right]$ Where, $\delta = r'/r''$ and C_{VM} is the virtual mass coefficient.	The model is based on energy conservation approach and a continuous work of Luo, (1993). The function assumes that the inertial collision is caused by turbulent fluctuations and they are derived based on isotropic turbulence. The droplet contact time was calculated based on energy conservation during droplet collision. The model was developed on basis of gas-liquid flow and accounts the effect of film drainage. They assumed that the time for the film area to go from zero to its

		maximum equals the time for the reverse process back to zero and this indicates that the interaction time not only depends on the fluid properties, but also on the radius ratio of the two approaching droplets or bubbles. The model shows a good ability to predict drop distribution.
Lane et al., (2005)	$\psi_E(r) = \exp\left(-0.71\sqrt{\frac{2^{5/3}\rho_c\varepsilon^{2/3}r^{5/3}}{\sigma}}\right)\times$ $\exp\left(-5.49\times10^6\times\frac{8r^3}{\varepsilon}\right)$	The model is the improved version from Chesters, (1991) and Prince and Blanch (1990). The model is developed on the basis that the rate of binary collisions between droplets moving with a random velocity equal to the turbulent fluctuating velocity of eddies of the same size within the inertial subrange. The model also accounts the finite time for droplet deformation and film drainage. According to Lane et al., (2005), the model by Chesters, (1991) neglected the minimum energy required for droplet deformation and the model by Prince and Blanch (1990) did

		not prove satisfactory when applied to the stirred tank simulations, since the model lead to substantial coalescence rates in the bulk of the tank, away from the impeller. Hence, they have improved the coalescence efficiency model and suggested in the model to account for the minimum level of turbulent energy that may affecting the coalescence efficiency as well as the negligible coalescence in the bulk of the tank that was overlooked by the model by Prince and Blanch (1990). They also counted the droplet volume as the amount of energy produced affected by the drop volume. The model was developed for equal-sized bubbles for gas-liquid system.
		The model was proposed from energy model (where the probability of immediate coalescence due to significant collision increases with increase in the energy of collision). The expression of this model

Sovova, (1981)	$\psi_E(r', r'') = \exp\left[-\frac{k_\psi \sigma (r'^3 + r''^3)(r'^2 + r''^2)}{2\rho_d \varepsilon^{2/3} r'^3 r''^3 2^{2/3} (d'^{2/3} + d''^{2/3})}\right]$	relates the kinetic collision energy to the interfacial energy in which they explained that adhesion forces are weaker than turbulent forces and thus unable to control the coalescence efficiency. This model predicts larger average time of coalescence for unequal-sized droplets and smaller average time for larger droplet sizes. It also predicts larger turbulent energy dissipation rates, and smaller surface potentials (Sajjadi et al., 2013). However, the model is found to overpredict the experimental results by Narsimhan, (2004) due to simplification of the reflecting boundary condition. In addition, this model does not consider the drainage and rupture of intervening film between drops (Abidin et al., 2015).
		Simon (2004) derived similar expression with Sovova, (1981) except that he calculated the kinetic energy from the

Simon, (2004)	$\psi_E(r', r'') = \exp\left[-\frac{4k_\psi\sigma(r'^2 + r''^2)}{\rho_d\varepsilon^{2/3}2^{11/3}(r'^{11/3} + r''^{11/3})}\right]$	momentum balance during the collision. The model was developed based on the premise of energy model approach which is similar to the work of Sovova (1981) and Chatzi et al., (1989). The model assumed that the interfacial energy of drops is proportional to drop surface area and interfacial tension. The kinetic collision energy is proportional to the relative velocity of two colliding drops and their average volume (Sovova, 1981). However, the kinetic collision energy can also be determined from the momentum balance during the collision of droplets as suggested by Simon, (2004) in his coalescence efficiency model. This model is not applicable for low turbulence and big droplets where the timescales of collision and coalescence are not analogous (Sajjadi et al., 2013).

Chesters, (1991)	$\psi_E(r', r'') = \exp\left[-k_\psi \frac{2^{5/6}\rho_c^{1/2}\varepsilon^{1/3}r_{eq}^{5/6}}{\sigma^{1/2}}\right]$ $where\ r_{eq} = \left(\frac{1}{r'} + \frac{1}{r''}\right)^{-1}$	The model was developed based on film drainage concept for deformable droplet with fully mobile interfaces. The model is derived based on similar concept of film drainage event as Coulaloglou and Tavlarides (1977) except on the mobility of the droplet interfaces. The model is developed for a liquid-liquid system with less viscous fluids (i.e., inviscid liquid). The drainage model is derived from the inertial terms in which the model assumed that the viscosity is sufficiently small, hence drainage is no longer controlled by the viscosity but by the resistance offered by the film to deformation and acceleration. This model suggested that the drainage time for the inertia thinning is proportional to the approach velocity. This indicates that if drainage time is small, the coalescence efficiency is high, thus the approach velocity is low (Liao and Lucas, 2010).

2.5 Energy dissipation rate

The turbulence kinetic energy dissipation rate, ε is an important property in turbulent flow at high Reynolds number as it controls the drop breakup, heat transfer and mass transfer (Wang et al, 2020). The rate of the dissipation is associated with the turbulent eddies in the fluid flow or in brief, the strength of turbulence. Ideally, the dissipation rate, ε indicates the rate at which the turbulence energy is absorbed, redistributed and transferred in the fluctuating flow by breaking the eddies into smaller scales in cascade process driven by vortex. In general, there are three different regions or energy flow of the turbulent energy cascade. The length scale of the largest eddy is referred to the region of energy-containing range. Instead, the smallest scale at which the eddies are dissipated by the viscous force and converted into heat is denoted as to the region of dissipation range (viscous effect is dominant). If the viscous effects are negligible, the eddies are suggested to be in inertial subrange. There are various energy dissipation rates have been proposed in the literature based on different turbulent conditions as depicted in Table 2.5.(Azizi and Taweel, 2011; Raikar et al., 2009; Galinat et al., 2005; Jakobsen, 2014; Hesketh et al., 1991).

Table 2.5 Turbulent dissipation rate, ε from literature

Author	**Energy dissipation rate, ε**	**Descriptions**
Galinat et al. (2005)	$\varepsilon = \frac{1}{\rho_c}\frac{\Delta P_{max} U}{2D}\left(\frac{1}{\beta^2} - 1\right)$ Where, $\beta = \frac{D_o}{D}$	The model is developed based on the relation between dissipation rate and maximum pressure drop across the orifice ΔP_{max} (pipe flow with restriction) as well as the orifice-pipe ratio, β.
Azizi and Taweel (2011)	$\varepsilon = \frac{U\Delta P}{\rho_c L_M}$	The rate of energy

		dissipation proposed from the pressure drop, ΔP in the static mixer.
Hesketh et al. (1991)	$\varepsilon = \frac{2v_c^3 f}{D}$ Where f is from the Blasius relation friction factor.	The energy dissipation rate is calculated based on the widely used empirical relationship in turbulent pipe flow. The friction factor, f is used for pressure drop in the system.
Raikar et al. (2009)	$\varepsilon = \frac{cP^{3/2}}{V^{1/3}\rho_d^{-3/2}}$ Where P is the homogenization pressure and c is constant.	The estimate is modified from Coulaloglou and Tavlarides (1977) for emulsion in high pressure homogeneizer.
Flórez-orrego et al. (2012)	$\varepsilon = 0.0176\frac{U^3 R_e^{-3/8}}{D}$	The energy dissipation rate is proposed from $\kappa - \varepsilon$ model. The turbulence assumed to be generated from the bulk.

Jacobi, (2014) modified the estimate of the energy dissipation rate, ε, based on the relationship between Reynolds number equation and friction factor, f in the global specific energy dissipation rate as follows:

$$\varepsilon \approx \frac{2v_l^3 f}{D} \approx \frac{2Re^3 \nu^4 f}{D^4} \approx 0.16 Re^{2.75}\left(\frac{\nu^3}{D^4}\right) \tag{2.15}$$

Where f in equation 2.15 is fanning friction factor. The relation for the turbulent dissipation energy is based on the wall friction as the primary source of turbulence production and is the extended version from Hesketh et al. (1991). The turbulent dissipation energy can also be

derived from the $\kappa - \varepsilon$ model as suggested by Flórez-orrego et al. (2012). However, this estimate is only valid in the bulk as there are hardly any production of turbulence in the bulk, thus the $\kappa - \varepsilon$ model length scale gives very minimum turbulence. Nevertheless, estimation of turbulent dissipation rate in turbulent multiphase flows is still limited (Wang et al., 2020). In the following section, an overview of the available and popular approaches for PBE solution are elucidated.

2.6 Solution to population balance equation (PBE)

This section offers an insight into several challenges as well as approaches employed by other researchers in the literature as an effort to solve the complex PBE. For a liquid-liquid flow in pipes, the droplet size distribution can affect significantly the rheological behaviour and the pressure gradient of the fluids (Arirachakaran et al., 1989). Hence, a good model that could accurately predict the drop size distribution in liquid-liquid emulsion is crucial, particularly in processes related to separation application (Schümann, 2016). Population balance equations (PBE) can be used to model and describe the complex case of dynamic evolution of drop size distribution in pipe flow. The PBE are also represent the transport equation for number density function of the droplets (Nguyen et al., 2016). In general, to solve the PBE, one must discretize the particle volume domain into a number of discrete elements. The resulting solutions will be in the form of stiff, nonlinear differential and/or algebraic equations that are subsequently integrated numerically (Alexopoulos et al., 2004). It is of interest to mention here that, there are many challenges involved in solving PBE such as numerical complications, large number of equations involved, modeling accuracy, computational efficiency, growth rate of the droplet due to breakage and coalescence, inconsistency of droplet distribution in terms of size and time, as well as the mechanism attributed to the drop size evolution (Rehman and Qamar, 2014; Pinar et al.,

2015; Korovessi and Linninger, 2005; Gunawan et al., 2004). According to Mesbah et al., (2009), the numerical solutions of PBE can be complicated due to the occurrence of sharp discontinuities and steep moving fronts that result from convective nature of partial differential equations as well as initial and boundary conditions incompatibility.

In recent years, there have been numerous methods proposed in literature to solve the PBE (Kumar et al., 2008; Omar and Rohani, 2017). These include finite volume methods, finite element methods, finite difference method, method of characteristics, moments method, least-squares method, and Monte-Carlo method (see details in the review article by Vikas et al., 2013; Kumar et al., 2008; Mesbah et al., 2009; Omar and Rohani, 2017; Solsvik et al., 2013). The finite volume method was originally established for gas dynamics and presently it has been adopted to solve the PBE (Qamar and Wernecke, 2007). It includes the discretization of the spatial domain and uses piecewise functions to approximate the derivatives (Mesbah et al., 2009). The resulting ordinary differential equations (ODE) will be integrated over time (see details in Vikas et al., 2013; Gunawan et al., 2004; Qamar and Wernecke, 2007). The finite element method involves the conversion from partial differential equations (PDE) into algebraic equations for steady state and ODE for dynamic state (Omar and Rohani, 2017). The final result in the form of stiff nonlinear differential equations is integrated over time (see details in Alexopoulos et al., 2004; Rigopoulos and Jones, 2003). However, this method may experience numerical complications due to the incompatibility between the initial condition and boundary condition that cause moving discontinuity in numerical solutions (Mesbah et al., 2009). In finite difference method, the differential equations in PBE are approximated by difference equations in which implicit, explicit, and Crank-Nicolson schemes are commonly used (Omar and Rohani, 2017). According to John and Suciu (2014), the finite difference method will lead to nonphysical oscillations and

accuracy may have to compromise with computational cost (see details in Bennet and Rohani, 2001; John and Suciu, 2014).

Kumar and Ramkrishna (1997) proposed method of characteristic to enhance the solution accuracy of the discretized PBE. In this method, the PDE are transformed into ODE by finding curves in the internal coordinate and time planes (i.e., L-t plane) resulting in significant improvement of solution accuracy (Gunawan et al., 2004; Mesbah et al., 2009). However, there are limitations involve of using this method in terms of long calculation times for complex case and practical system, time-step selections, and obligated scalar modelling (Lim et al., 2002) – see details in Lim et al., (2002) and Kumar and Ramkrishna (1997). Hulburt and Katz (1964) are among the first who introduced the method of moments and the main focus is to convert the PDE into ODE using a moment transformation. In this respect the PBE are converted into moment equations of the number density (Omar and Rohani, 2017). There are various other subsequent models developed based on this method for instance, quadrature method of moments, direct quadrature method of moments, sectional quadrature method of moments, and extended quadrature method of moments (see details in McGraw, 1997; Marchisio and Fox, 2005; Attarakih et al., 2009; Yuan et al., 2012; Akinola et al., 2013). However, for complex systems the moment closure conditions are violated, applicable to limited number of problems and no available information about the shape of the distribution (Dorao and Jakobsen, 2006a; Gunawan et al., 2004; Omar and Rohani, 2017). Another way of solving the PBE is by employing the least-squares method. The fundamental idea of least-squares method is to minimize the integral of the square of the residual over the computational domain (Dorao and Jakobsen, 2006a; 2006b). In this respect, the minimization is performed for the norm-equivalent functional (see details in Solsvik et al., 2013; Dorao and Jakobsen, 2006b; Zhu et al., 2008).

The least-square method is a well-established technique for solving various mathematical problems and details of this method are discussed by Jiang (1998) and Bochev and Gunzburger, (2009). However, in a system with high non-linearity and large scale, an error occurred in the properties of the distribution and the method becomes unstable (Omar and Rohani, 2017; Zhu et al., 2008). To address these issues, Zhu et al., (2008) introduced least-squares method with direct minimization method. Still, the method does not always produce a symmetric and positive-definite system (Omar and Rohani, 2017). Monte-Carlo method solves the PBE by generating a set of solutions from randomly generated numbers in the mathematical system (Omar and Rohani, 2017). To increase the accuracy of the system, a greater number of randomly generated input trials is needed, and many individual droplets must be tracked. In this regard, the method becomes computationally expensive (Nguyen et al., 2016; Kumar et al., 2008; Gunawan et al., 2004). Monte-Carlo method is suitable for a multi-dimensional and stochastic PBE particularly in a complex system (Kumar et al., 2008; Ramkrishna, 1985). Although a plethora of studies have been conducted on numerical solutions for PBE, robust solutions are still needed because more advanced control and optimization strategies can be developed (Omar and Rohani, 2017).

2.7 Chapter summary

In this chapter the introduction and the importance of PBE in modeling the liquid-liquid drops evolution is elucidated. In addition, the sub-processes for the population balance equations in terms of breakage and coalescence models are also reviewed and discussed. The underlying mechanisms for breakage frequency, daughter size distributions, coalescence frequency, and coalescence efficiency are also reviewed. Details of method employed are discussed in the following section.

CHAPTER 3

3 MODELING AND SIMULATION SETUP

3.1 Physical descriptions of the model

In turbulent dispersion of liquid-liquid systems, the fluid dynamics and the processes involving particularly breakage and coalescence are complex. The simplist model for the dynamic evolution of the drop density distribution of a liquid-liquid dispersion in turbulent pipe flow system should assume isotropic turbulence with a uniform (plug) velocity, U as shown in Fig. 3.1 across pipe diameter, D and length, L. This is a reasonable assumption considering that the fine-scale structure in most of non-isotropic turbulent flows is found to be locally close to isotropic (Hinze, 1959). Furthermore, isotropic turbulence assumption has often been used for liquid-liquid dispersion studies (Coulaloglou and Tavlarides, 1977; Tsouris and Tavlarides, 1994; Azizi and Tawell, 2011).

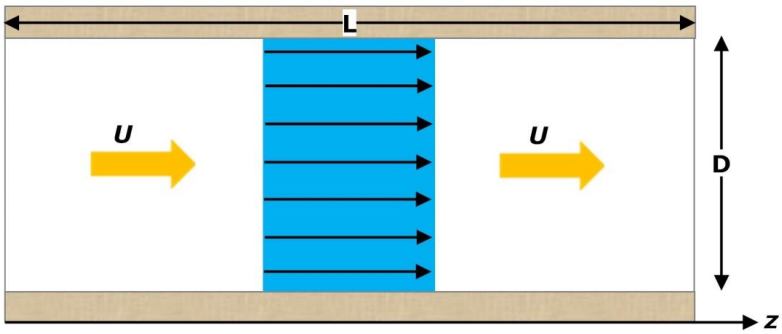

Figure 3.1 Sketch of turbulent flow field of a moving fluid in a pipe of length L, diameter D, and moving with an average velocity (plug flow), U

Due to the plug flow assumption any variance of the droplet sizes along the radial direction as well as angular direction of the pipe is neglected. The model considers that the birth and death processes of drops are due to breakage and coalescence. While, the distribution will be a function of time, axial position, z and drop radius, r (i.e., internal coordinate of r).

In addition, to minimize the complexity as well as to simplify the models, other assumptions and certain simplifications are necessary. In this regard, the model considers that, the droplets are spherical in shape and the droplet size is within the inertial subrange eddies $r_e \geq 2r \geq r_d$ (i.e., r_e is the integral length scale for large eddies and r_d is the Kolmogorov scale for small eddies). In this case, the viscous effect is negligible, and deformation of drops occurs primarily from turbulent fluctuations. Binary breakage is also assumed to take place in the system. With respect to these model assumptions, experimental evidence has also shown that binary breakage as depicted in Fig. 3.2 is most likely to occur in turbulent pipe flows (Hesketh et al., 1991).

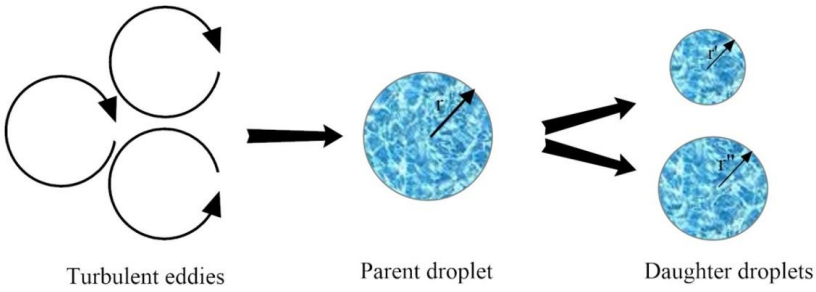

Figure 3.2 Binary breakage as a result of turbulent eddies

3.2 Initial conditions and population balance equation (PBE)

The number density distribution, $f_n(r,z)$ as a function of drop radius r (internal coordinate) and axial position z of the pipe (external coordinate) is used to represent the number distribution of droplets per unit volume (m^3) per unit drop size (m) in the system. From the definition of droplet number density distribution, $f_n(r,z)$ described above, the local

total number density function, $N_d(z)$ and the local volume fraction, $\phi(z)$, of the dispersed phase at a particular position of z coordinate can be written as follows, respectively:

$$N_d(z) = \int_0^\infty f_n\,(r', z)dr' \tag{3.1}$$

$$\phi(z) = \int_0^\infty \left(\frac{4\pi}{3}r'^3\right) f_n(r', z)dr' \tag{3.2}$$

In Eqn. (3.2) above, $\phi(z)$ remains constant across the length of the pipeline since no drop volume is gained or lost from coalescence or breakage and the volume is conserved. It is worth noting that, using the drop volume, v, the number density distribution f_n can be converted to the volume density distribution, f_v, as follows:

$$f_v(r, z) = v f_n(r, z) = \left(\frac{4\pi}{3}r^3\right) f_n(r, z) \tag{3.3}$$

Apart from that, by taking into account the process of birth and death by breakage and coalescence on the overall droplet growth processes, PBE for locally isotropic turbulent field can be written as follows:

$$\frac{\partial f_n}{\partial t} = R_{C_b}(r, t) - R_{C_d}(r, t) + R_{B_b}(r, t) - R_{B_d}(r, t) \tag{3.4}$$

By assuming isotropic turbulence with a uniform (plug) velocity, U in pipe flow. The expression in Eqn. (3.4) can be converted to rate of change of concentration of drops of radius r with axial position, z as follows:

$$U\frac{\partial f_n}{\partial z} = R_{C_b}(r,z) - R_{C_d}(r,z) + R_{B_b}(r,z) - R_{B_d}(r,z) \quad for\ 0 \le z \le L\ , 0 \le r \le \infty \quad (3.5)$$

In the Eqn. (3.5), R_{C_b} and R_{C_d} denote the birth and death rates of a droplet with radius r due to coalescence. While, R_{B_b} and R_{B_d} both represent the birth and death rates with radius r due to breakage, respectively.

The inlet ($z = 0$) number density function is, f_{n_0} and is given as:

$0 \le z \le L$, $0 \le r \le \infty$, and $f_n(r, z = 0) = f_{n_0}(r, z = 0)$

3.3 Coalescence birth and death functions

As volume is conserved in the coalescence process, the volumes of the parent droplets (i.e., volume of the colliding particles) must equal to the volume of droplet formed. In this respect, the radius, r'', of the second parent droplet is constrained by the radius, r, of the droplet formed and the radius, r', of the first parent droplet. The relationship between the merger of primary parent droplet which is having radius of r' with a secondary parent droplet of r'' and the formation of new droplet, r can be expressed as follows:

$$r'' = (r^3 - r'^3)^{1/3} \quad (3.6)$$

Therefore, based on these definitions and relationships, the coalescence birth rate as a function of drop radius, r and axial position, z is then given by:

$$R_{C_b}(r,z) = \int_0^{r/\sqrt[3]{2}} r_c(r', r'') f_n(r', z) f_n(r'', z) \frac{r^2}{r''^2} dr' \quad (3.7)$$

In the above equation (i.e., Eqn. 3.7), r_c represents the volume rate of coalescence and is the product between the collision frequency, $\omega_c(r', r'')$ and the coalescence efficiency, $\psi_e(r', r'')$ for drops having sizes of r' and r''. These two functions physically mean that two droplets will coalesce when they are in collision. Therefore, the volume rate of coalescence r_c can be written as follows:

$$r_c(r', r'') = \omega_c(r', r'')\psi_e(r', r'') \tag{3.8}$$

By taking into consideration the volume conservation in coalescence process, the parent droplets lost (death) from the birth of droplets by coalescence must be accounted for. Therefore, the death rate function from coalescence of parent droplets having radius r is given by:

$$R_{C_d}(r, z) = f_n(\mathrm{r,z}) \int_0^\infty r_c(r, r') f_n(r', z)\, dr' \tag{3.9}$$

Both Eqns. (3.7) and (3.9) are valid under conditions of, $0 \leq z \leq L$, $0 \leq r \leq \infty$.

3.4 Breakage birth and death functions

The death rate of a droplet having radius r due to breakage can be determined by the product of the breakage frequency, $g(r)$ and number density function, $f_n(r, z)$ as follows:

$$R_{B_d}(r, z) = g(r) f_n(r, z) \tag{3.10}$$

On the other hand, the breakage birth integral takes into account the birth of daughter droplets having radius, r that formed during the death of a parent droplet with radius, r'. The birth of droplets due to breakage can be determined by integrating over the interval of drop sizes, $r(r \leq r' \leq \infty)$. Therefore, for binary breakage, the breakage birth integral can be expressed as follows:

$$R_{B_b}(r,z) = \int_r^{\infty} 2\beta(r,r')g(r')f_n(r',z)\,dr' \tag{3.11}$$

Both Eqns. (3.10) and (3.11) are valid for the following domains: $0 \leq z \leq L$, $0 \leq r \leq \infty$.

In Eqn. (3.10), $\beta(r,r')$ is a daughter size distribution. The $\beta(r,r')$ term is introduced to characterize the probability of a drop with size r' to form a drop with size r during breakage. The model assumed binary breakage which indicates that at least two drops are formed during breakage process. In this respect, the number of drops formed is represented by the coefficient 2 in the breakage integral.

3.5 Collision frequency function, ω_C

Collison is essential for droplets to coalesce and merge in a multiphase flow system due to turbulent fluctuations. In this present study, turbulent-induced collision is selected due to its suitability as the collision frequency mechanism for the liquid-liquid system, while buoyancy and velocity gradient mechanisms are only applicable for gas-liquid system. For this study, the first collision frequency model by Coulaloglou and Tavlarides (1977) without the damping effects (1+ϕ) at high volume fraction is employed. The model is later compared with the addition of correction factor to observe the droplet growth (see discussion in Chapter 4). This coalescence frequency function will be utilized for the model comparison study

discussed in Chapter 4 of this thesis. The final expression for collision frequency function is given by:

$$\omega_c(r', r'') = 4\sqrt[3]{2}\, k_\omega \varepsilon^{1/3}(r' + r'')^2\left(r'^{2/3} + r''^{2/3}\right)^{1/2} \tag{3.12}$$

Where k_ω in Eqn. (3.12) above is a proportionality constant (or fitting parameter in the model) and ε is the energy dissipation rate per unit mass. The energy dissipation rate, ε in this work is employed from Jakobsen, (2014). The equation is recently developed by considering that wall shear from the pipe is the main source of turbulence production. Hence, the energy dissipation rate can be expressed as follows:

$$\varepsilon \approx 0.16 Re_m^{2.75}\left(\frac{{\mu_m}^3}{{\rho_m}^3 D^4}\right) \tag{3.13}$$

In the Eqn. (3.13) above, Re_m denotes the mixture Reynolds number and can be estimated as follows:

$$Re_m = \frac{\rho_m U D}{\mu_m} \tag{3.14}$$

In Eqn. (3.14), μ_m is the mixture viscosity, ρ_m represents the mixture density, U is the average flow velocity. The mixture estimations for viscosity and density are calculated based on suggestions by Schümann, (2016) for liquid-liquid mixture in pipe flow. For density mixture, the equation can be written as follows:

$$\rho_m = \phi_w \rho_w + \phi_o \rho_o \tag{3.15}$$

In Eqn. (3.15) above, the ϕ_w and ϕ_o indicate the phase fractions of oil and water, respectively. Where, ρ_w and ρ_o denote the density of water and oil, respectively. Schümann, (2016) proposed the widely used equation by Pal and Rhodes (1989) to estimate the mixture viscosity in liquid-liquid system as follows:

$$\mu_m = \mu_c \left[1 + \frac{0.8415\phi/\phi_{\mu_r=100}}{1 - 0.8415\phi/\phi_{\mu_r=100}}\right]^{2.5} \tag{3.16}$$

In Eqn. (3.16), μ_c indicates the viscosity of the continuous phase, ϕ is the dispersed phase fraction, and $\phi_{\mu_r=100}$ is a constant factor of the dispersed phase fraction. The value for $\phi_{\mu_r=100}$ is estimated when the mixture viscosity exceeds hundred times that of continuous phase. Schümann, (2016) used the value $\phi_{\mu_r=100} = 0.765$ proposed by Søntvedt and Valle (1994) for the liquid-liquid system as reported in Elseth (2001). From the author's best knowledge there are limited studies that focused on utilizing the mixture Reynolds number in estimating the rate of dissipation energy, ε. It is crucial to use the mixture Reynolds number Re_m in liquid-liquid dispersed flow to avoid overestimate of the energy dissipation rate, ε.

3.6 Coalescence efficiency function, ψ_E

The colliding droplets may not coalesce and repulse when they are in contact. Hence, the expression for coalescence efficiency is introduced to describe the effectiveness of coalescence from the result of collision between droplets. In this present work, film drainage model together with energy model are assessed and evaluated for better insight and understanding of the model. The critical approach velocity model is not selected in this study due to the fact that u_{crit} term in the model has to be determined experimentally (empirical

model) and the model is developed for bubble coalescence (i.e., gas phase) (Lehr et al., 2002), which is not applicable to the present study. For the main model, film drainage is selected, and energy model is employed as a model comparison (see chapter 4 in results and discussions as well as Part III of the manuscript prepared in the attachments – Appendix D). The efficiency function developed by Chesters (1991) is selected for this work. The model is based on film drainage between colliding dispersed phase entities of two deformable droplets of radius $r^{'}$ and $r^{''}$. The coalescence efficiency can be expressed as follows:

$$\psi_E(r', r'') = \exp\left[-k_\psi \frac{\rho_c^{1/2}\varepsilon^{1/3} r_{eq}^{5/6}}{2^{1/6}\sigma^{1/2}}\right] \qquad where, r_{eq} = \frac{1}{2}\left(\frac{r'r''}{r' + r''}\right) \tag{3.17}$$

Where k_ψ in the Eqn. (3.17) is a universal constant that takes in the value of initial film thickness and the film thickness at which film rupture occurs and carries no unit. Apart from efficiency model by Chesters (1991), the film drainage model by Coulaloglou and Tavlarides (1977) as well as energy model by Simon, (2004) are also assessed and evaluated in the model comparisons discussed in Chapter 4 (results and discussions) of this thesis. The comprehensive study on regression and model comparison can also be found in the Part III of the manuscript prepared – refer to Appendix D.

3.7 Breakage frequency functions, $g(r)$

Breakage frequency functions $g(r)$ are derived based on the interactions between the turbulent eddies and the droplets due to turbulent fluctuations. Vankova et al., (2007) modified the model by Coulaloglou and Tavlarides (1977) to consider the effect of densities from dispersed and continuous phases. In this present work, the model proposed by Vankova et al., (2007) is selected and the expression takes the following form:

$$g(r) = k_{g_1} \frac{\varepsilon^{1/3}}{2^{2/3} r^{2/3}} \sqrt{\frac{\rho_c}{\rho_d}} exp\left[-k_{g_2} \frac{\sigma}{\rho_d 2^{5/3} r^{5/3} \varepsilon^{2/3}}\right] \quad (3.18)$$

Eqn. (3.18) above involves the system properties such as dispersed phase volume fraction (ϕ), interfacial tension (σ), dispersed and continuous phase densities (ρ_d) and (ρ_c), energy dissipation rate (ε) and proportionality constants (k_{g_1} and k_{g_2}). In this study, the model by Vankova et al., (2007) and Coulaloglou and Tavlarides (1977) are selected for model comparison and are discussed in Chapter 4 of this thesis.

3.8 Breakage size distribution function (daughter size distribution), $\boldsymbol{\beta(r, r')}$

The expression for breakage size distribution is a relationship between the number of new (daughter) droplets as a function of r formed to the number of initial (parent) droplets as a function of r' that rupture. In this present study, the binary breakage event with equal sized droplets by Coulaloglou and Tavlarides (1977) is employed. The daughter size distribution is given as follows:

$$\beta(r, r') = \frac{2.4}{r'^3} \exp\left[-4.5 \frac{(2r^3 - r'^3)^2}{r'^6}\right] \times 3r^2 \quad (3.19)$$

Apart from the normal distribution model proposed by Coulaloglou and Tavlarides (1977), the more complex beta distribution by Hsia and Tavlarides, (1980) is also assessed in the model comparison discussed in the Chapter 4 of this thesis. Manuscript Part III (Appendix D) prepared for the model comparisons provide more comprehensive discussions.

3.9 The mean radii and standard deviations of number and volume density distributions

The mean drops radii of the dynamic evolution of drop number and volume density distributions, μ_N and μ_V can be formulated by normalizing the number and volume density distributions to the first statistical moments. Hence, the mean radii μ_N and μ_V can be expressed as follows, respectively:

$$\mu_N(z) = \frac{1}{N_d(z)} \int_0^\infty r' f_n(r', z)\, dr' \tag{3.20}$$

$$\mu_V(z) = \frac{1}{\phi(z)} \int_0^\infty r' \left(\frac{4\pi}{3} r'^3\right) f_n(r', z)\, dr' \tag{3.21}$$

The following are the expressions for standard deviation of the number and volume density distributions, σ_N and σ_V. The standard deviations are determined by normalizing the f_n and f_v to the second statistical moments about the mean. The standard deviations of σ_N and σ_V are given by:

$$\sigma_N(z) = \sqrt{\frac{1}{N_d(z)} \int_0^\infty \left(r' - \mu_N(z)\right)^2 f_n(r', z)\, dr'} \tag{3.22}$$

$$\sigma_V(z) = \sqrt{\frac{1}{\phi(z)} \int_0^\infty \left(r' - \mu_V(z)\right)^2 \left(\frac{4\pi}{3} r'^3\right) f_n(r', z)\, dr'} \tag{3.23}$$

3.10 Population balance equations for turbulent flow of oil and water in pipes

In this present work, the population balance equation (PBE) can be written as follows:

$$U\frac{\partial f_n(r,z)}{\partial z} = \int_0^{r/\sqrt[3]{2}} r_c(r',r'')f_n(r',z)f_n(r'',z)\frac{r^2}{r''^2}dr' \; - \; f_n(r,z)\int_0^{\infty} r_c(r,r')f_n(r',z)\,dr'$$

$$+ \int_r^{\infty} 2\beta(r,r')g(r')f_n(r',z)\,dr' \quad - \; g(r)f_n(r,z) \tag{3.24}$$

The population balance equations above are defined in the following domains:

$0 \le z \le L \;,\; 0 \le r \le \infty$

In Eq. (3.24) above, $f_n(r,z)$ denotes the number density function in terms of r, radius of the droplets (internal coordinate) and z, the axial position of the droplet in the pipe (external coordinate).

In this present work, the PBE in Eqn. (3.24) is formulated in terms of number density distribution, $f_n(r,z)$. From the fact that the magnitude of number density distribution $f_n(r,z)$ can alter significantly during drop growth process, thus, the PBE in Eqn. (3.24) is modified to account for volume density distribution, $f_v(r,z)$ in order to have a consistent magnitude over time. One of the advantages of this approach is that the convergence criterion in terms of relative tolerance and absolute tolerance are consistent with volume density distribution for the numerical calculations. To achieve this, the volume fraction, $\phi_v(z)$ at a particular position of z coordinate is required. By applying the Eqn. (3.3) into Eqn. (3.24), the modified population balance equation in terms of volume density distribution is given as follows:

$$U\frac{\partial f_v(r,z)}{\partial z} = v\int_0^{r/\sqrt[3]{2}} r_c(r',r'')\frac{f_v(r',z)}{v'}\frac{f_v(r'',z)}{v''}\frac{r^2}{r''^2}dr' - f_v(\mathrm{r,z})\int_0^{\infty} r_c(r,r')\frac{f_v(r',z)}{v'}dr'$$

$$+ v\int_r^{\infty} 2\beta(r,r')g(r')\frac{f_v(r',z)}{v'}dr' \; - \; g(r)f_v(r,z) \tag{3.25}$$

For $0 \le z \le L \;,\; 0 \le r \le \infty$

This new formulation (Eqn. 3.25) represents population balance equation in terms of volume density distribution for dynamic evolution of droplet size in oil-water (turbulent) pipe flow. This formulation describes the volume change per unit pipe length instead of number change per unit pipe length. Thus, one could easily identify the coalescence birth relative to death at larger droplet sizes. To simulate the model and facilitate the numerical solutions, the system equations should be scaled into dimensionless variables. In this respect, the model is able to characterize the system behaviour at dynamically similar system and different scales. The scaling and the dimensionless analysis of the model equations are described in detail in the Appendix A of this thesis. For comprehensive descriptions of the dimensionless techniques and analysis, please refer to Part I of the manuscript – Appendix B.

3.11 Algorithm and numerical protocols

Following the non-dimensional conversions, the model equations are then solved numerically starting from the initial distribution of the system. In this work, the algorithm is written to operate on either a user defined distribution or from experimental data. In either case, the values of the distribution might be arbitrary meaning it would not satisfy Eqn. (3.2). To achieve this, the following methods are used:

The variables in the distribution are defined as follows:

$$\vec{f}_{n0} \approx f_{n,exp,i} \qquad where\ i = 1,2, \dots \dots . N_{ini} \tag{3.26}$$

$$\vec{r}_e \approx r_{exp,i} \qquad where\ i = 1,2, \dots \dots . N_{ini} \tag{3.27}$$

$$\vec{\delta}_v \approx \frac{4}{3}\pi r_{exp,i}^3 \qquad where\ i = 1,2, \dots \dots . N_{ini} \tag{3.28}$$

In the above equations from (3.26) until (3.28), r_{exp} represents the experimental droplet radius, N_{ini} denotes the number of data (experimental data), and δ_v is the volume size of each droplet in the distribution. Depending on the type of initial distributions (i.e., number density distribution or volume density distributions), the integrations are approximated as follows:

The program reads in and integrates an arbitrary number density distribution:

$$I_n = \int_0^{r_e} \delta_v f_{n0} dr' = \sum_{i=2}^{N_{ini}} (\delta_{v,i} f_{n,exp,i} + \delta_{v,i-1} f_{n,exp,i-1})(r_{exp,i} - r_{exp,i-1})/2 \tag{3.29}$$

The program reads in and integrates an arbitrary volume density distribution:

$$I_v = \int_0^{r_e} f_{n0_e} dr' = \sum_{i=2}^{N_{ini}} (f_{n,exp,i} + f_{n,exp,i-1})(r_{exp,i} - r_{exp,i-1})/2 \tag{3.30}$$

Once the integration is determined, the number and volume density distributions can be scaled as follows:

(i) For number basis

$$f_n = \frac{\phi}{I_n} f_{n0,exp} \tag{3.31}$$

$$f_v = f_n \delta_v \tag{3.32}$$

(ii) For volume basis

$$f_v = \frac{\phi}{I_v} f_{n0,exp} \tag{3.33}$$

$$f_n = f_v / \delta_v \tag{3.34}$$

It is worth noting that, the experimental data from FBRM technique supplied in this present work are measured in terms of number density distribution, f_n. Hence, Eqns. (3.29), (3.31), and (3.32) are employed for the experimental data used.

On the other hand, the parameter R_{max} or maximum drop radius is introduced to the system. The value of R_{max} is set arbitrarily due to the fact that the exact value for R_{max} is unknown until the simulation is performed. In this respect, the value of R_{max} is set large enough such that the volume and number density distributions are not exceeding the R_{max} as they evolve. In addition, R_{max} is important to the non-dimensionalization of the system equations because it represents the characteristic length of the radial coordinate (internal coordinate) in the scaling formulation (refer to Appendix A of dimensional analysis). Apart from that, to facilitate interpolation of the experimental data and the simulation grid, an arbitrary number of additional points are added between maximum experimental radius, $R_{max,exp}$ and R_{max}. The additional points are added if the condition of $R_{max} > R_{max,exp}$ is met.

3.11.1 Numerical protocol in non-dimensionalization system

On top of that, to enhance the numerical solutions, spectral elements (n) are introduced to the system. This is achieved by splitting the drop radius coordinate into several domains, while the element boundaries are determined by $r_{n,min}$, $r_{n,mean}$, $r_{v,at\ volume\ 99\%}$, $r_{v,\log space}$ (from the logarithmic spacing), and r_{max} (equivalent to R_{max} in dimensional system) of the volume density distribution as shown in Fig. 3.3 with $\overline{f_v}$ indicates the dimensionless volume density distribution (refer to dimensionless analysis in Appendix A). In this respect, the element end points or the boundaries in terms of dimensionless radius (ξ^n) can be determined as follows:

$$\xi^1 = 0/R_{max} = 0 \tag{3.35}$$

$$\xi^2 = r_{n,min}/R_{max} \tag{3.36}$$

$$\xi^3 = r_{n,mean}/R_{max} \tag{3.37}$$

$$\xi^4 = r_{v,at\ volume\ 99\%}/R_{max} \tag{3.38}$$

$$\xi^5 = r_{v,\log space}/R_{max} \tag{3.39}$$

$$\xi^6 = r_{max}/R_{max} = 1 \tag{3.40}$$

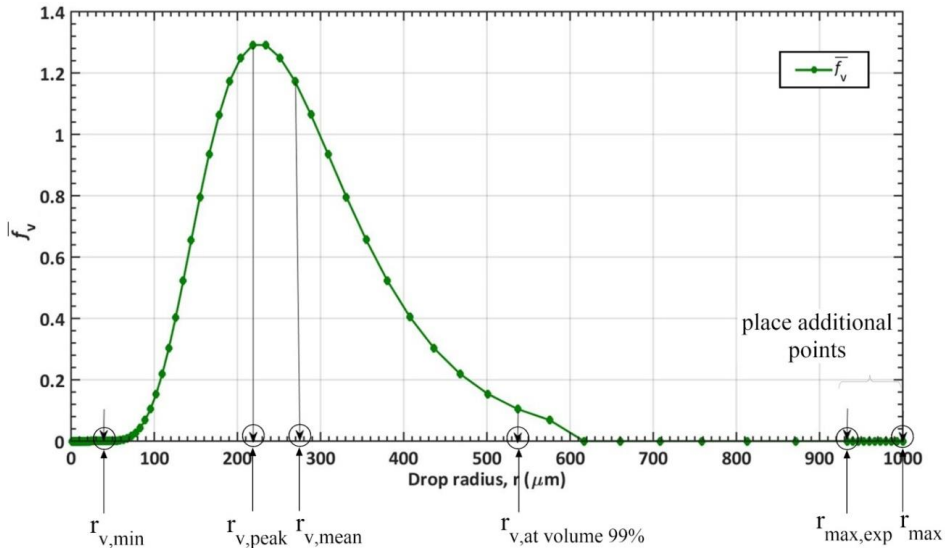

Figure 3.3 schematic diagram of the radial coordinate and the properties of the volume density distribution in terms of minimum radius, peak radius, mean radius, radius at 99% volume, maximum experimental radius, and maximum (simulation) radius.

The total number of spectral elements, N_t employed in the system is important in order to set the element end point, ξ^n for the system. For instance, if the total number of elements, $N_t \geq 5$, the element end point, ξ^n takes in the following value:

$$N_t \geq 5,\ \xi^n = \xi_0, \xi_{n,min}, \xi_{n,mean}, \xi_{v,99}, \xi_{v,\log space}, \xi_1$$

In the expression above, ξ_0 indicates the initial radius at zero coordinate, $\xi_{n,min}$ represents the smallest radius where the number density distribution is non zero, $\xi_{n,mean}$ denotes the mean value of the number density distribution, $\xi_{v,99}$ signifies the radius located where the volume density distribution integral (i.e., ϕ) is 99% of the total integral value, and at the last number of element (i.e., $N_t \geq 5$) the radius will be located at the logarithmically spaced points between $\xi_{v,99}$ and 1.0 (i.e., 10^0) which refers to $\xi_{v,\log space}$. Otherwise, (i.e., if $N_t < 5$), the element end point, ξ^n will take the following steps:

$N_t = 4,\ \xi^n = \xi_0, \xi_{n,min}\ , \xi_{n,mean}\ , \xi_{v,99}, \xi_1$

$N_t = 3,\ \xi^n = \xi_0, \xi_{n,mean}\ , \xi_{v,99}, \xi_1$

$N_t = 2,\ \xi^n = \xi_0, \xi_{v,99}, \xi_1$

$N_t = 1,\ \xi^n = \xi_0, \xi_1$

Gauss-Lobatto Quadrature with Jacobi Polynomials is constructed for each of the element (n) along with user defined value for the number of internal collocation points in each element, N_{ip}^n. In the numerical solutions, the degree of the Jacobi polynomials (i) in every element of N_{ip}^n can be varied. This method is essentially to provide numerical flexibility in the lower values of the r domain. In this regard, the dynamics for small drop coalescence is very fast, hence, more points are needed to accommodate small r values to provide numerical accuracy and speed in the initial stages of the simulation. The advantage of this feature in numerical scheme is that it allows one to place the collocation points strategically in the spectral element and as a result the computational time can be reduced effectively. Based on the value of N_{ip}^n for each element, a set of roots u_i^n and weights w_i^n are calculated. The roots are determined by Newton's method from the shifted Jacobi polynomial on the

interval [0 1]. The integration weights, w_i^n for each collocation point in the spectral elements are calculated using Gauss-Lobatto Quadrature from the roots of the Jacobi polynomials and its derivatives. The roots and weights calculated are used to approximate the integrals in the system equations. The overall properties of the gridding system and layout of the elements are depicted in Fig. 3. 4.

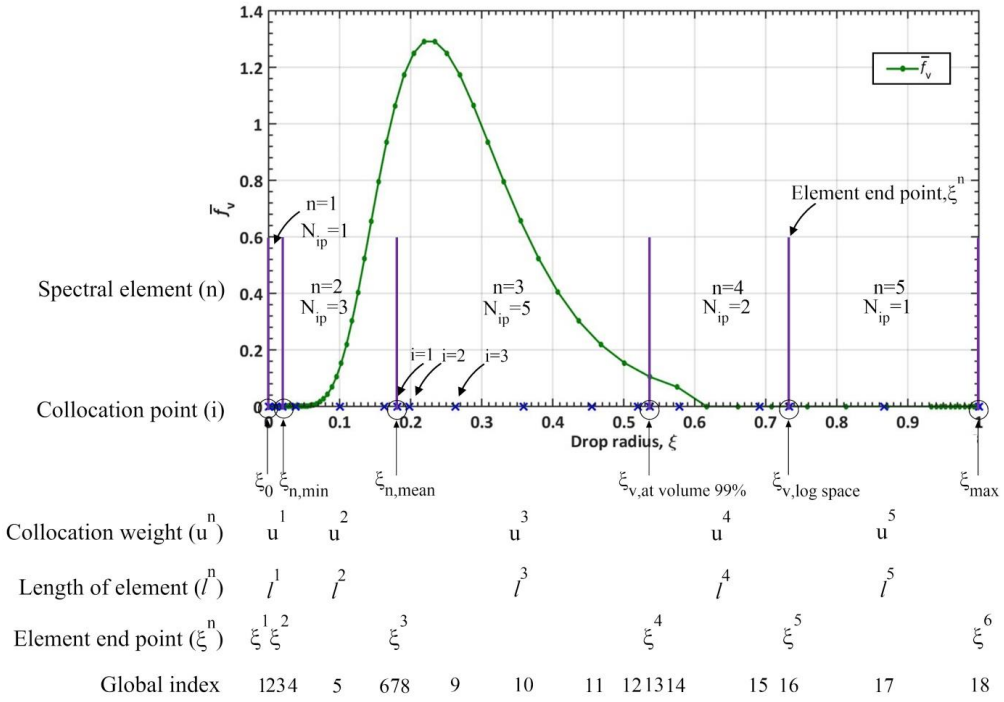

Figure 3.4 Schematic diagram of the gridding system and the overall layout of elements.

From the expression in Eqn. (3.42), the integration of volume density distribution and the first derivative weight of volume density distribution can be written as follows, respectively:

$$\int_0^1 \bar{f}_v d\xi = \sum_{n=1}^{N_t} \sum_{j=1}^{N_{ip}^n+2} \bar{f}_{v,j}^n \, l^n w_j^n \tag{3.43}$$

$$\left.\frac{d\bar{f}_{v,i}^{n}}{d\xi}\right|_{u_i^n} = \sum_{n=1}^{N_t} \sum_{j=1}^{N_{ip}^n+2} \frac{A_{i,j}^n}{l^n} \bar{f}_{v,j}^n \tag{3.44}$$

In the algorithm, the matrices containing the first and second orders derivatives weights are calculated from the roots of the Jacobi polynomial at each of the collocation point (i). The initial distributions can be interpolated onto the simulation grid once the simulation grid is constructed. The interpolation technique by Akima spline interpolation is selected due to its ability to produce smooth curves as well as its less proneness to wiggling (Salomon, 2011). To solve the system equation, the integration limits in the birth integral must be in the range of [0 1] and correspond to the orthogonal collocation weights constructed. Hence, the limits of the integrals have to be transformed and the number and volume density distributions will be then interpolated onto this new domain (coordinate system). To achieve this, the dimensionless volume and number density distributions (i.e., $\bar{f}_v$ and $\bar{f}_n$) are split into several sections in the spectral elements as shown in Fig. 3.5. The algorithm used cubic spline interpolation method due to the flexibility and suitability in the system to interpolate the birth integrals at every time step onto this new domain (i.e., $\bar{f}_{v_p}$ and $\bar{f}_{n_p}$). One of the attributes of this numerical scheme is that it enables the raw experimental data for an initial droplet size distribution to be employed. In addition, one feature of the spectral element method (n) introduced in the numerical scheme is it allows one to place the number of collocation points (i) in the system, strategically (details are discussed in Chapter 4 of this thesis). This feature will enable the model to solve the system equation at much lesser time without compromising the numerical stability and solutions.

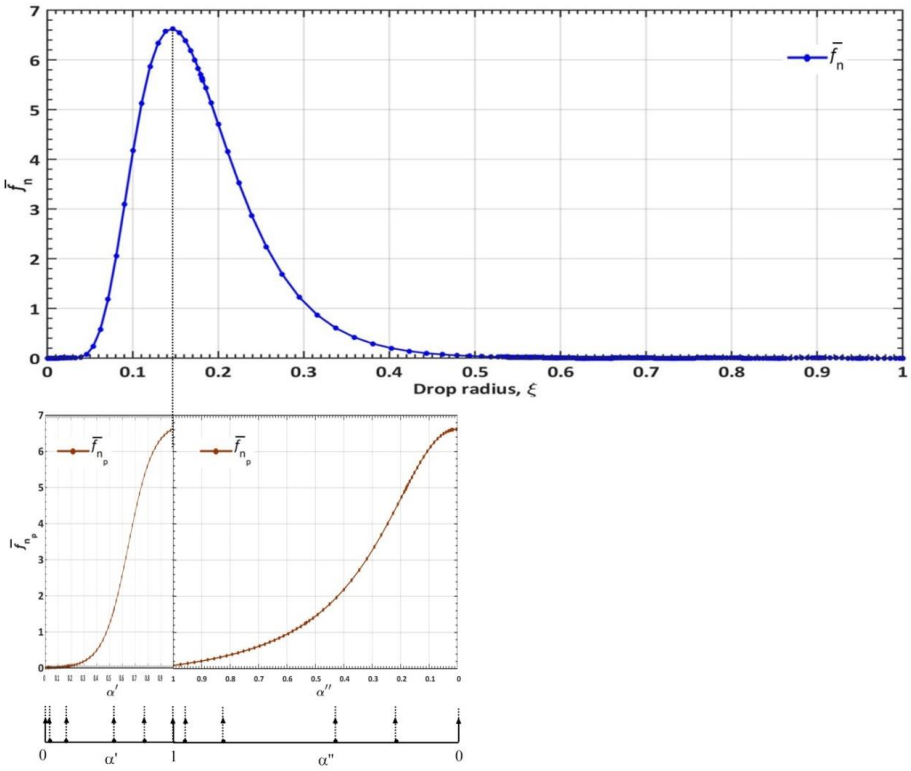

Figure 3.5 The schematic diagram of the interpolated number density distribution, $\bar{f}_{n_p}$ onto coordinate system of α' and α'' for the coalescence birth integral.

For the case of coalescence birth integral (Eqn. 3.25), new integration coordinate $\alpha'(\xi)$ is defined for every value of non-dimensional radius, ξ in the domain. Based on the upper limit in the coalescence birth integral, $\xi/\sqrt[3]{2}$, hence α' can be formulated as follows:

$$\alpha' = \frac{\xi'}{\xi/\sqrt[3]{2}} \tag{3.45}$$

Based on the expression in Eqn. (3.45) above, the dimensionless radius ξ' and its derivative $d\xi'$ with respect to α' can be expressed as follows, respectively:

$$\xi^{'} = \left(\frac{\xi}{\sqrt[3]{2}}\right)\alpha^{'} \tag{3.46}$$

$$d\xi^{'} = \left(\frac{\xi}{\sqrt[3]{2}}\right)d\alpha^{'} \tag{3.47}$$

Subsequently, by taking into account the relationship of $\xi^{''} = \left(\xi^3 - \xi^{'3}\right)^{1/3}$ from the volume conservation in the coalescence process and Eqn. (3.46), the following expression for $\alpha^{''}$ can be obtained:

$$\alpha^{''} = \left(2 - \alpha^{'3}\right)^{1/3} \tag{3.48}$$

The following are the expression for the coalescence birth and death processes in terms of discretization.

Discretized forms of birth and death rates due to coalescence, respectively:

$$P_{C_b}[\xi_i, \lambda] = \xi_i{}^3 \left(\frac{\xi_i}{\sqrt[3]{2}}\right) \sum_{n=1}^{N_t} \sum_{j=2}^{N_{ip}^n+2} \frac{\xi_i{}^2}{\xi_j^{''2}} \bar{r}_c \left(\xi_j^{'}, \left[\xi_i{}^3 - \xi_j^{'3}\right]^{1/3}\right) \bar{f}_{v_p',j}^n \bar{f}_{v_p'',j}^n l^n w_j^n \tag{3.49}$$

$$P_{C_d}(\xi_i, \lambda) = \bar{f}_{v,j}^n \sum_{n=1}^{N_t} \sum_{j=2}^{N_{ip}^n+2} \bar{r}_c \left(\xi_i, \xi_j\right) \frac{\bar{f}_{v,j}^n}{\bar{v}_j^n} l^n w_j^n \tag{3.50}$$

In Eqn. (3.49) above $\bar{f}_{v_p}$ represents the interpolated dimensionless volume density distribution. The equations are simulated for every collocation point across all spectral elements.

On the other hand, for the breakage case, similar principles are applied in which the limits for the breakage birth integral have to be scaled to range from 0 to 1. To achieve this, the cubic spline interpolation method is employed to interpolate the distribution onto the new coordinate grid as shown in Fig. 3.6.

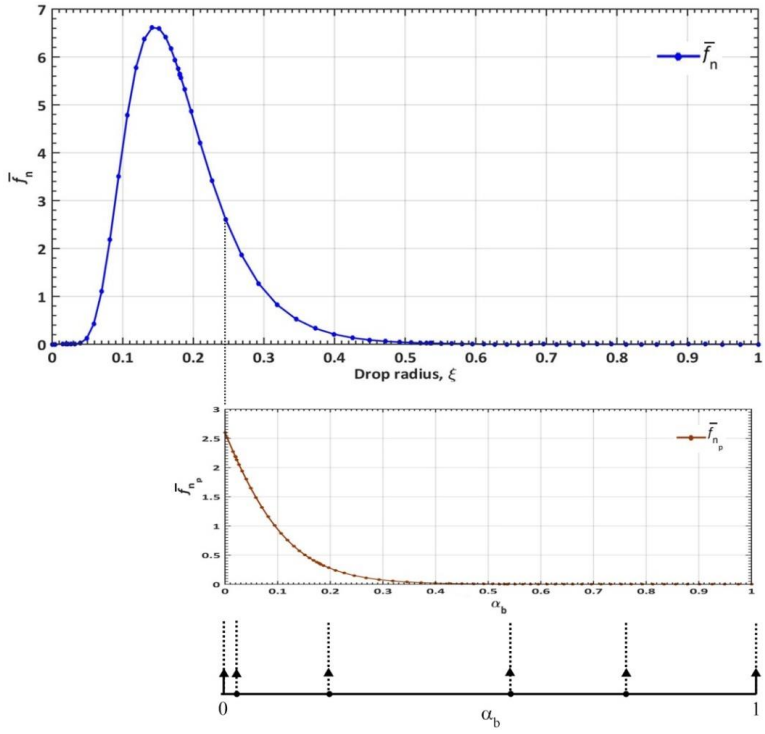

Figure 3.6 The schematic diagram of the interpolated number density distribution, $\bar{f}_{n_p}$ onto coordinate system of α_b for the breakage birth integral.

Similar to the coalescence case, a new integration coordinate $\alpha_b(\xi)$ is defined for every value of non-dimensional radius, ξ in the domain. In this context, ξ' along with its derivative $d\xi'$ with respect to α_b can be expressed as follows, respectively:

$$\xi' = \xi + (1 - \xi)\alpha_b \tag{3.51}$$

$$d\xi' = (1 - \xi)d\alpha_b \tag{3.52}$$

Hence, the discretized breakage birth and death can be written in the following form:

Discretized form of birth and death rates due to breakage, respectively:

$$P_{B_b}[\xi_i, \lambda] = [1 - \xi_i]\xi_i{}^3 \sum_{n=1}^{N_t} \sum_{j=1}^{N_{ip}^n+2} 2\bar{\beta}\left(\xi_i, \xi_j\right)\bar{g}\left(\xi_j\right)\bar{f}_{v_p,j}^n l^n w_j^n \tag{3.53}$$

$$P_{B_d}(\xi_i, \lambda) = \left[\bar{g}(\xi_i)\, \bar{f}_{v,j}^n\right] \tag{3.54}$$

Where in Eqn. (3.53), the expression of ξ_j can be written as follows:

$$\xi_j = \xi_i + (1 - \xi_i)\alpha_{b,j} \tag{3.55}$$

Finally, the resulting ODE with initial conditions is numerically solved using Gear's backward differentiation formulae (BDF) method and integrated for over the *z* coordinate.

3.12 Physical properties of the oil-water system

In this work, three different data sets supplied by Statoil were measured from the Focused Beam Reflectance Method (FBRM) for the turbulently flowing oil-water system. The data sets in this present work are classified as ge12275a, ge12279a, ge12284a. The physical properties of each of the data set are shown in Table 3.1. It is worth to note that, the major difference between the three data sets is the average flow velocity, U. As depicted in

Table 3.1, ge12284 represents the highest average flow velocity, U at 2.50 m/s, followed by ge12279a and ge12275a with 2.0 m/s and 1.70 m/s, respectively. These physical parameters of the system are used as inputs for the model simulations.

Table 3.1 The physical properties of the oil-water system in pipe

Parameter	Ge12275a	Ge12279a	Ge12284a	Descriptions
ϕ	0.30	0.30	0.30	Volume fraction
U	1.70 [m/s]	2.00 [m/s]	2.50 [m/s]	Average flow velocity
L	30 [m]	30 [m]	30 [m]	Length of the pipe
R_{max}	1000 [μm]	1000 [μm]	1000 [μm]	Upper bound of the radius domain
D	0.069 [m]	0.069 [m]	0.069 [m]	Diameter of the pipe
ρ_d	865 [kg/m^3]	865 [kg/m^3]	865 [kg/m^3]	Density of the dispersed phase
μ_d	177 [mPas]	169 [mPas]	152 [mPas]	Viscosity of the dispersed phase
ρ_c	1021 [kg/m^3]	1021 [kg/m^3]	1021 [kg/m^3]	Density of the continuous phase
μ_c	1.0 [mPas]	1.0 [mPas]	1.0 [mPas]	Viscosity of the continuous phase
σ	26.0 [mN/m]	26.0 [mN/m]	26.0 [mN/m]	Interfacial tension

3.13 Experimental data of droplet size distribution

When oil and water are transported through pipeline under vigorous shear rates, the formation of dispersion between oil and water will occur. In laboratory work, one of the techniques to record the droplet size distribution during dispersion process of oil and water in dynamic pipe transportation is using Focused Beam Reflectance Measurement (FBRM). The method of using FBRM probe has been studied in detail experimentally in horizontal pipes by

Placensia (2013) and Schümann (2016). Their research work suggested that FBRM probe can provide in-situ drop size evolution measurement through oil-water pipe flow. In this research work, the in-situ measurement of droplet size distribution profiles was obtained using two FBRM probes, one at the inlet and the other one at the outlet of the pipe. The advantages of using FBRM are droplet size variations in the dispersion process can be easily tracked compared to other instrument such as Particle Video Microscope (PVM) and real time measurement of particle size, count and shape can be obtained during oil-water emulsion in turbulent pipe flow (Placensia, 2013). FBRM utilizes highly precise chord length distribution (CLD), sensitive to particle size and count under real-time measurement without the need of sample preparation. FBRM is capable to measure droplet size in the range of 0.8-1000 μm which is ideal for in-situ droplet size analysis in real time (Dowding et al., 2001).

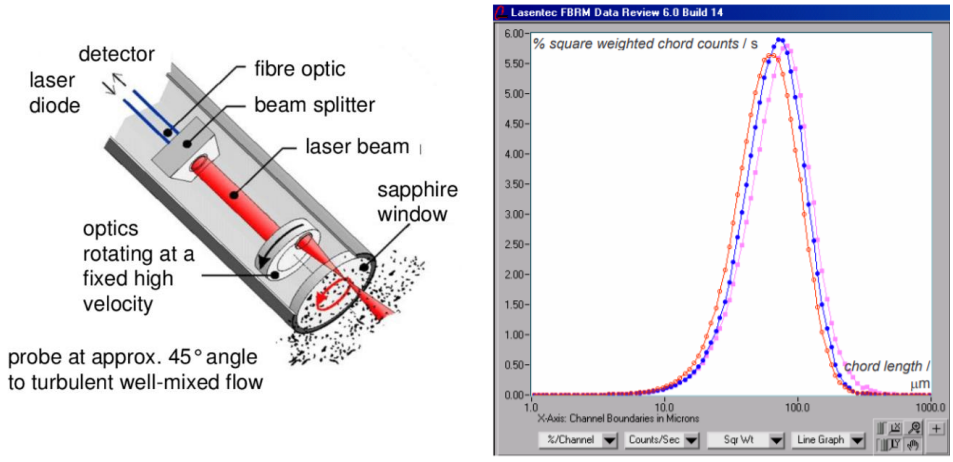

(a) (b)

Figure 3.7 FBRM Measurement (a) Schematic of FBRM probe tip (b) Particle size distribution using FBRM probe (Worlitschek and Buhr, 2005).

In general, the droplet size distribution was measured during the experimental work once the flow of oil-water dispersions reached a stabilized oil-water dispersion (steady state condition: stable pressure drop, mixture density, temperature and droplet size). In addition, the homogeneity of the mixture was also tracked by measuring the mixture density using the Coriolis flow meter during the dynamic flow of oil-water dispersion. These conditions must be met to ensure the quality of the droplet size distribution profiles obtained are accurate. It is to be noted that the experimental data of droplet size distributions were completely supplied by Statoil Research Centre, Trondheim. Hence, the validation of data was performed by the appointed researcher from Statoil. The samples of experimental data of drop size distribution is depicted in Fig. 3.8. FBRM probe is known to be one of the exceptional methods to measure real time droplet size distribution in liquid-liquid system. This is indicated by numerous studies on oil-water system using FBRM method (Maaß et al., 2011; Schümann et al., 2015; Schümann, 2016; Plasencia, 2013; Boxall et al., 2010; Naeeni and Pakzad, 2019).

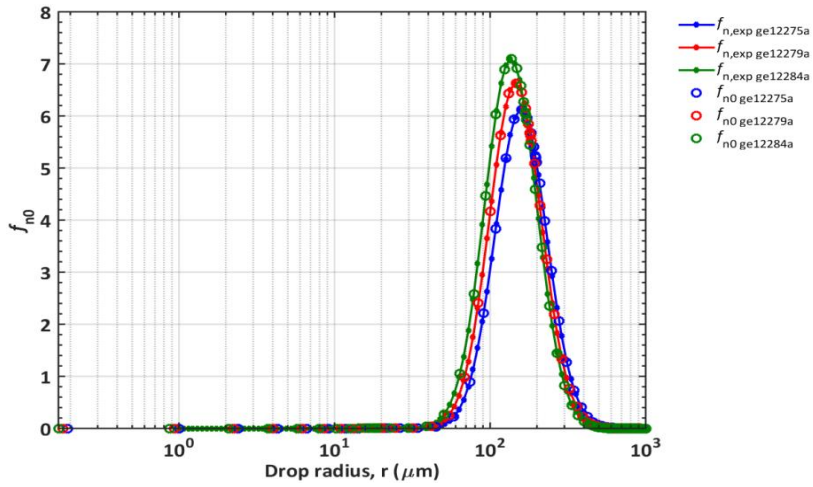

Figure 3.8 Samples of number density distributions for oil-water dispersions in pipe flow using FBRM probe. The $f_{n,exp}$ indicates experimental number distribution and $f_{n,0}$ the interpolated number distribution.

During the lab experiment of this current project, no other devices for droplet monitoring installed in the flow loop (pipes). However, to ensure the quality of the data obtained, direct comparison of drop size distribution profiles was established using PVM simultaneously with FBRM probes in a separate experiment in stirred tank setup using the same fluids. A conversion factor was derived from the comparison results of chord length distribution (CLD) from FBRM to real droplet size and distribution. Thorough discussion on the conversion factor can be found in research work by Khatibi, (2013) and Schümann et al. (2015). In addition, Boxall et al. (2010) also suggested that PVM probe is a useful tool for a calibration method with FBRM probe. For this present work, the shape of the droplet from experimental data is assumed spherical. Therefore, the mean chord length size measured by FBRM corresponds to the diameter of the droplet. However, there will be uncertainty in the chord length measured by the FBRM from the real droplet size distribution due to several factors such off-center crossing of the droplets by the laser beam, dense emulsions scattering of light by other droplets, variation in refractive index of the liquids, surface structures and properties such as translucent or transparent surface that may cause internal reflection and/or subsurface scattering (Vay et al., 2012; Schümann et al., 2015). Therefore, a general correction has been proposed by comparing simultaneous FBRM with PVM measurements in the same fluid system in order to reduce underestimation of the droplet size. The method allows combination of both techniques and produce real time and in situ measurement of correct droplet sizes although with an uncertainty of 50% (Schümann et al., 2015). This method introduced the log-normal distribution function to describe the droplet size distribution and it can be written as follows (Farr, 2013):

$$f(D) = \frac{1}{D\sigma\sqrt{2\pi}} exp\left\{\frac{[\ln(D/D_0)]^2}{2\sigma^2}\right\} \tag{3.56}$$

Where $f(D)$ is log-normal function of the droplet size distribution, D is the droplet size, σ is the dimensionless geometric standard deviation (the width of the distribution) and D_0 is a reference diameter setting the scale or the length scale of the distribution. According to Schümann et al. (2015), the conversion method from FRBM measurements has successfully reduced the error from factor of five to factor of two. Since the distribution of droplet size is commonly presented in logarithmic scale, thus, the error is considered within the acceptable limits. The conversion has been applied for this research work across all the measurements and the particle sizes measured from the three different experiments are observed to be in the range of 1.00 μm to 616.00 μm (refer to Table 3.2 and Fig. 3.8). It is worth to note that, the author is not involved in the experimental work. Hence, details about the experimental procedures and data preparations are exclusively owned by Statoil.

Table 3.2 Size range of the droplets from three different data sets of oil-water pipe flow

Experimental data set	Size range of the droplets
Ge12275a	1.00 μm – 616.00 μm
Ge12279a	1.00 μm – 575.00 μm
Ge12287a	1.00 μm – 537.00 μm

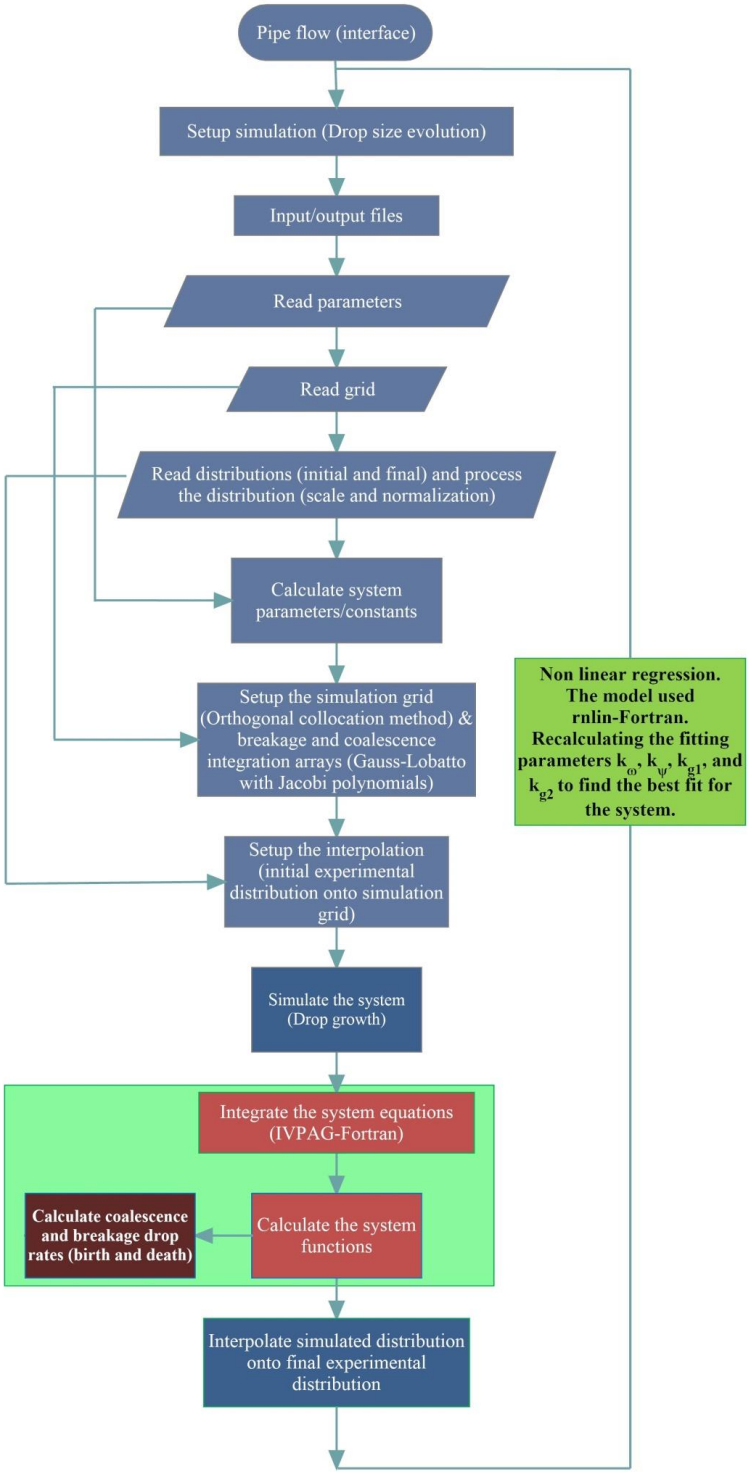

Figure 3.9 Overview of the simulation flow processes

3.14 Chapter summary

In this chapter, all models derived and formulated are showed and elucidated in each subsection. Since the system equations involve turbulent flows, assumptions have to be made (in early subsections) in order to simplify and enhance the simulation work. In the model formulation, possible methodologies are introduced using orthogonal collocation approach on finite elements as an alternative technique to solve the PBE. For any axial position in pipeline, the model developed from this method is able to predict the evolution of number and volume density distributions, the average drop radii for number and volume density distributions, the standard deviations of the droplet in terms of number and volume density distributions, and the rates of breakage and coalescence as well as total growth rates over a distance in pipes. For more comprehensive and details discussions of the model formulations and techniques, the reader is encouraged to refer to Part I of this manuscript in the attachment of Appendix B.

CHAPTER 4

4 RESULTS AND DISCUSSION (PART I)

4.1 Simulation results and discussion

In this thesis, the results and discussion are divided into two main parts: (i) the model behaviour and parametric effects and (ii) regression of the experimental pipe flow data: comparison between simulation and experimental data. The first part (Part I) is discussed in this chapter – Chapter 4, while the second part (Part II) is discussed in the next chapter – Chapter 5. In these two chapters (i.e., Chapter 4 and Chapter 5), two manuscripts are prepared for each of the results discussed in Part I and Part II. Including the paper prepared in Chapter 3, there are three manuscripts altogether for this research work and they can be found in the Appendix B, Appendix C, and Appendix D of this thesis, respectively.

4.2 Part I: The model behaviour and parametric effects

In liquid-liquid systems, many physical properties of the dispersion are strongly related to the drop size distribution of the dispersed phase. In pipe flow, any changes in the drop size distribution may affect the flow pattern and pressure drop significantly. Hence, the evaluation and study of parametric effect is important because coalescence and breakage processes in liquid-liquid turbulent pipe flow are strongly dependent on the physical properties of the continuous and dispersed phase, state of flow, and mixing conditions in the system (Solsvik et al., 2015). For this purpose, the model is investigated under various parametric effects to provide insights toward the overall model behaviour. For these investigations, the following physical properties as shown in Table 4.1 are employed as an input for the simulation.

Table 4.1 Input parameters for the simulation

Parameter	Value	Descriptions
ϕ	0.30	Volume fraction
U	2.00 [m/s]	Average flow velocity
L	1500 [m]	Length of the pipe
R_{max}	1000 [μm]	Upper bound of the radius domain
D	0.069 [m]	Diameter of the pipe
ρ_d	865 [kg/m^3]	Density of the dispersed phase
μ_d	169 [mPas]	Viscosity of the dispersed phase
ρ_c	1021 [kg/m^3]	Density of the continuous phase
μ_c	1.0 [mPas]	Viscosity of the continuous phase
σ	26.0 [mN/m]	Interfacial tension

Depicted in Fig. 4.1 is the plot of experimental number density distribution, $f_{n,exp}$ at initial position in the pipe ($z = 0$) as a function of drop radius, r. The distribution is then compared against the interpolated initial number density distribution, $f_{n,0}$. On the same figure, the experimental and interpolated volume density distributions, $f_{v,exp}$ and $f_{v,0}$ respectively, are also plotted against the drop radius, r. Essentially, the comparison between the experimental and interpolated distributions is to map the experimental data points onto the collocation points that consist of simulation grid. In this respect, the interpolation was showing good results wherein the interpolated initial number and volume density distributions, $f_{n,0}$, $f_{v,0}$ are perfectly fits with the experimental data points consistently.

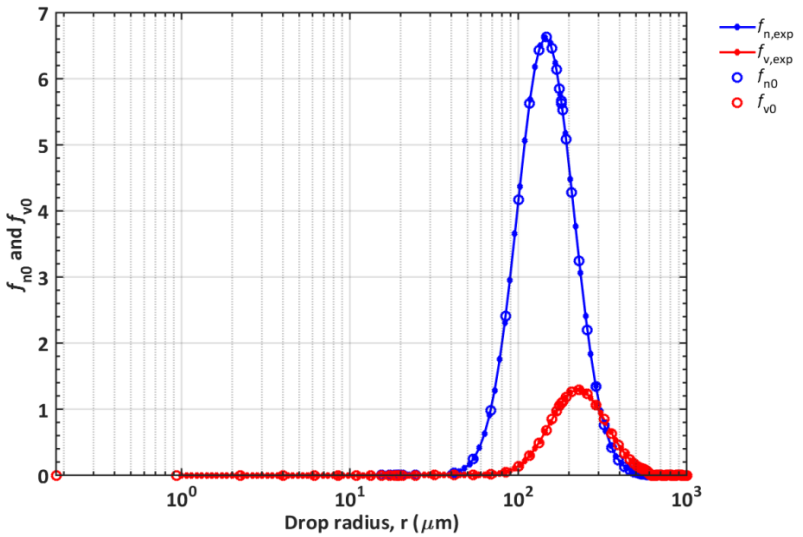

Figure 4.1 Initial experimental number and volume density distributions, $f_{n,exp}$, $f_{v,exp}$ in blue and red dotted lines, and interpolated initial number and volume distributions**,** $f_{n,0}$, $f_{v,0}$ in blue and red circles, are plotted as a function of droplet radius, r.

4.2.1 Base case

In this present work, a base case is prepared as a reference to give an overview of how the system behaves with the given set of input parameters. For this purpose, the following fitting parameters are used as shown in Table 4.2.

Table 4.2 Base case: fitting parameters

Parameter	Value	Descriptions
k_ω	1.00 e -04	Fitting parameter for coalescence frequency expression
k_ψ	1.00 e -03	Fitting parameter for coalescence efficiency expression
k_{g_1}	5.00 e -01	Fitting parameter for breakage frequency expression
k_{g_2}	5.00 e -01	Fitting parameter for breakage efficiency expression

From the set of fitting parameters above, the evolution of the number and volume density distributions (f_n and f_v) are simulated and depicted in Fig. 4.2. From the figure, the dynamic evolution of f_n and f_v of the base case are plotted in terms of radius, r, throughout nine different axial (z) locations in the pipeline. The number density distribution, f_n in Fig. 4.2(a) demonstrates that there is a small quantity of larger size droplets at the beginning of the pipeline and the magnitude of f_n grows higher as the droplets evolve toward the end of the pipeline. This is true considering that the larger droplets present at the beginning of the pipeline are more likely to break than smaller droplets. This indicates that breakage is dominant in the system at short axial distances. Similarly, for volume density distribution, f_v, the magnitude increases towards the end of pipeline. This shows that, coalescence balances breakage as axial (z) increases and the distribution reaches equilibrium. An increasing magnitude of drops evolution (f_v) as shown in Fig. 4(b) suggests that, the distribution is narrower at equilibrium relative to the initial condition, in which there are large numbers of small droplets formed at the end of the pipeline.

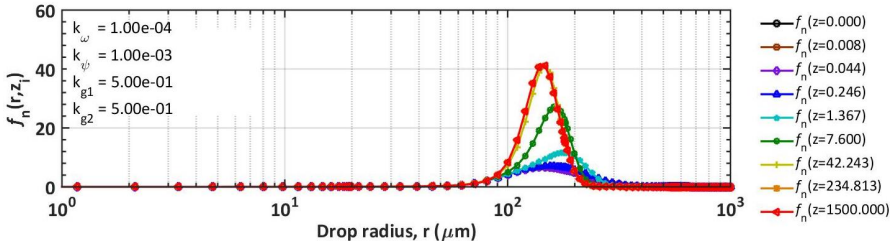

(a)

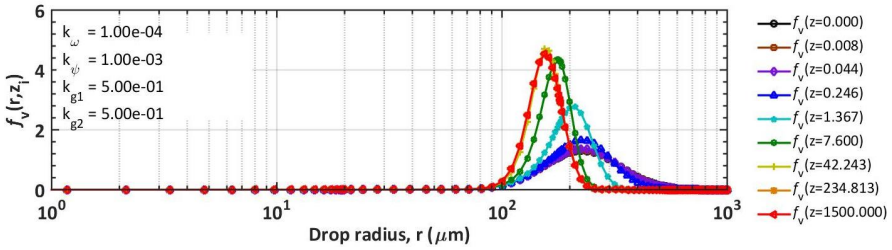

(b)

Figure 4.2 Evolution of (a) number density distribution, f_n and (b) volume density distribution, f_v along the pipeline as a function of drop radius, r. The fitting parameters used are shown on top left corner of the plots for the base case.

On the other hand, Fig. 4.2 illustrates the dynamic evolution of mean radii in terms of number and volume density distributions (μ_N and μ_V) as a function of axial position, z of the pipe for the base case. The mean radii in Fig. 4.3 depict that, μ_N and μ_V are decreasing as the droplets travel through the 1500 m pipeline. This suggests that, breakage is initially dominant over coalescence for this set of fitting parameters and initial distribution (i.e., base case) as the droplets evolve towards the end of the pipeline. It is worth noting that the mean radii of μ_N and μ_V are equilibrated after they surpass the 1 m of pipeline. As this takes place, the mean radii have reached constant values in which the system is in balance between the breakage and coalescence processes particularly, at the equilibrium state. Similar events are found to occur in the standard deviations for number and volume density distribution, σ_N and σ_V, as shown in Fig. 4.3(b). The magnitudes for both σ_N and σ_V are gradually decreasing as they approach the end of the pipeline. They are also found to be levelled once the system reaches the equilibrium.

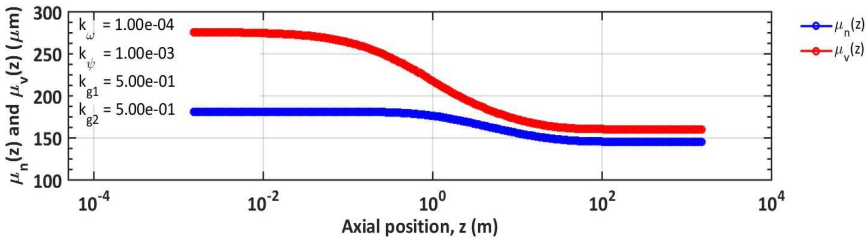

(a)

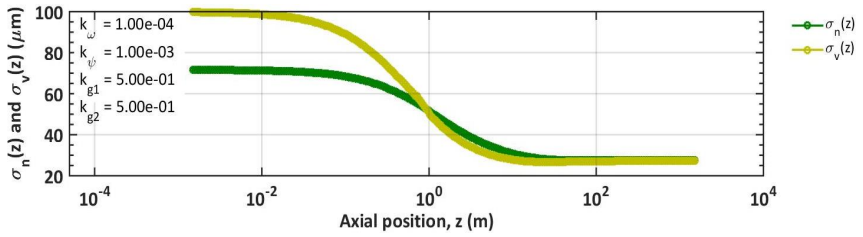

(b)

Figure 4.3 The plot of: (a) the average radii of number density distribution, μ_N and volume density distribution, μ_V as a function of axial position, z in the pipe, and (b) the standard deviations of number density distribution, σ_N and volume density distribution, σ_V as a function of axial position, z in the pipe. The fitting parameters used are shown on top left corner of the plot for the base case.

To further evaluate the drop growth from the PBE model, the total coalescence and breakage rates, R_{C_t} and R_{B_t} are plotted as a function of drop radius r for nine different locations as shown in Fig. 4.4. In this figure, the positive part of the curve indicates the birth and the negative part of the curve represents the death by virtue of coalescence and breakage processes. In Fig. 4.4(a), the total coalescence rate is lower in magnitude at the beginning of the pipeline and as axial position, z increases, the rate gets higher. This suggests that, coalescence rate is stronger approaching the end of the pipe and somewhat weaker at the beginning stage in the pipe. This is true considering the large number of smaller droplets presence towards the end of the pipe. Hence, coalescence is expected to increase towards the end of the pipeline due to the fact that small droplets are more likely to coalesce, and the larger number density promotes collision, while larger droplets tend to rupture. Conversely, the total breakage rate, R_{B_t} in Fig. 4.4(b) is found to reduce in magnitude as the breakage process moves towards the end of the pipeline. Moreover, it is expected that R_{B_t} is found to be greater at low z values because larger droplets at the onset of the pipeline are easier to

break and rupture than smaller droplets at the end. Apart from that, the birth rate due to breakage shown in Fig. 4.4(b) is observed to be higher (i.e., $R_{B_t} \approx 2000$) than the death rate by breakage (i.e., $R_{B_t} \approx$ -1200). This is primarily because of the difference in the number of larger droplets present at the beginning of the pipeline than at the end which will significantly affect the breakage frequency and efficiency.

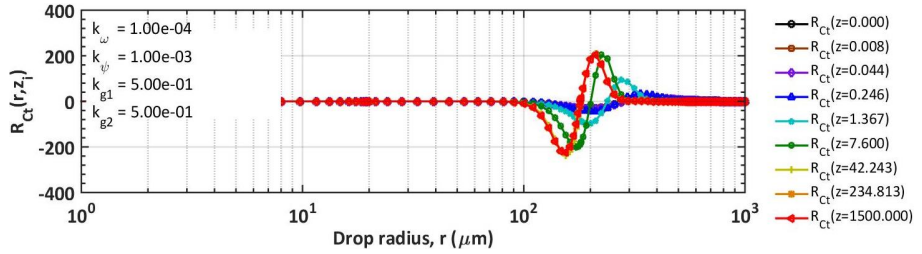

(a)

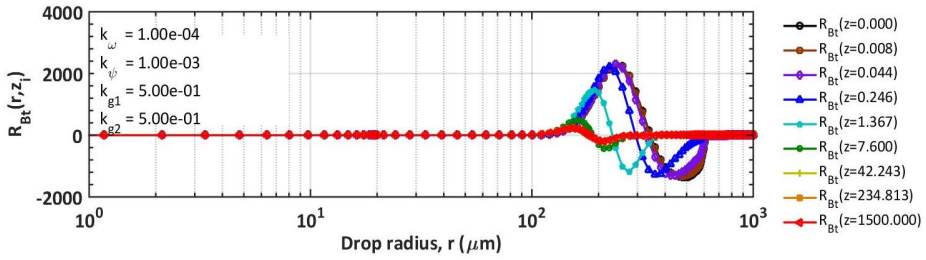

(b)

Figure 4.4 Evolution of (a) total coalescence rate, $R_{C_t}$and (b) total breakage death rate, R_{B_t}. Both rates are plotted for the base case parameter set and as a function of droplet radius, r at nine different locations from 1500 m pipe length. The fitting parameters used are shown on top left corner of the plots for the base case.

4.2.2 Numerical techniques and model behavior

Prior to analysis on various parametric effects, the model performance is assessed in terms of the proposed numerical technique (orthogonal collocation method) as described in

Chapter 3 of this thesis to give a comprehensive understanding of the overall model behavior. These results will complement the assessment made in the various parametric effects discussed in the following section 4.3 and show the capability of the model, thoroughly. To achieve this, the following fitting parameters are set as shown in Table 4.3 to demonstrate the drop rates and model behavior.

Table 4.3 Fitting parameters

Parameter	Value	Descriptions
k_{ω}	1.70 e -03	Fitting parameter for coalescence frequency expression
k_{ψ}	1.50 e -03	Fitting parameter for coalescence efficiency expression
k_{g_1}	2.50 e -02	Fitting parameter for breakage frequency expression
k_{g_2}	3.50 e -01	Fitting parameter for breakage efficiency expression

From the fitting parameters suggested in Table 4.3 above, the following results are simulated to highlight the evolution of number and volume density distributions (f_n and f_v), the mean radii in terms of number and volume density distributions (μ_N and μ_V), and total breakage and coalescence rates (R_{B_t} and R_{C_t}). Fig. 4.5 shows the dynamic evolution of number density distribution, f_n and volume density distribution, f_v throughout nine different axial (z) locations in the pipeline. As opposed to the base case, the results from the dynamic evolution of number density distribution, f_n in Fig. 4.5(a) shows that there is a large number of small size droplets present at the beginning of the pipeline ($z = 0$ m) and the magnitude gets lower as the droplets evolve through the end of the pipeline ($z = 1500$ m). These results are expected since the number of small droplets present at the beginning is higher. Hence, the chances of droplets to coalesce and merge into larger droplets are greater. This will result in coalescence being dominant in the early stage of the pipeline. However, as z increases, the

growth rate reduces due to breakage growing in dominance. Similar to the case in f_n, the volume density distribution, f_v shown in Fig. 4.5(b) is found to decrease particularly towards the end of the pipeline. This indicates that, coalescence and breakage narrow the drop size distribution relative to the initial condition. With a wide initial drop size distribution of small drops, the droplets are expected to have longer contact time than the drainage time, thus enhancing the coalescence process between droplets. Subsequently, the breakage process is becoming stronger as larger droplets formed from the coalescence process earlier begin to rupture. This is due to the fact that larger droplets are prone and easy to breakup than small droplets.

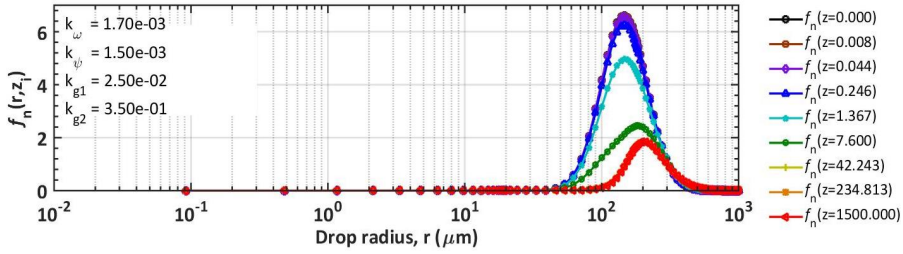

(a)

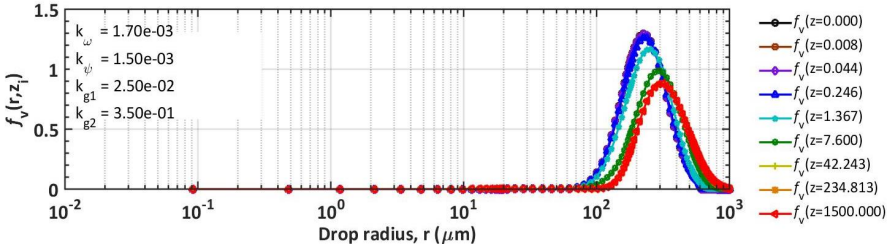

(b)

Figure 4.5 Evolution of (a) number density distribution, f_n and (b) volume density distribution, f_v along 1500m pipeline as a function of drop radius, r. The fitting parameters used are shown on top left corner of the plots.

Further, the average radii (μ_N and μ_V) and the standard deviations (σ_N and σ_V) of the number density and volume density distributions are plotted as a function of axial position in the pipe, z as depicted in Fig. 4.6(a) and (b), respectively. The plots provide an intriguing insight on the dynamic evolution of the mean radii during the oil-water fully dispersed flow in a very long-distance pipeline (i.e., 1500 m). In Fig. 4.6(a), the mean radii for both number and volume density distributions (μ_N and μ_V) are found to increase approaching the end of the pipeline. The same trend is observed for the standard deviations, σ_N and σ_V as depicted in Fig. 4.6(b). The increase in the magnitude of mean radii and standard deviations suggest that coalescence is dominant over breakage for this set of fitting parameters as the mixture liquids travel through 1500 m pipeline. The results suggest that the forces particularly, the kinetic energy involved in deforming the droplets are not sufficiently large enough to overcome the surface energy of the droplets which results in an increase in the mean radii and standard deviations (coalescence dominating) instead of a decrease (breakage dominating). It is also worth noting that the magnitude of the mean radii (μ_N and μ_V) as well as the standard deviations (σ_N and σ_V) are growing in the initial stage of the pipeline and are equilibrated approaching 10^2 m of the pipeline.

It is also important to note that the determination of average droplet size in liquid-liquid dispersion is imperative because it provides a useful parameter for droplet movement describing the sedimentation and coalescence profiles (Jeelani and Hartland, 1998; Yu and Mao, 2004). Apart from that, the maximum value of mean radii (towards the end of the pipeline) in Fig. 4.6(a) indicates the characteristic radius, $R_{characteristic}$ of the system. The characteristic radius is determined once the system reaches an equilibrium at which the breakage and coalescence processes are said to have balanced.

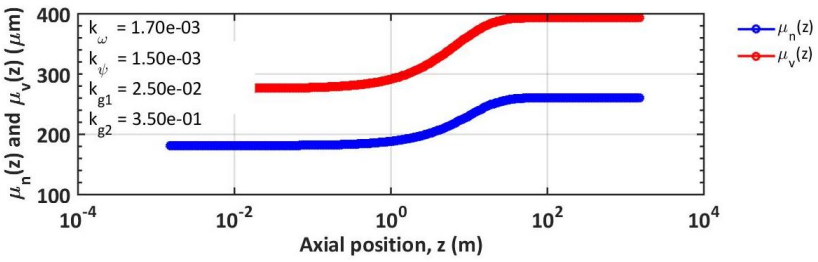

(a)

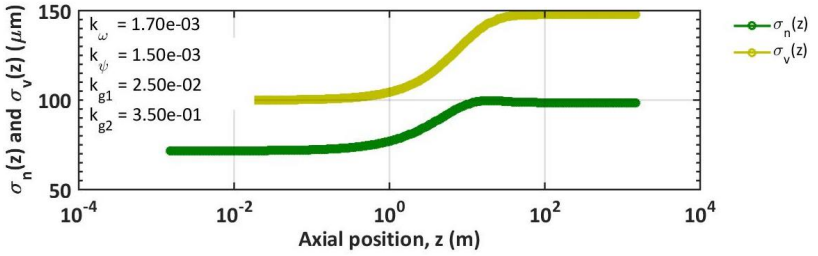

(b)

Figure 4.6 The plot of: (a) mean radii of number density distribution, μ_N and volume density distribution, μ_V as a function of axial position, z in the pipe and (b) standard deviations of number density distribution, σ_N and volume density distribution, σ_V as a function of axial position, z in the pipe. The fitting parameters used are shown on top left corner.

4.2.2.1 The importance of conversion from f_n to f_v

It is important to note that, in this work, the solutions of PBE are solved in terms of the volume density distribution, f_v instead of number density distribution, f_n. This can be done by converting the system equation as depicted in Eqn. 3.25 of Chapter 3. To elucidate the importance of volume density distribution, f_v in solving the PBE, we employed two different initial distributions in the system. The primary reason is to compare the evolution of total number density function, $\bar{N}_d$ and volume fraction, ϕ across 1500m pipeline as shown in Fig. 4.7. In this comparison, the three different initial distributions are named as case I, case II, and case III. The main difference between the initial distributions in case I, case II, and

case III is the average flow velocity, U in the pipes. The average flow velocity of the liquid-liquid system in the pipes increases from case I to case III. Fig. 4.7 demonstrates the comparison between the total number density function, $\overline{N}_d$ and the volume fraction, ϕ in terms of axial position, z in the pipeline for all the cases employed (i.e., cases I, II, and III). The results in Fig. 4.7(a) show that, at increase number of cases (i.e., cases I, II, III), the total number density as a function of axial position, $N_d(z)$ decreases in terms of the magnitude towards the end of the pipeline. While, the results of volume fraction, ϕ for all the cases simulated remain constant throughout the pipeline as depicted in Fig. 4.7(b). This clearly shows that, the magnitude of number density distribution f_n can alter significantly during the drop growth compared to the magnitude of volume density distribution, f_v. In this respect, one can have an insight that solving the PBE for dynamic evolution of drop size density distribution in liquid-liquid system over a distance in pipe is more effective in the form of volume density distribution, f_v instead of number density distribution, f_n (which has been widely used in the literature) due to its consistent magnitude over time. This is primarily crucial in order to ensure that the convergence criteria for the absolute and relative error tolerances of the numerical integrator are consistent with the magnitude of the dependent variable over the entire simulation.

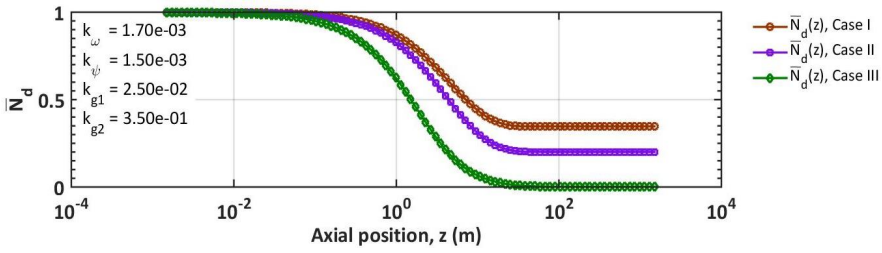

(a)

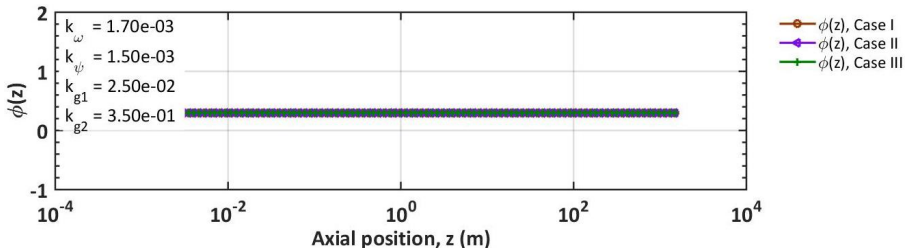

(b)

Figure 4.7 The evolution of (a) dimensionless total number density function, $\bar{N}_d$ as a function of axial position, z and (b) the volume fraction of droplets, ϕ as a function of axial position, z. Both are plots in terms of case I, case II and case III of different initial distributions. The fitting parameters used are shown on top left corner of the plots.

4.2.2.2 Error analysis on the numerical methods

In this present work, the error from the mass balance (ϕ) and the volume density distribution, f_v at equilibrium are assessed to give an overview of the overall system behaviour. To achieve this, four cases are prepared with different model behaviors: case I (coalescence-dominated), case II (breakage-dominated), case III (fast dynamics), and case IV (slow dynamics). Each of the cases is set with different fitting parameters to elucidate the model behavior in which, case I employs higher magnitude of and k_{g_1} and k_{g_2} (higher mean radii), case II employs lower magnitude of k_{g_1} and k_{g_2} (lower mean radii), case III employs greater magnitude of k_ω and k_{g_1}(faster equilibrium), and case IV employs smaller magnitude of k_ω and k_{g_1}(slower equilibrium). Fig. 4.8 (a), (b), (c), and (d) indicate the mass balance error analysis for case I, II, III, and IV at different total number of spectral elements, N_t and total number of points, i_{tot}. In general, the error is greater as lower number of points are allocated and conversely for higher number of points, regardless of the total number of spectral elements employed ($N_t = 1$ or $N_t = 6$). However, the error is found to be significantly lower when total number of spectral elements, $N_t = 6$ is used instead of $N_t =$

1. Increment in the number of total collocation points, i_{tot} particularly, at $N_t = 6$ has effectively decreased the magnitude of the mass balance error. This indicates that, spectral element method of $N_t = 6$ is more efficient in numerical solutions for all types of cases (i.e., coalescence and breakage dominated systems and slow and fast dynamics systems) due to the strategic placement of collocation points in the system. Ideally, increase in number of points provides efficient numerical solutions (lower mass balance error) as sufficient number of points are places to accommodate the droplets evolution over the axial position, z, but at the cost of longer simulation times.

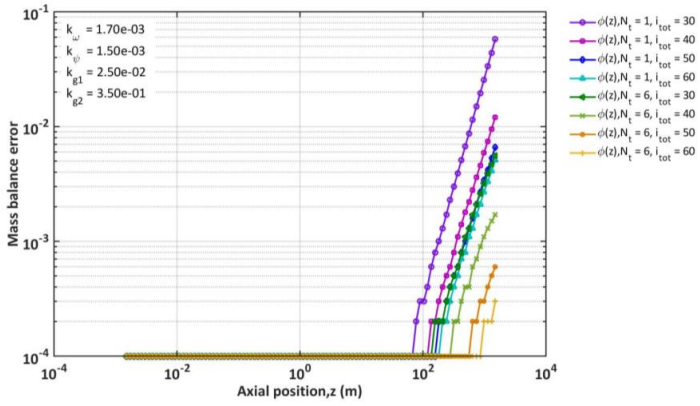

(a)

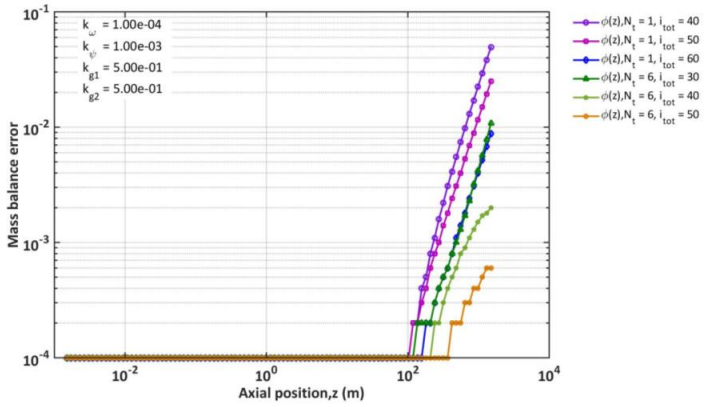

(b)

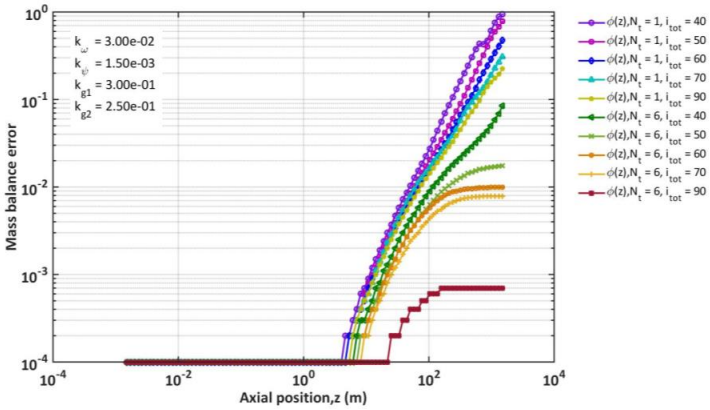

(c)

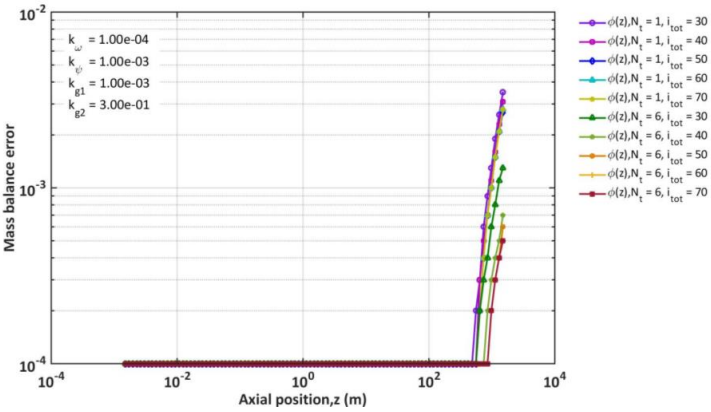

(d)

Figure 4.8 The mass balance error: (a) case I – coalescence dominated, (b) case II – breakage dominated, (c) case III – fast dynamics, and (d) case IV – slow dynamics.

On the other hand, the volume density distribution (f_v) at equilibrium with different total number of spectral elements (N_t) and collocation points (i_{tot}) employed are demonstrated in Fig. 4.9 (a), (b), (c), and (d) for all cases (coalescence-dominated, breakage-dominated, fast dynamics, and slow dynamics), respectively. The volume density distribution (f_v) in Fig. 4.9 shows that the distributions at equilibrium are varied for all cases in terms of different spectral elements methods (i.e., $N_t = 1$ and $N_t = 6$) and collocation points. The

magnitude of f_v is found to be maximum when higher number of collocation points are allocated for both spectral element methods ($N_t = 1$ and $N_t = 6$) in all cases. On the contrary, if a smaller number of points are employed, the magnitude of f_v reduces due to the losses in mass balance, particularly in case III of fast dynamics system as shown Fig. 4.9(c). In fast dynamics system, the event of small drop coalescence and large drop breakup especially at equilibrium occurs at a faster rate. Hence, more points are required in order to accommodate the stiffness of the numerical system in the r domain. In this respect, enhanced numerical accuracy can be expected. Furthermore, the results of f_v complement with the error results obtained in the mass balance errors depicted Fig. 4.8. In this error analysis of the system from case to case basis, both methods $N_t = 1$ and $N_t = 6$ are found to reduce the errors in the numerical system as higher number of collocation points are set. However, the spectral element method ($N_t = 6$) is considered the best method to be employed in the model due to the performance of spectral element methods $N_t = 6$ is much better and efficient than single element method $N_t = 1$. The spectral element methods, $N_t = 6$ produced the lowest error than one element method ($N_t = 1$) irrespective of the total number of points (i_{tot}) employed. In orthogonal collocation method, for each of the spectral element assigned, one can strategically place the number of points to specifically account for the stiffness in the numerical system. For instance, if the dynamics for small drop coalescence is very fast particularly at lower r domain, hence, more points can be strategically placed in this domain to accommodate these small r values (due to fast coalescence process) instead of uniformly distributed (placement) collocation points as shows in the single element method ($N_t = 1$). In this respect, the numerical accuracy and speed (refer to Table 4.4) can be enhanced due to strategic distribution of collocation points in the system.

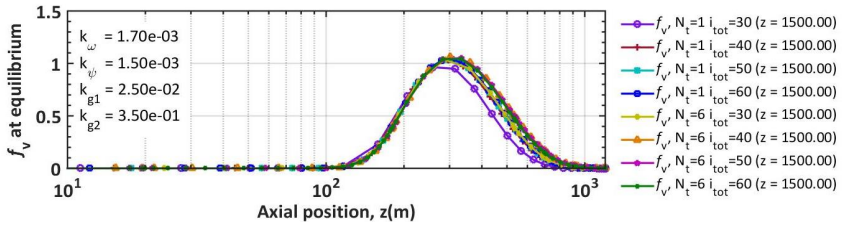

(a)

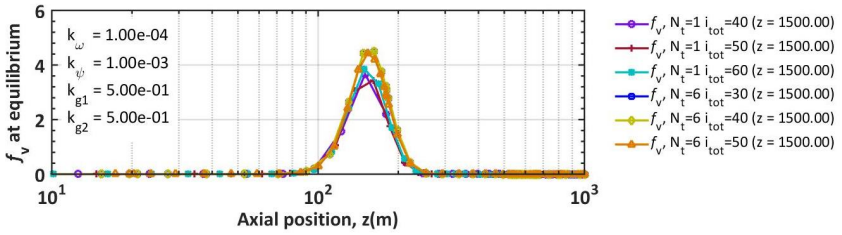

(b)

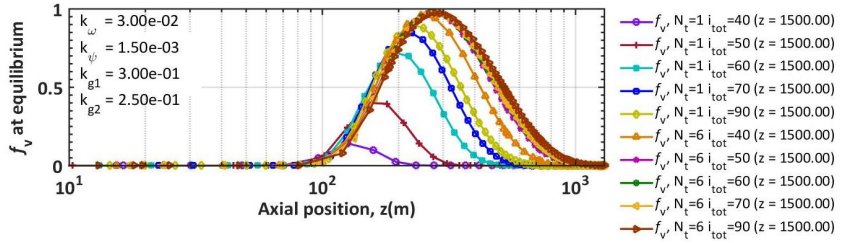

(c)

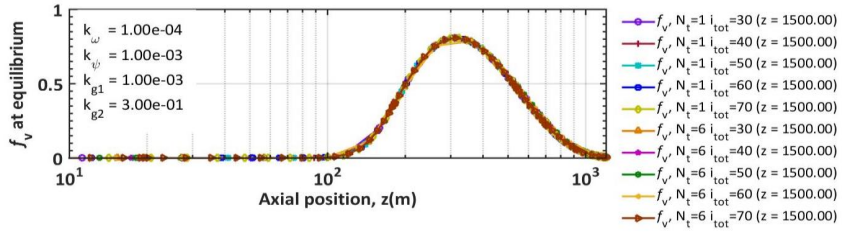

(d)

Figure 4.9 The volume density distribution (f_v) at equilibrium: (a) case I – coalescence dominated, (b) case II – breakage dominated, (c) case III – fast dynamics, and (d) case IV – slow dynamics.

Apart from that, CPU time and simulation time for all the cases studied (i.e., case I, II, III, and IV) at $N_t = 6$ and $N_t = 1$ are also investigated as depicted in Table 2. The results suggest that, a system with spectral elements (i.e., sub-domain of $N_t = 6$) provide lower CPU time and faster simulation time. This is true considering the fact that, strategic numbers of collocation points placed at different spectral elements promote faster numerical convergence. In other words, one may choose $N_t = 1$ and higher number i_{tot} but at cost of CPU expensive and longer simulation time. However, with the spectral element scheme, low CPU time and faster solutions can be expected as well as low errors as discussed earlier.

Table 4.4 CPU time and real time usages for given cases of N_t and i_{tot}

Case	CPU time (s)	Simulation time (s)
Case: coalescence dominated		
$N_t = 1, i_{tot} = 30$	34.5	33
$N_t = 1, i_{tot} = 40$	43.4	41
$N_t = 1, i_{tot} = 50$	47.5	45
$N_t = 1, i_{tot} = 60$	51.6	49
$N_t = 6, i_{tot} = 30$	33.8	31
$N_t = 6, i_{tot} = 40$	42.3	40
$N_t = 6, i_{tot} = 50$	45.3	43
$N_t = 6, i_{tot} = 60$	49.8	47
Case: breakage dominated		
$N_t = 1, i_{tot} = 40$	42.2	34
$N_t = 1, i_{tot} = 50$	47.2	37
$N_t = 1, i_{tot} = 60$	55.0	41

$N_t = 6, i_{tot} = 30$	37.3	29
$N_t = 6, i_{tot} = 40$	41.9	33
$N_t = 6, i_{tot} = 50$	45.9	35
Case: fast dynamics		
$N_t = 1, i_{tot} = 40$	42.5	37
$N_t = 1, i_{tot} = 50$	44.8	39
$N_t = 1, i_{tot} = 60$	52.7	47
$N_t = 1, i_{tot} = 70$	62.5	57
$N_t = 1, i_{tot} = 90$	87.2	76
$N_t = 6, i_{tot} = 40$	40.0	35
$N_t = 6, i_{tot} = 50$	41.6	36
$N_t = 6, i_{tot} = 60$	49.2	44
$N_t = 6, i_{tot} = 70$	57.2	52
$N_t = 6, i_{tot} = 90$	81.6	71
Case: slow dynamics		
$N_t = 1, i_{tot} = 30$	32.2	28
$N_t = 1, i_{tot} = 40$	36.0	32
$N_t = 1, i_{tot} = 50$	40.2	35
$N_t = 1, i_{tot} = 60$	49.5	42
$N_t = 1, i_{tot} = 70$	56.8	45
$N_t = 6, i_{tot} = 30$	30.1	26
$N_t = 6, i_{tot} = 40$	34.8	30
$N_t = 6, i_{tot} = 50$	39.5	34
$N_t = 6, i_{tot} = 60$	45.5	39

$N_t = 6, i_{tot} = 70$	56.0	45

4.2.3 Parametric effects

Analysis of the parametric effects would enhance the understanding of the model behavior in turbulently flowing liquid-liquid dispersions particularly for oil-water flow in pipes. To investigate the system behavior on the various parametric effects, the fitting parameters are set to a new value as depicted in Table 4.5 below. In this new set of fitting parameters, the variations of parameters in terms of energy dissipation rate, ε and volume fraction, ϕ are assessed and evaluated.

Table 4.5 New fitting parameters

Parameter	Value	Descriptions
k_ω	1.70 e -03	Fitting parameter for coalescence frequency expression
k_ψ	1.50 e -03	Fitting parameter for coalescence efficiency expression
k_{g_1}	2.50 e -02	Fitting parameter for breakage frequency expression
k_{g_2}	3.50 e -01	Fitting parameter for breakage efficiency expression

These parameters (i.e., ϕ, and ε) are crucial and contribute significantly to the experimental strategies and design of the liquid-liquid two-phase pipe flow. For instance, in experimental study of the overall drop size behaviour in two phase pipe flow, the typical approaches are by changing and/or varying the fluid volume fraction (i.e., ϕ) and the flow conditions (i.e., U) of the system. In regard to the fluid volume fraction, altering the volume fraction, ϕ of the dispersed phase will significantly affect the oil-water emulsion stability (Meybodi et al., 2014). While, in the context of flow condition, changing the velocity is the preferred method because of the direct influence on the turbulent kinetic energy in the system

which eventually leads to varying the energy dissipation rate, ε. The rate of energy dissipation is estimated based on the newly proposed energy dissipation rate ε by Jakobsen (2014). The rate is utilized based on the reason that the wall shear is the primary source of turbulence production. Fig. 4.10 shows the effect of various energy dissipation rates, ε during the drop size evolutions in terms of mean drop radii for number and volume density distributions, μ_N, and μ_V. The results in Fig. 4.10 show that, at increase number of energy dissipation rate, ε, the mean drop radii decreased and the magnitude is consistent approaching the end of 1500m pipeline. Conversely, at low energy dissipation rate of $\varepsilon = 2.0$ m^2/s^3 the mean radii are observed to be increased. These events are true considering that the energy dissipation rate, ε is one of the primary mechanisms that control the breakage frequency as depicted in Eqn. (3.17). Hence, due to an effect of small mean radii, the system will be breakage dominated and high energy dissipation rate, ε. Conversely, if the mean radii are large in magnitude, the system indicates coalescence dominated and low energy dissipation rate, ε. As breakage becomes stronger due to increase in energy dissipation rate, ε, more droplets will likely break into smaller droplets which leads to small magnitude in mean radii as depicted in Fig. 4.10 (a) and (b). This is due to the increase in kinetic energy in the system that eventually overcomes the surface energy of the droplets. Kumar et al., (1991) explained that, droplets will deform and break under the influence of turbulent inertial stresses. In this premise, increase in turbulent stresses will produce higher energy dissipation rate as a result of high Reynolds number and consequently force the droplet to break and rupture. Solsvik et al., (2017) also agreed that all droplets will break in turbulent liquid flows under high Reynolds numbers and energy dissipation rate. Although, turbulent eddies is responsible for breakup, however only large turbulent eddies from high energy dissipation rate contain sufficient energy to affect breakage (Prince and Blanch, 1990). In general, the result on parameter ε indicates that, the overall system behaviour can be in the form of breakage-

dominated or coalescence-dominated. The system is breakage-dominated if higher energy dissipation rate is introduced (i.e., higher flow rate and Reynolds number) and coalescence-dominated if the opposite criterion is met.

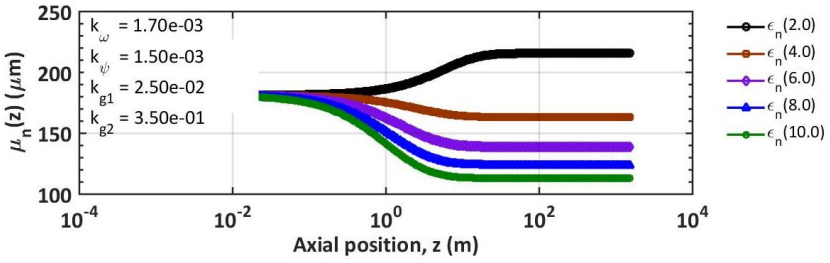

(a)

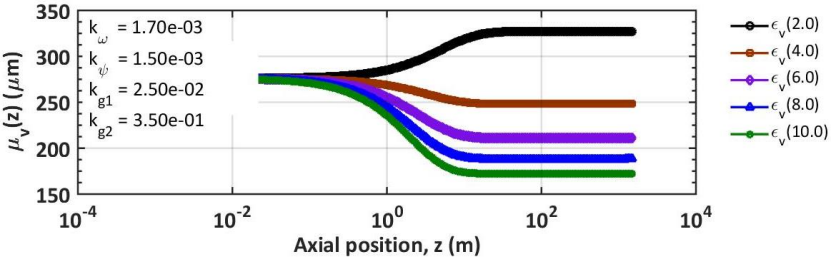

(b)

Figure 4.10 The effect of various energy dissipation rates, ε on the average radii of (a) number density distribution, μ_N and (b) volume density distribution, μ_V. The new fitting parameters used are shown on top left corner of the plot.

Besides that**,** fitting parameters of k_ω and k_{g1} are also important parameters to evaluate because they can significantly affect the overall model behavior, particularly the length of equilibrium, L_{eq}. In this work, the L_{eq} is the length at which the mean radii are consistently unchanged or equilibrated towards the end of the pipeline due to the balance between the breakage and coalescence processes. Hence, to evaluate the effect of fitting parameters k_ω and k_{g1} on the overall system behaviour, the mean radii for number and

volume density distributions are plotted against the axial position, z as depicted in Fig. 4.11(a) and (b). Furthermore, to maintain consistency in the study, the plot is selected at pipe length L = 10,000m and the fitting parameters k_ω and k_{g1} are varied at three different order of magnitudes (i.e., 10^n where, n=-2,-3,-4). From Fig. 4.11, the system is found to equilibrate at faster rate and shorter distance (shift to the left) as k_ω and k_{g1} increase. Conversely, the system is found to take slower time and longer equilibrium length (shift to the right) as k_ω and k_{g1} decrease. The results indicate that the k_ω and k_{g1} play a major role in altering and controlling the equilibrium state of the system. In this respect, as the magnitude of k_ω and k_{g1} increase, the equilibrium rate increases. This is true considering the intensity of the coalescence and breakage rates generated as fitting parameters k_ω and k_{g1} increase due to direct proportionality effect of k_ω and k_{g1} as depicted in Eqn. (3.11) and Eqn. (3.17). In general, the results signify that, k_ω and k_{g_1} have a strong influence the overall system behavior especially on the L_{eq}. Hence, altering or changing these values one can gain control on the relative magnitudes of coalescence and breakage frequencies which result in different length of equilibrium.

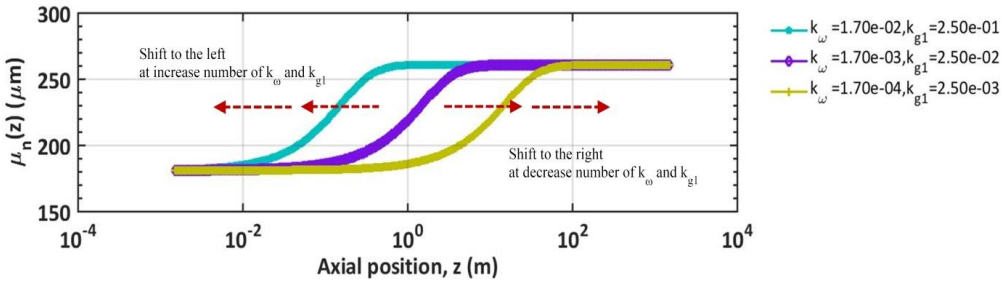

(a)

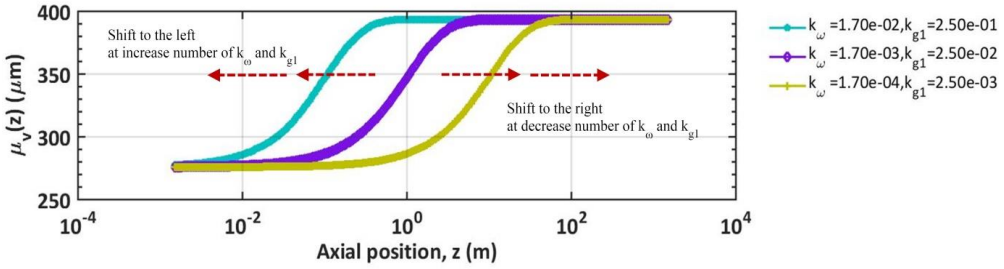

(b)

Figure 4.11 The effect of fitting parameters k_ω and k_{g1} at pipe length, L= 10,000m on the average radii of (a) number density distribution, μ_N and (b) volume density distribution, μ_V.

The last and most important parameter evaluated is the volume fraction of the oil-water system, ϕ. Fig. 4.12 shows the effect of various volume fractions on the mean number radii as a function of axial position, z. The mean radii are found to be consistently growing until they stabilize and level at a constant magnitude approaching the end of the pipeline (at higher z). The results of the mean radii in Fig. 4.12 indicates that, the volume fraction, ϕ plays a major role in affecting the overall system behavior. In this regard, the bigger the volume fraction, more droplets are expected to be present in the pipe and due to considerably high coalescence frequency and efficiency parameters at about k_ω= 1.70e^{-03} and k_ψ= 1.50e^{-03} in the system, hence, the tendency to form larger droplets also increases. At these conditions, the frequencies and chances of the droplets to collide and coalesce respectively are enhanced particularly at high volume fraction. Experimental study by Maaß et al., (2012) on the effect of dispersed phase fraction on drop size distributions supported the argument. They observed that, the increase in dispersed phase fraction causes the mean drop sizes to increase. In a nutshell, the magnitude of average drop radius becomes higher as volume fraction increased at the given fitting parameters. Several authors relate this behavior due to turbulence damping (Cohen 1991: Coulaloglou and Tavlarides, 1977), while, others attribute it to coalescence

process. There are also other researchers believe that this trend is associated with both turbulence dampening and coalescence (Gäbler et al., 2006). This, however, is not the case when the volume fraction is at 0.6 as depicted in Fig. 4.12. The mean number radii, μ_N at $\phi = 0.6$ is observed to drop to a magnitude less than at volume fraction, $\phi = 0.5$ at the equilibrium state towards the end of the pipeline. This is possibly due to the model kernels employed in the system neglect the damping effects $(1 + \phi)$ in turbulent local intensities at high volume fraction as suggested by Coulaloglou and Tavlarides (1977). Hence, at increase amount of dispersed volume fraction (i.e., $\phi > 0.3$) the system did not account the damping effect which results in lower mean radii at high volume fractions in the equilibrium state. However, the mean number radii μ_N are found to be not affected at lower dispersed volume fractions ($\phi \leq 0.3$) with an increasing trend as expected.

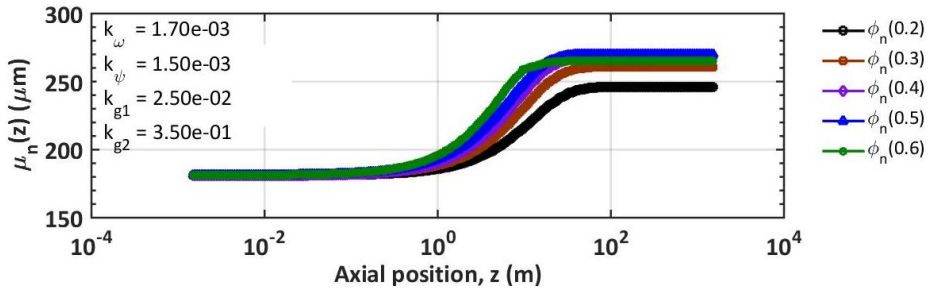

Figure 4.12 The effect of various volume fractions, ϕ on the average radii of number density distribution, μ_N. The fitting parameters used are shown on top left corner of the plot.

Many literatures have reported that an increase in the dispersed phase fraction will result in an increasing drop diameter. Hence, to address the issue of high-volume fraction in the system, the models as depicted in Table 4.6 have been implemented with minor modifications by introducing the factor of $(1 + \phi)$ to account for the damping effect as suggested by Coulaloglou and Tavlarides, (1977). The modified model for the breakage and

coalescence kernels are shown in Table 4.7 and the results are plotted in Fig. 4.13 using the same fitting parameters plotted in Fig. 4.12 for the mean number radii, μ_N.

Table 4.6 Existing model for breakage and coalescence kernels

Process	Existing model
Breakage frequency (Vankova et al., 2007)	$g(r) = k_{g_1} \frac{\varepsilon^{1/3}}{2^{2/3} r^{2/3}} \sqrt{\frac{\rho_c}{\rho_d}} exp\left[-k_{g_2} \frac{\sigma}{\rho_d 2^{5/3} r^{5/3} \varepsilon^{2/3}}\right]$
Collision frequency (Prince and Blanch, 1990)	$\omega_c(r', r'') = 4\sqrt[3]{2}\, k_\omega \varepsilon^{1/3} \left(r' + r''\right)^2 \left(r'^{2/3} + r''^{2/3}\right)^{1/2}$
Coalescence efficiency (Chesters, 1991)	$\psi_E(r', r'') = \exp\left[-k_\psi \frac{\rho_c^{1/2} \varepsilon^{1/3} r_{eq}^{5/6}}{2^{1/6} \sigma^{1/2}}\right]$

Table 4.7 Modified model for breakage and coalescence kernels

Process	Modified model
Breakage frequency	$g(r) = k_{g_1} \frac{\varepsilon^{1/3}}{2^{2/3} r^{2/3} (1+\phi)} \sqrt{\frac{\rho_c}{\rho_d}} exp\left[-k_{g_2} \frac{\sigma (1+\phi)^2}{\rho_d 2^{5/3} r^{5/3} \varepsilon^{2/3}}\right]$
Collision frequency	$\omega_c(r', r'') = \frac{4\sqrt[3]{2}\, k_\omega \varepsilon^{1/3}}{1+\phi} \left(r' + r''\right)^2 \left(r'^{2/3} + r''^{2/3}\right)^{1/2}$
Coalescence efficiency	$\psi_E(r', r'') = \exp\left[-k_\psi \frac{\rho_c^{1/2} \varepsilon^{1/3} r_{eq}^{5/6}}{2^{1/6} \sigma^{1/2} (1+\phi)^3}\right]$

Based on the coalescence and breakage models published in the literature (see Table 2.1 – 2.4), majority are found to neglect the damping factor $(1 + \phi)$ on the local turbulent intensities at high dispersed phase fraction as depicted in Table 4.6. Hence, this present work

offers an insight of the droplet sizes by accounting the dampening of the turbulence due to disperse phase fraction in the modified breakage and coalescence models as depicted in Table 4.7. The results in Fig. 4.13 suggests that, as the volume fraction increases the mean radii increase in magnitude, particularly at $\phi = 0.6$. This indicates that, higher volume fraction enhances the probability of the formation of larger droplets and consequently increases the mean radii. Recent experimental investigation by Schümann (2016) has shown that, the mean and the maximum droplet sizes increase when the dispersed volume fraction is increased. Earlier investigation by Ioannou, (2006) also found that higher fractions of dispersed phase lead to coalescence dominating and eventually increase the average droplet size. In general, the results have shown that, modelling drop size distributions at high volume fraction is in a good agreement with experimental work reported in literature. Thus, for drop size analysis in liquid-liquid dispersions, one should consider the damping factor $(1 + \phi)$ so that the turbulence damping at high volume fraction is appropriately accounted. From another point of view, the overall results of parametric effects suggest that, one can have the understanding and control of the breakage and coalescence processes when conducting the experiment on drop size distribution in turbulent pipe flow.

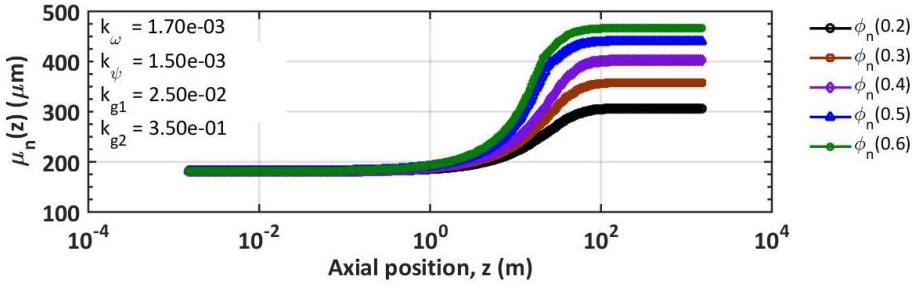

Figure 4.13 The effect of various volume fractions, ϕ on the average radii of number density distribution, μ_N with damping effect $(1 + \phi)$ proposed by Coulaloglou and Tavlarides, (1977) for the new fitting parameters shown on top left corner.

Additionally, simple regression analysis of drop size distribution at the final location in the pipe is also evaluated to understand the overall model behavior. To demonstrate the regression behavior, the sum of squares (SSQ) is evaluated between the simulation results and the experimental results at the final location in the pipe. In general, the results from SSQ enable important information in finding the best fit for the dynamic evolution of the drop size density distribution in liquid-liquid emulsions in turbulent pipe flow. In this regression study, the behavior of SSQ is plotted in terms of k_ω and k_{g_1} for three different values of fitting parameters k_ψ and k_{g_2} as depicted in Fig. 4.14(a), (b), and (c). The fitting parameters k_ψ and k_{g_2} are set at decreasing in magnitude as shown in Fig. 4.14(a), (b), and (c), respectively. The behavior of SSQ at k_ψ =1.50e^{-02} and k_{g_2} = 3.50e^{0} as portrayed in Fig. 4.19(a) indicates that the local minima are lies in the region approaching the 10^{-4} of k_{g_1} and 10^{0} for k_ω. As shown in this figure, the value for fitting parameters k_ω and k_{g_1} are set at lower, k_ω (i.e., $\leq 10^{-5}$) and higher, k_{g_1} (i.e., $\geq 10^{1}$). In this respect, for these set of fitting parameters (k_ψ and k_{g_2}), one should avoid placing the higher and smaller values for the fitting parameters of, k_{g_1} and k_ω, respectively, in order to find the best fit or local minima. On the other hand, Fig. 4.14(b) provides significant information on finding the best fit. From these results of regression behavior, one can have an insight on which order of magnitude and values of fitting parameters in finding the best fit for the dynamic evolution of drop size distribution in turbulently flowing liquid-liquid emulsions. In general, to find the best fit or local minima of the system, one must consider the appropriate magnitude of k_ψ and k_{g_2} (as depicted in Fig. 4.14(b)). This is because, the interplay between the four fitting parameters is crucial as they are found to be significantly affecting the overall regression behavior.

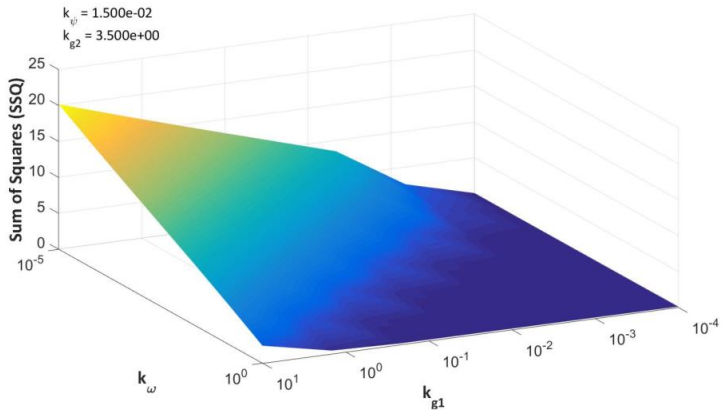
k_ψ = 1.500e-02
k_g2 = 3.500e+00
Sum of Squares (SSQ)
25
20
15
10
5
0
10^-5
10^0
10^1
k_ω
10^0
10^-1
10^-2
10^-3
10^-4
k_g1

(a)

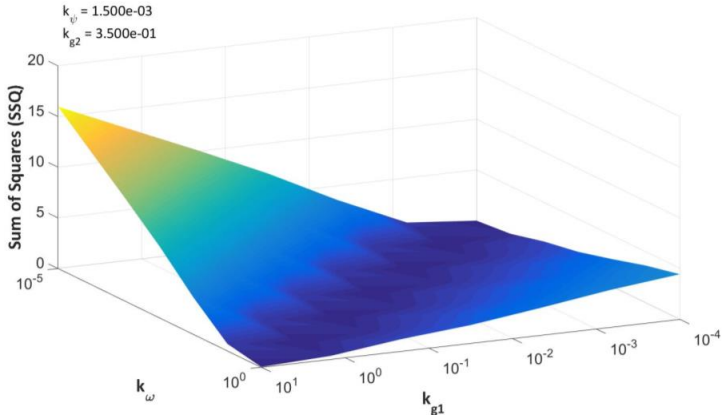
k_ψ = 1.500e-03
k_g2 = 3.500e-01
Sum of Squares (SSQ)
20
15
10
5
0
10^-5
10^0
10^1
k_ω
10^0
10^-1
10^-2
10^-3
10^-4
k_g1

(b)

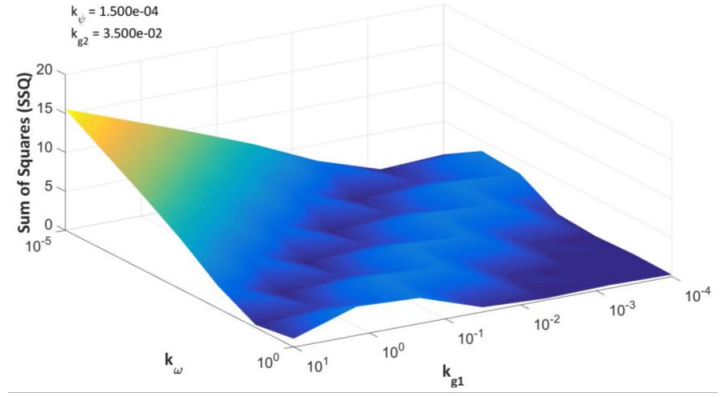
k_ψ = 1.500e-04
k_g2 = 3.500e-02
Sum of Squares (SSQ)
20
15
10
5
0
10^-5
10^0
10^1
k_ω
10^0
10^-1
10^-2
10^-3
10^-4
k_g1

(c)

Figure 4.14 The behavior of sum of squares (SSQ) as a function of k_ω and k_{g_1} at given fitting parameters: (a) k_ψ= 1.50e^{-02} and k_{g_2}= 3.50e^{-00}, (b) k_ψ= 1.50e^{-03} and k_{g_2}= 3.50e^{-01}, and (c) k_ψ= 1.50e^{-04} and k_{g_2}= 3.50e^{-02}.

4.3 Chapter summary

This chapter discussed the drops evolution of oil-water emulsion in a long-distance turbulent pipe flow. One of the main contributions in this present work is the proposed solutions for the PBE. In this present work, the PBE is solved in the form of volume density distribution, f_v instead of the typical number density distribution, f_n. The study is also crucial for case-specific system in a liquid-liquid condition with various fluids properties and flow conditions. In this regard, the study on parametric effects provides the understanding on the interplay between various parametric effects that contribute to the overall behavior of the drop size distributions. Besides that, the model has proved to be reliable and robust from the arbitrary set of results depicted. Two manuscripts are prepared (i.e.., Part I and Part II) for this discussion (Chapter 4) as attached in Appendix B and C of this thesis. Next section will discuss the regression of experimental pipe flow between simulation and experimental data.

CHAPTER 5

5 RESULTS AND DISCUSSION (PART II)

5.1 Part II: Regression of the experimental pipe flow data: comparison between simulation and experimental data

In this chapter, the comparisons between the simulation and experimental data as well as the best fitting parameters are analyzed and discussed. For the second part of the discussions (Part II), the following physical properties of the oil-water system are used in the simulation as depicted in Table 5.1. The physical properties shown in Table 5.1 are divided into three different data sets known as ge12275a, ge12279a, and ge12284a. The primary difference between the three experimental data sets is the average flow velocity, U. In this respect, ge12275a represents the lowest average flow velocity, U at 1.70 m/s, followed by ge12279a and ge12284a with 2.0 m/s and 2.50 m/s, respectively. All the parameters in Table 5.1 are then used as inputs for the model simulations.

In this regression study, several models are selected for the breakage and coalescence kernels in order to evaluate their effect on the dynamic evolution of the drop size density distribution in pipes. The details of the models are summarized in Table 5.2, Table 5.3, and Table 5.4. It is important to note that, the breakage kernels are selected based on the mechanism of turbulent fluctuations. While, the coalescence kernels are selected from the film drainage model and energy model as a result from turbulent-induced collisions. In Table 5.2, the selected models are categorized into three different cases known as case I, case II, and case III. Each case comprised of different underlying mechanisms.

Table 5.1 Overview of the physical parameters from the experimental oil-water pipe flow

Parameter	Ge12275a	Ge12279a	Ge12284a	Descriptions
Ø	0.30	0.30	0.30	Volume fraction
U	1.70 [m/s]	2.00 [m/s]	2.50 [m/s]	Average flow velocity
L	30 [m]	30 [m]	30 [m]	Length of the pipe
R_{max}	1000 [μm]	1000 [μm]	1000 [μm]	Upper bound of the radius domain
D	0.069 [m]	0.069 [m]	0.069 [m]	Diameter of the pipe
ρ_d	865 [kg/m^3]	865 [kg/m^3]	865 [kg/m^3]	Density of the dispersed phase
μ_d	177 [mPas]	169 [mPas]	152 [mPas]	Viscosity of the dispersed phase
ρ_c	1021 [kg/m^3]	1021 [kg/m^3]	1021 [kg/m^3]	Density of the continuous phase
μ_c	1.0 [mPas]	1.0 [mPas]	1.0 [mPas]	Viscosity of the continuous phase
σ	26.0 [mN/m]	26.0 [mN/m]	26.0 [mN/m]	Interfacial tension

Table 5.2 Comparison between simulation cases for breakage and coalescence kernels

Case	Breakage kernels	Coalescence kernels
I	Coulaloglou and Tavlarides, (1977) + Hsia and Tavlarides, (1980)	Coulaloglou and Tavlarides, (1977) + Coulaloglou and Tavlarides, (1977)
II	Vankova et al., (2007) + Coulaloglou and Tavlarides, (1977)	Prince and Blanch (1990) + Chesters (1991)
III	Vankova et al., (2007) + Coulaloglou and Tavlarides, (1977)	Prince and Blanch (1990) + Simon (2004)

Table 5.3 Summary of breakage models for every case

Case	Breakage kernels
I	$g(r) = k_{g_1}\frac{\varepsilon^{1/3}}{r^{2/3}(1+\phi)}\exp\left[-k_{g_2}\frac{\sigma(1+\phi)^2}{\rho_d\varepsilon^{2/3}r^{5/3}}\right] +$ $\beta(r,r') = \frac{45}{2\sqrt[3]{2}}\frac{r^2}{r'^3}\left(\frac{r^3}{r'^3}\right)^2\left[1-\left(\frac{r^3}{r'^3}\right)^2\right]$
II	$g(r) = k_{g_1}\frac{\varepsilon^{1/3}}{2^{2/3}r^{2/3}}\sqrt{\frac{\rho_d}{\rho_c}}exp\left[-k_{g_2}\frac{\sigma}{\rho_d 2^{5/3}\, r^{5/3}\varepsilon^{2/3}}\right] +$ $\beta(r,r') = \frac{2.4}{r'^3}\exp\left[-4.5\,\frac{(2r^3-r'^3)^2}{r'^6}\right]\times 3r^2$
III	$g(r) = k_{g_1}\frac{\varepsilon^{1/3}}{2^{2/3}r^{2/3}}\sqrt{\frac{\rho_d}{\rho_c}}exp\left[-k_{g_2}\frac{\sigma}{\rho_d 2^{5/3}\, r^{5/3}\varepsilon^{2/3}}\right] +$ $\beta(r,r') = \frac{2.4}{r'^3}\exp\left[-4.5\,\frac{(2r^3-r'^3)^2}{r'^6}\right]\times 3r^2$

Table 5.4 Summary of coalescence models for every case

Case	Coalescence kernels
I	$\omega_c(r',r'') = k_\omega\frac{\varepsilon^{1/3}}{1+\phi}(r'+r'')^2\left[r'^{2/3}+r''^{\,2/3}\right]^{1/2} +$ $\psi_e(r',r'') = \exp\left[-\frac{1}{k_\psi}\frac{\mu_c\rho_c\varepsilon}{\sigma^2(1+\phi)^3}\left(\frac{r'r''}{r'+r''}\right)^4\right]$
II	$\omega_c(r',r'') = 4\sqrt[3]{2}\,k_\omega\varepsilon^{1/3}(r'+r'')^2(r'^{2/3}+r''^{2/3})^{1/2} +$ $\psi_e(r',r'') = \exp\left[-k_\psi\frac{\rho_c^{1/2}\varepsilon^{1/3}r_{eq}^{5/6}}{2^{1/6}\sigma^{1/2}}\right]$
III	$\omega_c(r',r'') = 4\sqrt[3]{2}\,k_\omega\varepsilon^{1/3}(r'+r'')^2(r'^{2/3}+r''^{2/3})^{1/2} +$

$$\psi_e(r', r'') = \exp\left[-\frac{4k_\psi \sigma(r'^2 + r''^2)}{\rho_d \varepsilon^{2/3} 2^{11/3}(r'^{11/3} + r''^{11/3})}\right]$$

There are various mechanisms discussed to describe the breakage process (refer to Chapter 2, section 2.3.1 of this thesis) and the coalescence process (refer to Chapter 2, section 2.4.1 of this thesis) as explained in the review articles by Liao and Lucas (2009), Liao and Lucas (2010), Sajjadi et al., (2013), Solsvik et al., (2013), and Abidin et al., (2015). However, in this study, mechanism of turbulent fluctuations for breakage process is selected due to its relevance applicability to the present study (i.e., liquid-liquid flow) as well as its extensive used in the literature. Apart from limited discussions in literature, the other mechanisms such as breakup due to viscous shear force, breakup due to shearing-off process, and breakup due to interfacial instabilities are mainly developed based on gas-liquid system (Liao and Lucas, 2009).

On the other hand, for the coalescence process, the mechanism of turbulent-induced collisions is selected. Wherein, other mechanisms such as droplets capture in an eddy, velocity gradient-induced collisions, buoyancy-induced collisions, and wake interactions-induced collision are primarily relevance only for gas-liquid system where the different in properties of the phases are significant in affecting the collisions between bubbles/droplets. Although there is an exception on drop collision mechanism of droplets capture in an eddy. However, the mechanism is not able to predict the coalescence kinetics accurately as reported by Sajjadi et al., (2013) and limited studies are found in the literature. Therefore, turbulent fluctuations for breakage process and turbulent-induced collisions for coalescence process are considered while, other mechanisms are not evaluated in the current work. The overview of mechanisms for the simulation cases in each selected breakage and coalescence kernels are illustrated in Table 5.5 as follows.

Table 5.5 Comparison between simulation cases based on underlying mechanisms for each breakage and coalescence kernels

Case	Mechanisms for breakage kernels	Mechanisms for coalescence kernels
I	Turbulent fluctuations + statistical model (beta distribution function)	Turbulent-induced collisions + film drainage model (deformable particles with immobile interfaces)
II	Turbulent fluctuations + statistical model (normal distribution function)	Turbulent-induced collisions + film drainage model (deformable particles with fully mobile interfaces)
III	Turbulent fluctuations + statistical model (normal distribution function)	Turbulent-induced collisions + energy model

In Table 5.5, the coalescence efficiency function in case I and case II are selected based on film drainage model with specific characteristics of deformable droplets with immobile interfaces and deformable droplets with mobile interfaces, respectively. In film drainage, these characteristics are essential because they describe the quality of the coalescence efficiency during the collision between two droplets, particularly in liquid-liquid system. For both cases the deformable droplets refer to the rigidity of the particle surfaces, while, the mobility denotes the motion of the colliding droplet interfaces during the process of film drainage. In case I, the coalescence efficiency by film drainage is characterized by a viscous thinning. Hence, this film drainage model is applicable for very viscous dispersed phase or system with very specific surfactant soluble concentration (Liao and Lucas, 2010). According to Lee and Hodgson (1968), the immobile interfaces refers to interfaces when the surfaces shear stresses due to flow within the film are resisted by the interfacial tension gradient set up because of expansion of the surface in the central regions of the film. In this

regard, the droplet can support an infinite high shear stress (Æther, 2002). This is due to the presence of the surfactant or impurities at the interfaces and in this condition, the film will drain very slowly (Æther, 2002). On the other hand, in case II, the coalescence efficiency from the drainage process is the opposite criteria of case I. This model of deformable droplets with fully mobile interfaces is suitable for a case of liquid-liquid system of the dispersed phase (Chesters, 1991). In this respect, the drainage is no longer controlled by the viscous stress as in immobile interfaces but instead by the resistance occurred in the film due to deformation and acceleration (Chesters, 1991; Liao and Lucas, 2010).

5.2 Regression results and discussion (model validation with experimental data)

It is of interest in this section to compare the solution of the population balance equation using various breakage and coalescence models against the three different experimental data sets at the final location (pipeline). We used the fitting parameters to determine the most robust and applicable coalescence or breakage models. Table 5.6 shows the best estimation of the fitting parameters (i.e., $k_{\omega}, k_{\psi}, k_{g_1}, k_{g_2}$) for the regression of experimental pipe flow data in terms of volume density distribution, f_v at the final location.

Table 5.6 Numerical value of best fitting parameters and confidence intervals

Data set	Case	$k_\omega \pm$ confidence interval	$k_\psi \pm$ confidence interval	$k_{g_1} \pm$ confidence interval	$k_{g_2} \pm$ confidence interval
Ge12275a	I	$2.200 \times 10^{-2} \pm 5.19 \times 10^{-5}$	$4.550 \times 10^{-11} \pm 7.39 \times 10^{-14}$	$3.879 \times 10^{-1} \pm 6.27 \times 10^{-4}$	$1.010 \times 10^{-1} \pm 3.80 \times 10^{-4}$
	II	$1.090 \times 10^{-2} \pm 2.74 \times 10^{-5}$	$8.499 \times 10^{-3} \pm 2.23 \times 10^{-5}$	$1.870 \times 10^{-1} \pm 4.70 \times 10^{-4}$	$2.380 \times 10^{-1} \pm 6.25 \times 10^{-4}$
	III	$2.799 \times 10^{-2} \pm 1.25 \times 10^{-5}$	$1.100 \times 10^{-4} \pm 4.89 \times 10^{-8}$	$4.750 \times 10^{-1} \pm 7.93 \times 10^{-4}$	$2.350 \times 10^{-1} \pm 4.89 \times 10^{-4}$
Ge12279a	I	$2.550 \times 10^{-2} \pm 1.30 \times 10^{-5}$	$6.900 \times 10^{-11} \pm 2.31 \times 10^{-13}$	$4.050 \times 10^{-1} \pm 2.69 \times 10^{-4}$	$1.450 \times 10^{-1} \pm 7.78 \times 10^{-4}$
	II	$1.560 \times 10^{-2} \pm 1.26 \times 10^{-5}$	$5.500 \times 10^{-3} \pm 2.01 \times 10^{-7}$	$2.460 \times 10^{-1} \pm 1.90 \times 10^{-5}$	$3.350 \times 10^{-1} \pm 1.65 \times 10^{-5}$
	III	$1.950 \times 10^{-2} \pm 1.46 \times 10^{-6}$	$1.100 \times 10^{-4} \pm 6.02 \times 10^{-7}$	$3.000 \times 10^{-1} \pm 2.71 \times 10^{-4}$	$3.250 \times 10^{-1} \pm 2.16 \times 10^{-5}$
Ge12284a	I	$2.500 \times 10^{-2} \pm 2.15 \times 10^{-5}$	$9.850 \times 10^{-11} \pm 1.07 \times 10^{-13}$	$3.249 \times 10^{-1} \pm 3.24 \times 10^{-4}$	$2.150 \times 10^{-1} \pm 1.95 \times 10^{-4}$
	II	$1.059 \times 10^{-2} \pm 2.60 \times 10^{-7}$	$5.500 \times 10^{-3} \pm 1.40 \times 10^{-7}$	$1.820 \times 10^{-1} \pm 1.21 \times 10^{-6}$	$6.149 \times 10^{-1} \pm 3.72 \times 10^{-6}$
	III	$3.200 \times 10^{-2} \pm 5.94 \times 10^{-6}$	$1.100 \times 10^{-4} \pm 1.73 \times 10^{-7}$	$5.320 \times 10^{-1} \pm 5.79 \times 10^{-4}$	$5.850 \times 10^{-1} \pm 1.46 \times 10^{-4}$

It is worth noting that, each two of the fitting parameters are associated with coalescence (k_ω, k_ψ) and breakage (k_{g_1}, k_{g_2}) mechanisms, respectively. These four fitting parameters are crucial as they control the dynamics of the overall system behaviour (as discussed earlier in parametric effect in Part I of Chapter 4). The confidence intervals are calculated based on the difference between the simulation and experimental data at the final location of the pipes. The results tabulated in Table 5.6 also highlight the confidence intervals that consist of the probability or the range limit of the best fitted parameters. From all of the cases studied, the confidence interval is found to be at least one order of magnitude different than the actual parameter. This suggests that, the results for the regression of breakage and coalescence parameters at lower order of magnitude of the confidence interval are in good agreement with the experimental data as shown in Fig. 5.1 until Fig. 5.3. The results of regression clearly indicate that the model simulations are perfectly fit with the shape and peak of the volume density distribution at final location in the pipeline for each of the best fitting parameters depicted in Table 5.6. The comparison among all the cases and data sets suggests that the fit of the drop volume distribution at the final location is considered satisfactory in terms of the distribution properties (i.e., shape and peak location). This demonstrates that all the models evaluated match the experimental data.

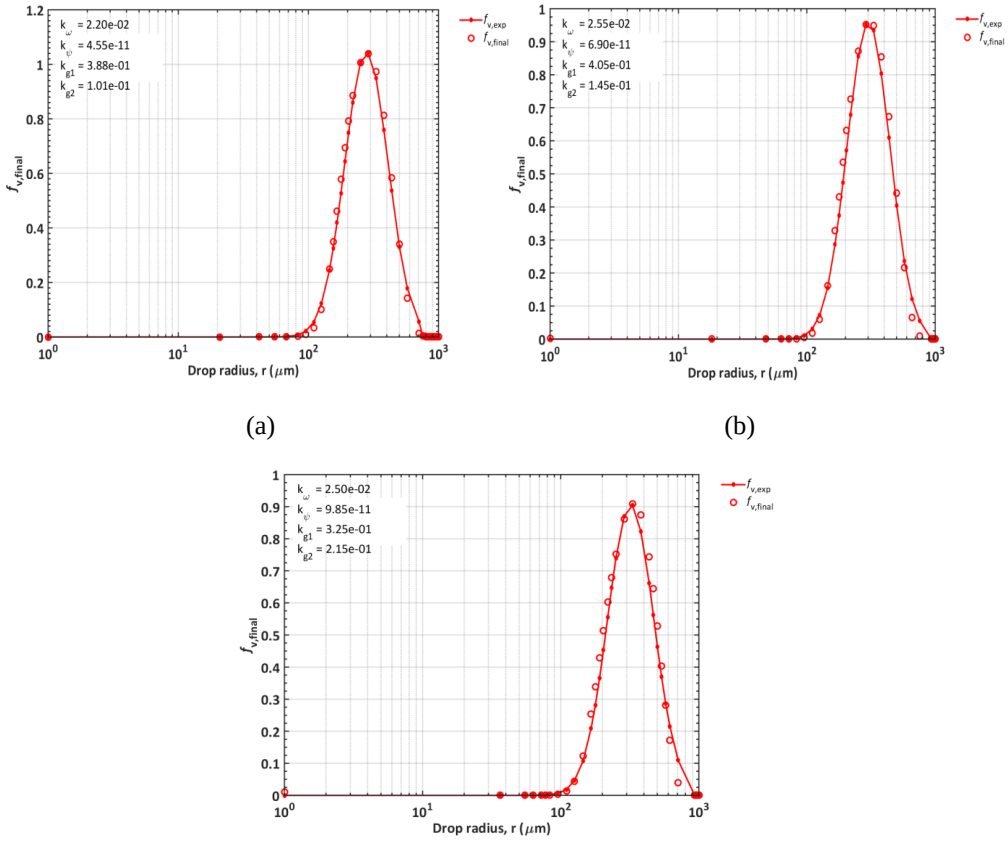

Figure 5.1 Comparison of the scaled experimental volume density distribution and the model prediction using the best fit parameters for case I and data set of: (a) ge12275a, (b) ge12279a, and (c) ge12284a.

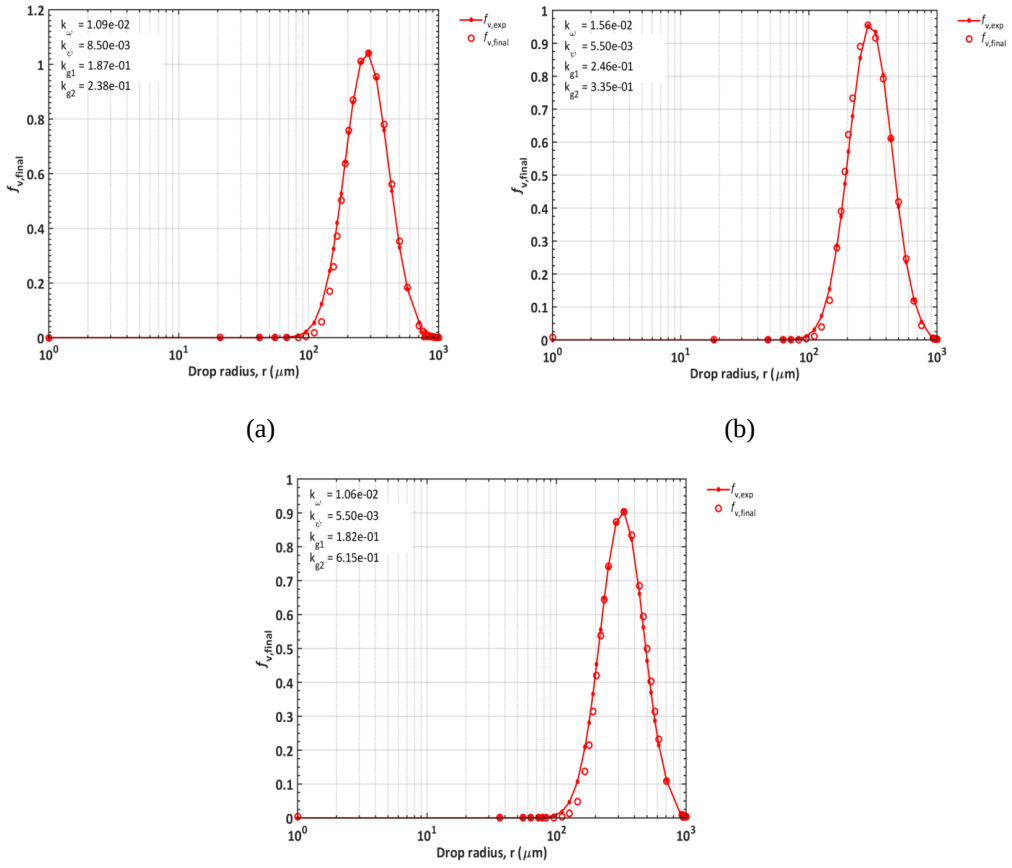

Figure 5.2 Comparison of the scaled experimental volume density distribution and the model prediction using the best fit parameters for case II and data set of: (a) ge12275a, (b) ge12279a, and (c) ge12284a.

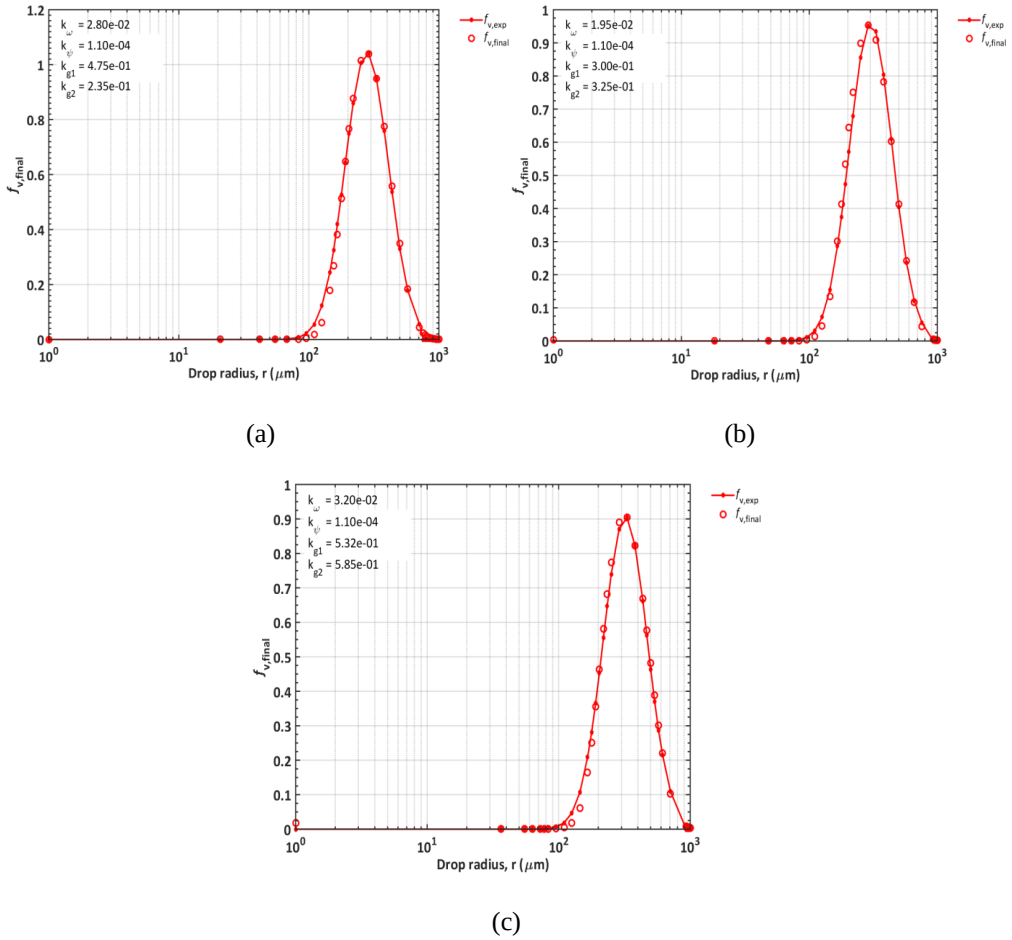

Figure 5.3 Comparison of the scaled experimental volume density distribution and the model prediction using the best fit parameters for case III and data set of: (a) ge12275a, (b) ge12279a, and (c) ge12284a.

In this study, the fits are determined by using nonlinear regression model and while doing so, the effect toward the overall model behavior have to be considered. For every fitting parameter tested, the results are plotted and analyzed until it is considered to be perfectly fits with the final (location) experimental data in terms of the shape and peak of the volume density distribution. In addition to this approach, sum of squares (SSQ) are also calculated to verify the best regression of the volume density distribution at final location.

Principally, SSQ method is to find the local minima (deviation in data points) between the simulation results and the experimental data. As depicted in Fig. 5.4 until Fig. 5.6, at the given values of k_ψ and k_{g_2}, one can estimate the range of k_ω and k_{g_1} at the lowest SSQ (local minima) to find the best fits of the system.

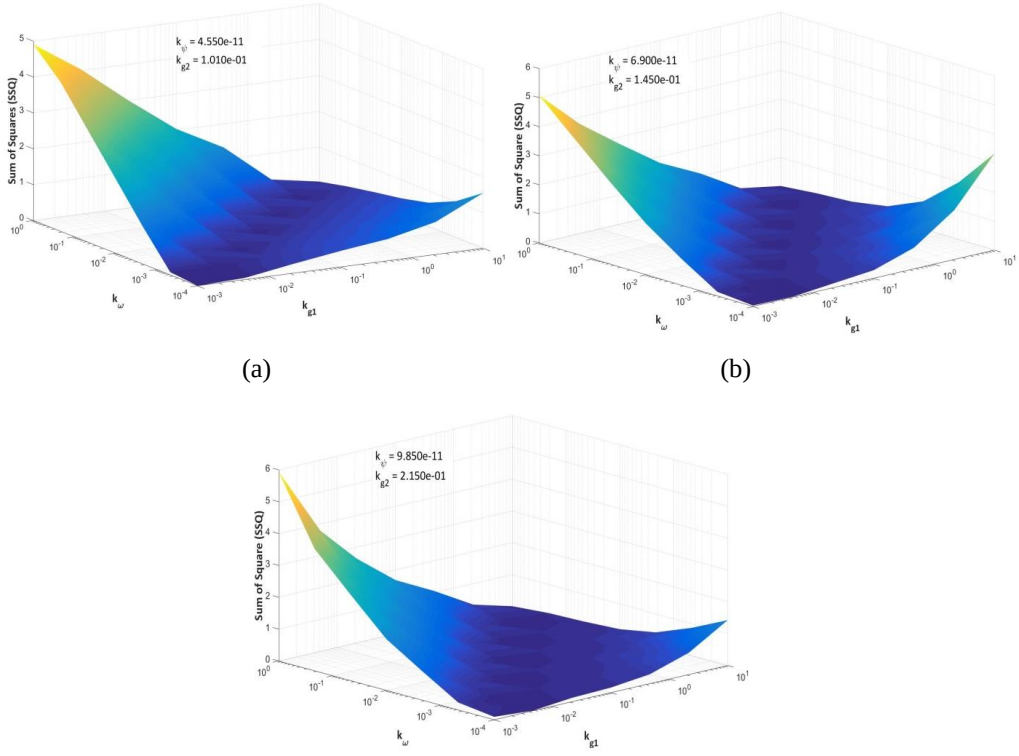

Figure 5.4 Overview of sum of squares (SSQ) as a function of k_{g_1} and k_ω for case I and data set of: (a) ge12275a at $k_\psi = 4.55 \times 10^{-11}$ and $k_{g_2} = 1.01 \times 10^{-1}$, (b) ge12279a at $k_\psi = 6.90 \times 10^{-11}$ and $k_{g_2} = 1.45 \times 10^{-1}$, and (c) ge12284a at $k_\psi = 9.85 \times 10^{-11}$ and $k_{g_2} = 2.15 \times 10^{-1}$.

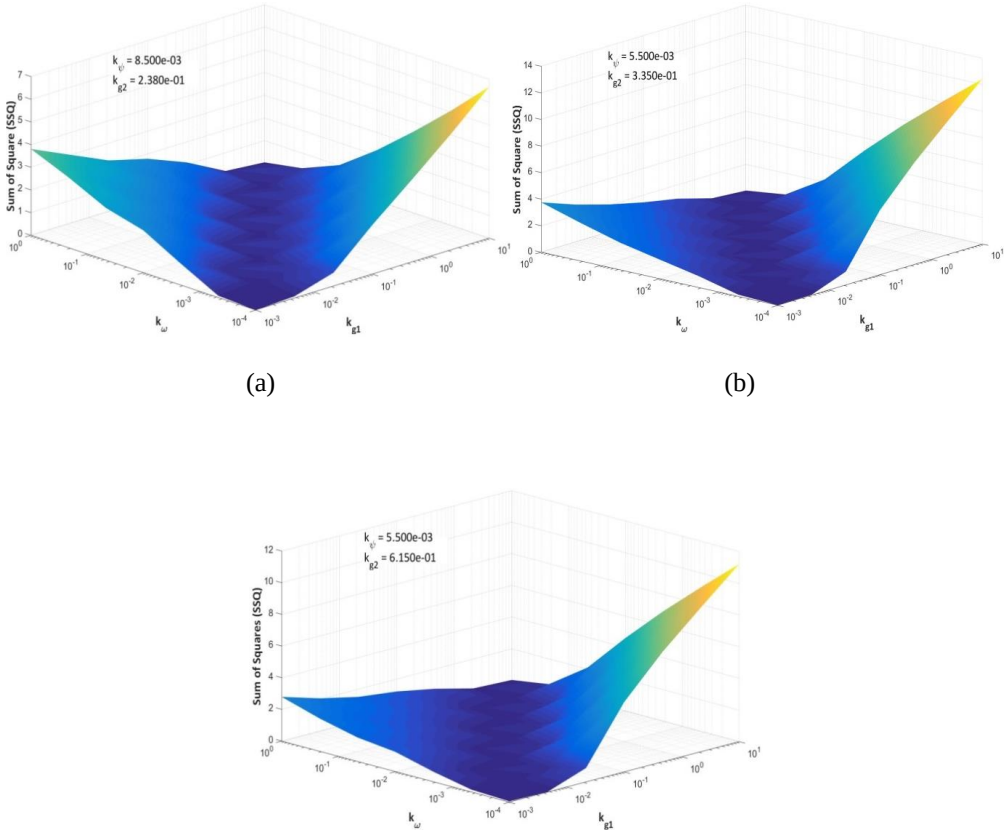

Figure 5.5 Overview of sum of squares (SSQ) as a function of k_{g_1} and k_ω for case II and data set of: (a) ge12275a at $k_\psi = 8.50 \times 10^{-3}$ and $k_{g_2} = 2.38 \times 10^{-1}$, (b) ge12279a at $k_\psi = 5.50 \times 10^{-3}$ and $k_{g_2} = 3.35 \times 10^{-1}$, and (c) ge12284a at $k_\psi = 5.50 \times 10^{-3}$ and $k_{g_2} = 6.15 \times 10^{-1}$.

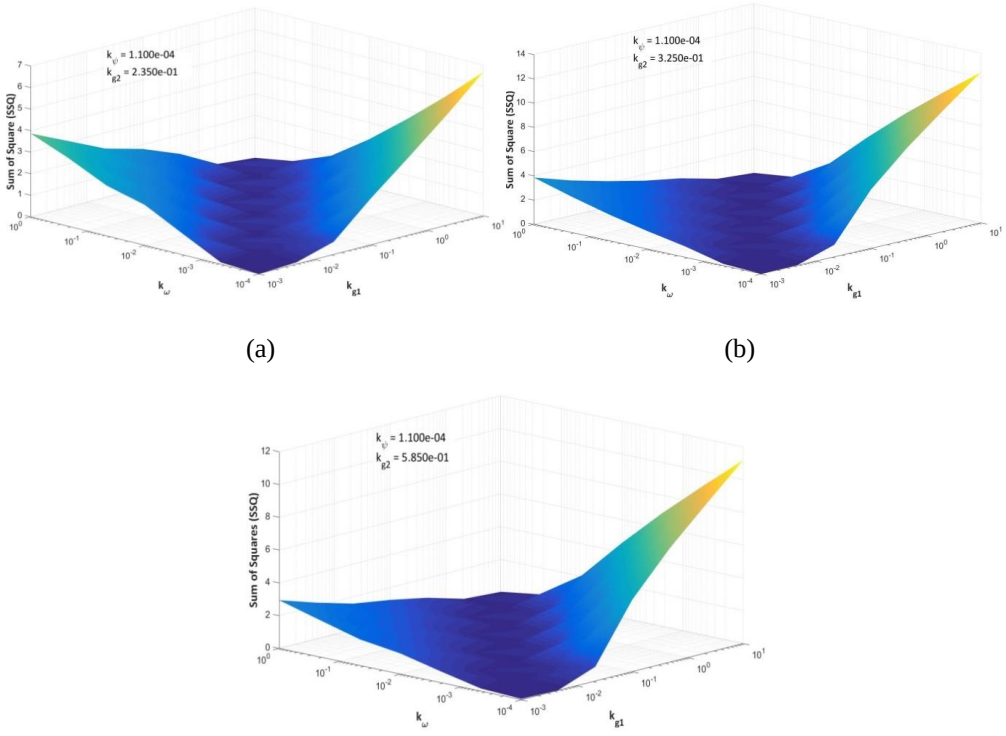

Figure 5.6 Overview of sum of squares (SSQ) as a function of k_{g_1} and k_ω for case III and data set of: (a) ge12275a at $k_\psi = 1.10 \times 10^{-4}$ and $k_{g_2} = 2.35 \times 10^{-1}$, (b) ge12279a at $k_\psi = 1.10 \times 10^{-4}$ and $k_{g_2} = 3.25 \times 10^{-1}$, and (c) ge12284a at $k_\psi = 1.10 \times 10^{-4}$ and $k_{g_2} = 5.85 \times 10^{-1}$.

The results of SSQ are tabulated in Table 5.7 along with the best fitting parameters for all the cases and data sets studied. The results demonstrate that the calculated values of SSQ from the function being fitted are in the range of $\approx 10^{-3} - 10^{-4}$, which indicates that the fits are in good agreement with the experimental data as demonstrated in Fig. 5.1 until Fig. 5.3. From Table 5.7, the best fitting parameter for collision frequency k_ω of this system is found to be in the range between 1.00×10^{-2} to 3.50×10^{-2} for all the cases and data sets.

Table 5.7 Numerical value of the best fitting parameters for all the cases and data sets

Data set	Case	k_ω	k_ψ	k_{g_1}	k_{g_2}	$\frac{k_{g_1}}{k_\omega}$	SSQ
	I	2.20×10^{-2}	4.55×10^{-11}	3.88×10^{-1}	1.01×10^{-1}	17.6	5.92×10^{-4}
Ge12275a	II	1.09×10^{-2}	8.50×10^{-3}	1.87×10^{-1}	2.38×10^{-1}	17.1	6.32×10^{-4}
	III	2.80×10^{-2}	1.10×10^{-4}	4.75×10^{-1}	2.35×10^{-1}	16.9	5.12×10^{-4}
	I	2.55×10^{-2}	6.90×10^{-11}	4.05×10^{-1}	1.45×10^{-1}	15.9	8.50×10^{-4}
Ge12279a	II	1.56×10^{-2}	5.50×10^{-3}	2.46×10^{-1}	3.35×10^{-1}	15.7	3.57×10^{-4}
	III	1.95×10^{-2}	1.10×10^{-4}	3.00×10^{-1}	3.25×10^{-1}	15.3	6.06×10^{-4}
	I	2.50×10^{-2}	9.85×10^{-11}	3.25×10^{-1}	2.15×10^{-1}	13.0	1.18×10^{-3}
Ge12284a	II	1.06×10^{-2}	5.50×10^{-3}	1.82×10^{-1}	6.15×10^{-1}	17.1	6.22×10^{-4}
	III	3.20×10^{-2}	1.10×10^{-4}	5.32×10^{-1}	5.85×10^{-1}	16.6	3.04×10^{-4}

The fitting parameter for coalescence efficiency k_ψ is expected to change for different cases, however, in case I it is observed to be much smaller compared to the cases II and III. This is owing to the fact that the model developed by Coulaloglou and Tavlarides, (1977) assumed the initial thickness of the drops and the film thickness at which film rupture occurs to be constant and lumped into parameter, k_ψ. Therefore, the fitting parameter k_ψ carries a unit of m^2 and can take a very low magnitude (i.e., $\approx 10^{-10} - 10^{-20}$). It is important to note that, in this present work, the equation by Coulaloglou and Tavlarides, (1977), k_ψ is treated as a denominator instead of numerator in the original model which we found to be more practical and sensible in this system. The fitting parameter k_ψ for case I is found to be in the range of 4.00×10^{-11} to 10.00×10^{-11}, while case II lies between 5.00×10^{-3} to 9.00×10^{-3} and case III, the parameter remains constant at 1.01×10^{-4}. In other words, the higher the value of k_ψ, the slower the coalescence rate become (the plot in Fig. 5.1 and Fig. 5.3 will shift backward). This is due to the fact that, k_ψ poses a direct proportionality

influence against the coalescence efficiency model in the exponential term (k_ψ as numerator) as shown in Table 5.4 for all the cases except case I. Consequently, higher magnitude of k_ψ will under-predict the final experimental drop volume density distribution aside from case I, where k_ψ is the denominator (imposes indirect proportionality to the coalescence efficiency) in the exponential term of coalescence efficiency model (refer to Table 5.4).

The result for breakage parameters, k_{g_1} and k_{g_2} are observed to be in the range of $1.00 \times 10^{-1} - 5.50 \times 10^{-1}$ and $1.00 \times 10^{-1} - 6.50 \times 10^{-1}$, respectively. It is worth noting that the constants between k_{g_1} and k_ω play an important role in finding the best fitting parameters. This is true by considering the results of sum of squares (SSQ) analysis as depicted in Fig. 5.4 until Fig. 5.6. The fitting parameters of k_{g_1} and k_ω are observed to have a local minima at every order of magnitude (i.e., 10^n where n = 1, 2, 3) for every set of best fitting parameters in k_ψ and k_{g_2}. To put into another perspective, the ratio of k_{g_1}/k_ω is calculated as depicted in Table 5.7. The ratio may provide an insight on the difference in the degree of magnitude between k_{g_1} and k_ω for every cases and data sets in order to achieve the best fit between the simulation and experimental data of the system. Nevertheless, in this study, we are not determining the absolute value of k_{g_1}/k_ω but only the ratio between both parameters. This due to the different complexity and system application as well as variation in terms of the model employed.

Apart from that, the evolution of number density distribution, f_n and volume density distribution, f_v are determined from the best fitting parameters estimated in Table 5.7 and plotted against droplet of radius, r for nine different locations of the pipe length for case I, II, and III as illustrated in Fig. 5.7, 5.8 and 5.9. The plots provide an overview on the dynamic evolution of drop density distribution in terms of number and volume density distributions (f_n and f_v) throughout 30m pipe length for all the three different cases (case I, II, and III) and data sets (ge12275a, ge12279a, and ge12284a). From the dynamic evolution of number

density distributions shown from Fig. 5.7 until Fig. 5.9 (upper part), there is a large quantity of droplets (high magnitude) present at the beginning (z = 0) and the quantity reduces as it reached the end of the pipeline (z = 30 m). This can be clearly observed in all of the cases, wherein at increasing number of z, the curve begins to descend until it reaches the end of the axial position, z = 30m. Under these conditions, coalescence balances breakage as z increases and eventually the distribution reaches equilibrium. This occurred for all the cases and data sets. A decreasing magnitude of f_n indicates that the drop size distribution is lower and lesser at equilibrium compared to the initial condition. On the other hand, the second plot (bottom part) of Fig. 5.7, 5.8, and 5.9 demonstrate that the droplets dynamic evolution in terms of volume density distribution, f_v across nine different pipe lengths are behaving in similar trend to the f_n. The plots illustrate that, f_v is higher at the beginning (large volume of droplets present at the initial condition) and decreases towards the end (fewer drops volume present at the final condition) of the pipeline at z = 30m as they reaching an equilibrium. for all the cases simulated as shown in Fig. 5.7(c), 5.8(c), and 5.9(c). This indicates that breakage is weak at the beginning of the pipeline because smaller droplet is harder to break than larger droplet.

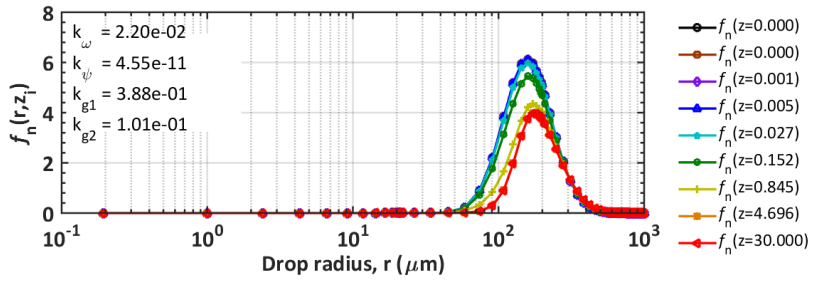

Number density distribution

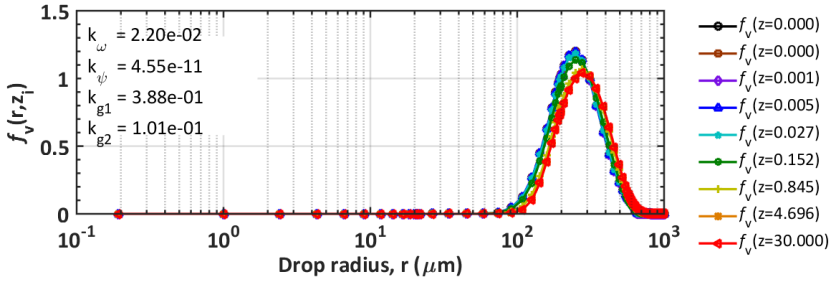

Volume density distribution

(a)

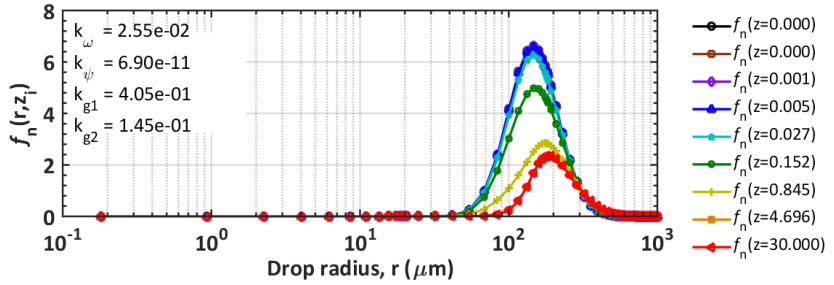

Number density distribution

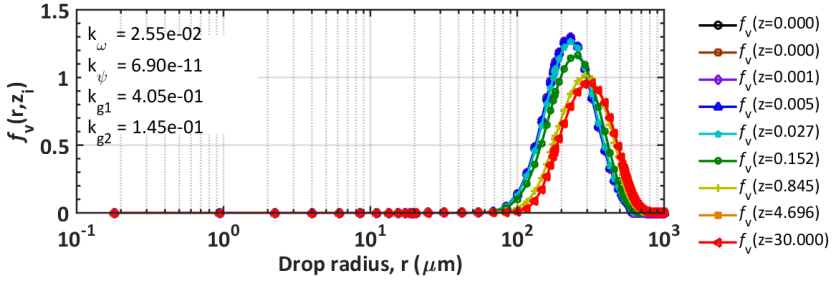

Volume density distribution

(b)

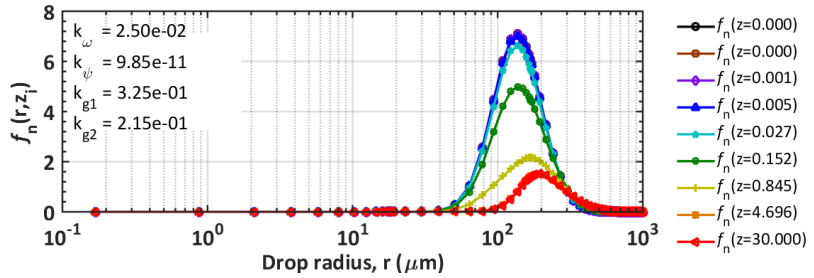

Number density distribution

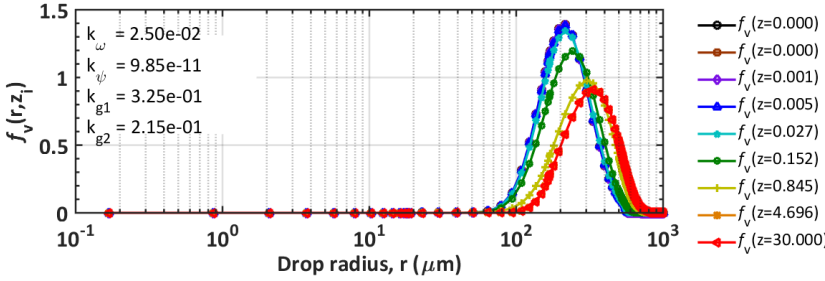

Volume density distribution

(c)

Figure 5.7 Evolution of number density distribution, f_n (top) and volume density distribution, f_v (bottom) along the pipeline as a function of drop radius, r for case I: (a) ge12275a, (b) ge12279a, and (c) ge12284a. The fitting parameters used are shown on top left corner of the plots.

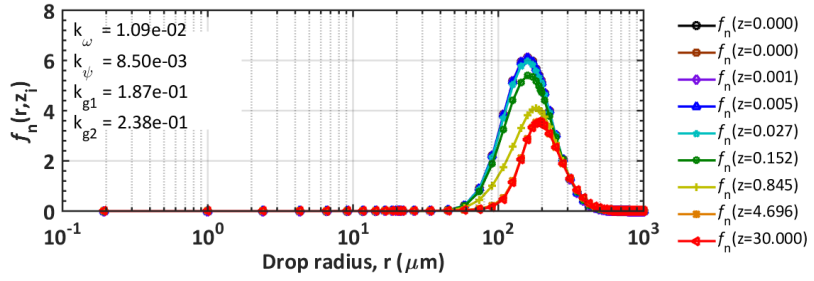

Number density distribution

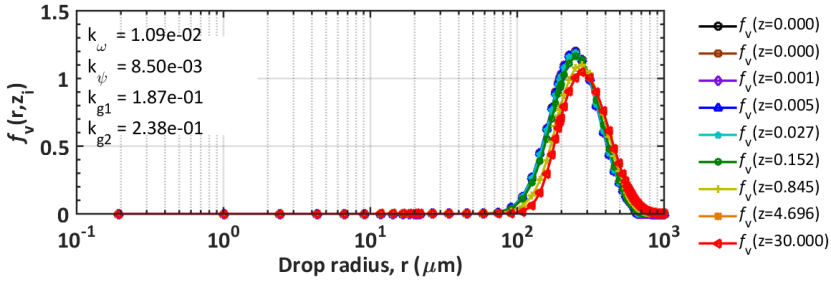

Volume density distribution

(a)

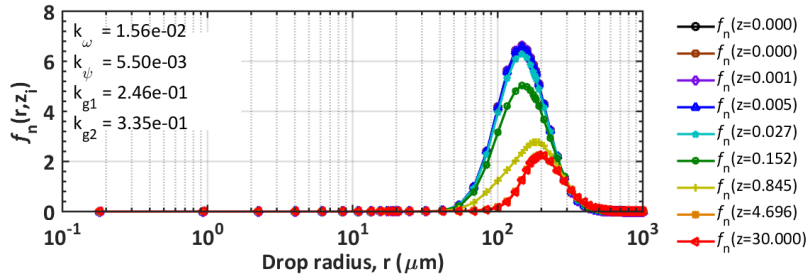

Number density distribution

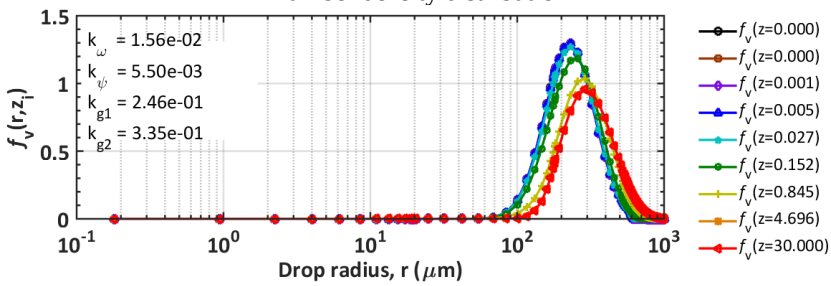

Volume density distribution

(b)

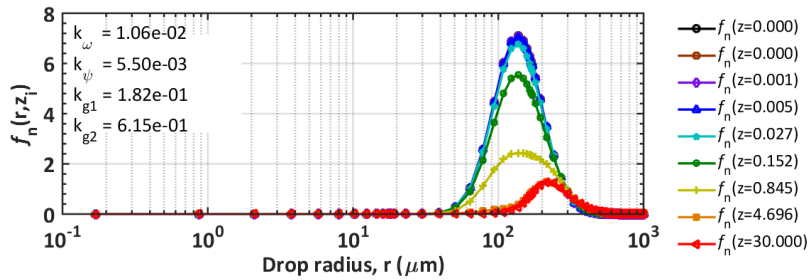

Number density distribution

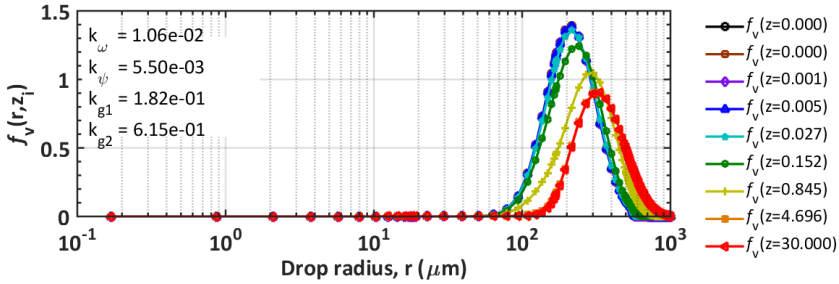

Volume density distribution

(c)

Figure 5.8 Evolution of number density distribution, f_n (top) and volume density distribution, f_v (bottom) along the pipeline as a function of drop radius, r for case II: (a) ge12275a, (b) ge12279a, and (c) ge12284a. The fitting parameters used are shown on top left corner of the plots.

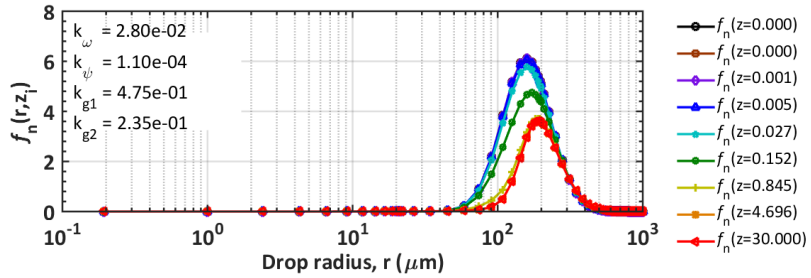

Number density distribution

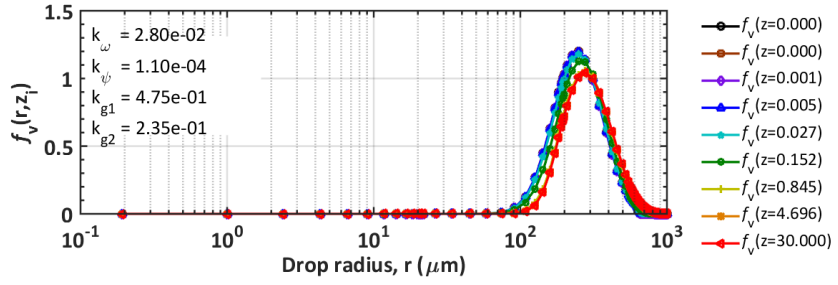

Volume density distribution

(a)

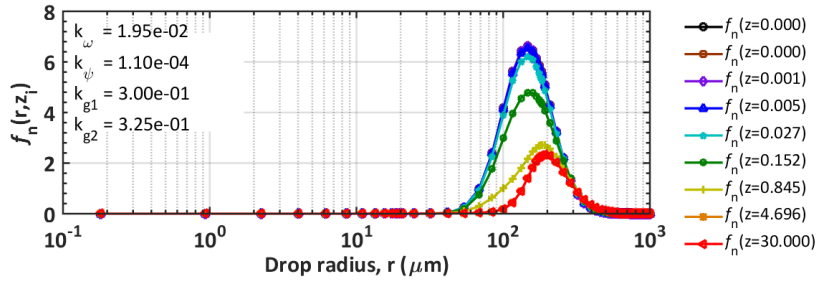

Number density distribution

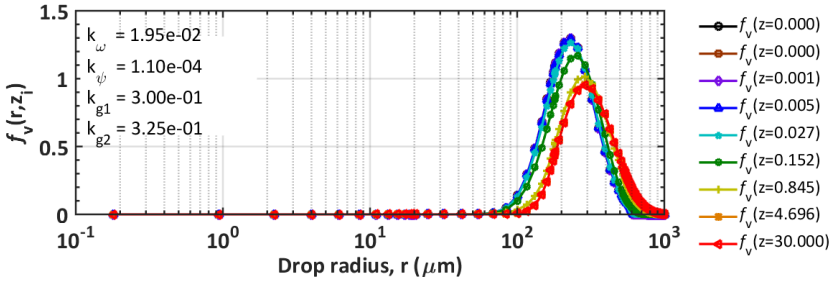

Volume density distribution

(b)

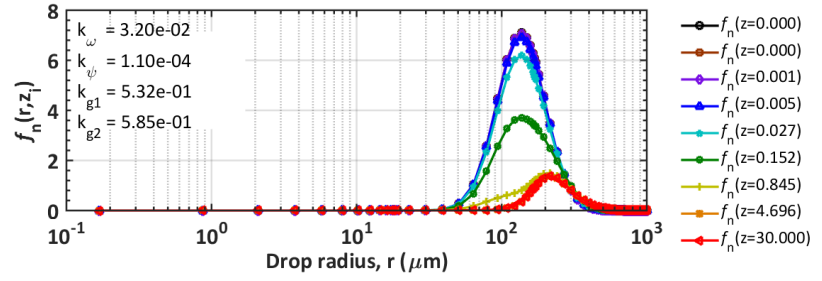

Number density distribution

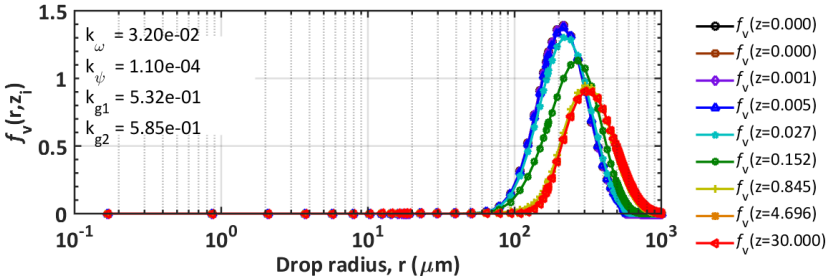

Volume density distribution

(c)

Figure 5.9 Evolution of number density distribution, f_n (top) and volume density distribution, f_v (bottom) along the pipeline as a function of drop radius, r for case III: (a) ge12275a, (b) ge12279a, and (c) ge12284a. The fitting parameters used are shown on top left corner of the plots.

Besides that, to further investigate the changes in the droplets sizes as they travel dynamically through the 30 m pipeline, the average radii profile of the drop density distributions is plotted as depicted in Fig. 5.10(a) and (b). In this figure, the average radii for the number and volume distributions (μ_n and μ_v) are plotted as a function of axial position, z for all the three cases and data sets. The results in Fig. 5.10 show that, the average radii for number density distribution, μ_n and volume density distribution, μ_v increased as the droplets transport from the beginning towards the end of the pipeline. This indicates that, the coalescence process is initially dominating over breakage in the overall system behavior due to the increase in magnitude of the average radii (i.e., higher probability of droplets to coalesce and forming larger droplets than breakup at the beginning of the pipe) for both number and volume density distributions. The results are simulated based on the best fitting parameters and initial distributions for each case. Aside that, from all the data sets evaluated, data set ge12284a is found to experience higher relative change (i.e., larger magnitude of

mean radii) along the pipeline particularly at the equilibrium state (approaching the end of the pipeline) compared to data sets ge12275a and ge12279a.

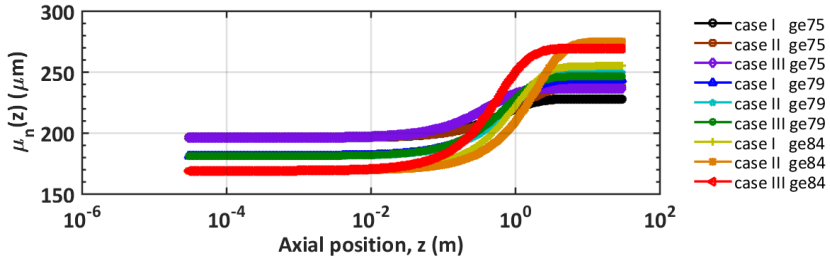

(a)

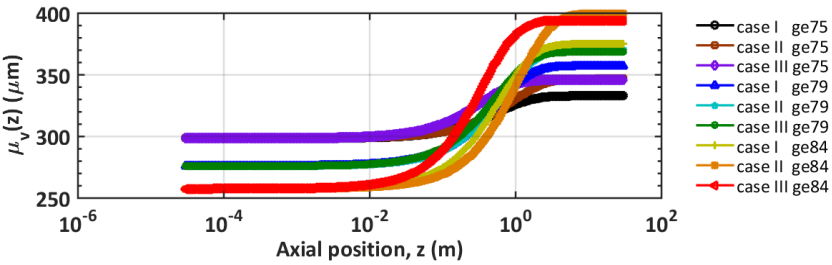

(b)

Figure 5.10 The average radii of (a) the number distribution, μ_n and (b) volume distribution, μ_v versus the axial position in the pipe, z for all cases and data sets.

This is most likely owing to the different in magnitude of average flow velocity, U in all of the experimental data sets. In this respect, data set ge12284a contains the highest average flow velocity, U followed by data sets ge12279a and ge12275a. Hence, by taking this into consideration and based on the initial condition, the data set ge12284a is expected to experience greater kinetic energy from the turbulent eddies which ultimately leads to high breakup of the droplets at the beginning of the pipe. This is due to the fact that, turbulent kinetic energy supplied is sufficient or has exceeded the surface energy of the droplets. The strong turbulent fluctuations in the flow means high energy dissipation rate and more droplets

are likely to break which results in higher f_n and f_v for small size droplets at the beginning of the pipeline as depicted in Fig. 5.7, 5.8, and 5.9 (large quantity of smaller droplets at the onset of the pipe). Schümann, (2016) supported the assumption in his experimental study of oil-water pipe flow. He concluded that, higher mixture velocities increase the possibility of the droplets to breakup and the droplet sizes decrease at higher velocity with increasing Reynolds numbers. In this respect, more droplets will coalesce (high μ_n and μ_v) and form due to smaller sizes droplets produced at onset of the pipes. It worth noting that, In Fig. 5.10(a) and (b), case II and case III are found to predict higher mean radii than case I for all the data sets studied (i.e., ge12275a, ge12279a, ge12284a). This suggests that, the mechanisms employed in the model for case II and case III have a tendency to predict high mean radii in the system. This is because in case II, the coalescence efficiency by Chesters (1991) from the film drainage model is considered from the deformable droplets at fully mobile interfaces (see Fig. 2.11(c) in Chapter 2 of this thesis). In this context, the fully mobile interfaces are expected to experience faster film drainage than case I at immobile interfaces (Æther, 2002). In other words, the rate of coalescence efficiency is higher in case II resulting in larger mean radii as demonstrated in Fig. 5.10(a) and (b). This process is suitable for a system having pure fluids (i.e., no impurities or surfactants) or low viscosity fluids where viscous forces are negligible (Chesters, 1991).

On the other hand, in case I, the film drainage model of deformable droplets at immobile interfaces proposed by Coulaloglou and Tavlarides (1977) gives a lower magnitude of mean radii in comparison to case II and III. This is owing to the model developed by Coulaloglou and Tavlarides (1977) that takes into account the viscous stress effect from the viscosity of the dispersed phase or/and specific surfactant soluble concentration in the system (Liao and Lucas, 2010) as well as the effect of local turbulent intensities at high volume fraction $(1 + \phi)$. It is worth noting that, the effect of local turbulent intensities at high volume

fraction $(1+\phi)$ effectively reduces the rate of collision frequency (ω_c) due to the indirect proportionality influence of the term as illustrated in Table 5.4. For these reasons, the probabilities of droplets to form larger droplets are lower and resulting in small magnitude of mean radii. Furthermore, if there is a presence of viscous effects at the interfaces, it is expected that the drainage time will be sufficiently longer than the contact time, thus some droplets may not be able to coalesce. As discussed by Kamp et al., (2017), in film drainage model, the droplets must remain in contact for sufficient time until the intervening liquid film thins to its critical thickness at which $t_{contact} > t_{drainage}$ (refer to Fig. 2.8 in Chapter 2 of this thesis) for coalescence to occur. On the other hand, in case III, the coalescence efficiency model proposed by Simon (2004) is strongly dependent on kinetic collision energy (as shown in Table 5.4 for coalescence kernels). In this respect, the higher the kinetic energy (i.e., higher flow velocity, U) as described in data set ge12284a, the more efficient the coalescence process will become (bigger droplet formed). Hence, the probability of coalescence (ψ_e) from drop collision process increases if the kinetic collision energy is greater than the surface energy holding the droplet together (i.e., $E_k > E_\sigma$). Nevertheless, by taking into account the complexity of the model and the turbulent flow behavior, the predictions (results) are considered satisfactory based on the individual mechanisms as they appropriately described the essence of droplets behavior in emulsion of oil and water. In addition, the results on average radii may have important implication in terms of accessing designing strategies specifically for multiphase separator system as well as droplet movement describing the sedimentation and coalescence profiles (Jeelani and Hartland, 1998; Yu and Mao, 2004).

Apart from that, the simulations results in both figures (5.10a and 5.10b) also indicate that the mean radii for number and volume density distributions (μ_n and μ_v) are approaching equilibrium in which no significant net changes in drop sizes after they surpassed the 1 m length of the pipe. In this case, the mean radii μ_n and μ_v are said to have equilibrate once

they reached the point where they are no longer growing (toward the end of the pipe length). This is due to the fact that, the system is having a balance between the coalescence and breakage processes. In this regard, the length at which the equilibrium achieved is called L_{eq} and it is set to the axial position of z-axis. Table 5.8 elucidates the length of equilibrium, L_{eq} based on the mean radii on each cases and pipe flow data for the set of best fitting parameters (details in Table 5.7). Table 5.8 also calculates the time required for each length once it reached the state of equilibrium. The length of equilibrium L_{eq} is an important number to measure because it plays a major role in the overall system behaviour. The steady and consistent magnitude of average drop radii approaching the end of the pipeline determines how fast the system can achieve the length of equilibrium, L_{eq}.

Table 5.8 Overview of length equilibrium, L_{eq} and time equilibrium, T_{eq} for number and volume density distributions at every cases and data sets

Data set	Case	L_{eq_n} from μ_n	L_{eq_v} from μ_v	$T_{eq_n} = \frac{L_{eq_n}}{U}$	$T_{eq_v} = \frac{L_{eq_v}}{U}$
	Case I	4.16 m	3.82 m	2.45 s	2.25 s
Ge12275a	Case II	4.79 m	4.32 m	2.82 s	2.54 s
	Case III	3.78 m	3.65 m	2.23 s	2.15 s
	Case I	4.79 m	4.35 m	2.39 s	2.18 s
Ge12279a	Case II	5.52 m	4.66 m	2.76 s	2.33 s
	Case III	3.62 m	3.34 m	1.81 s	1.67 s
	Case I	4.16 m	3.62 m	1.66 s	1.45 s
Ge12284a	Case II	6.36 m	5.72 m	2.54 s	2.28 s
	Case III	2.06 m	1.35 m	0.82 s	0.54 s

In a nutshell, the length of equilibrium, L_{eq} showed in Table 5.8 illustrates that the time of equilibrium is influenced by the velocity, U. In this respect, with the increase of velocity, U from data set ge12275a to ge12284a, the system is observed to reach the equilibrium at faster rate. Furthermore, the results also demonstrate that, case III has reached the length of equilibrium, L_{eq} earlier compared to case I and case II. This is potentially due to the energy model proposed by Simon, (2004) in the coalescence efficiency function and combined with the turbulent fluctuation model from the breakage kernel which has greatly affects the overall system behavior. In addition, case III consists of both coalescence and breakage models developed from the similar mechanism of turbulent energy relationship. Hence, as the turbulent energy increases particularly from data set ge12275a to ge12284a, the equilibrium state of the system is accelerated. In other words, the higher the kinetic energy supplied from the turbulent eddies, the faster the system is expected to reach the stability (equilibrium). On the other hand, changing and altering the fitting parameters specifically the k_{ω} and k_{g_1} will also have a greater effect on the behavior of L_{eq}. In this respect, the higher the magnitude of fitting parameters k_{ω} and k_{g_1}, the faster the system reaches equilibrium (refer to Part I of Chapter 4 for details). This is mainly because of the direct effect on the rate of breakage and coalescence frequencies as depicted in Table 5.3 and Table 5.4. Therefore, the system will growth and equilibrates faster when the value of k_{ω} and k_{g_1} are set at substantially higher.

It is of interest in this study to investigate the dynamic evolution of drop density distribution in terms of coalescence and breakage rates throughout the pipeline. To achieve this, the best fit parameters shown in Table 5.7 are employed for every case to generate the results related to the breakage and coalescence rates functions. Fig. 5.11 until Fig. 5.13, illustrate the dynamic evolution of drop density distribution in terms of the total coalescence rate (top), R_{C_t} and total breakage rate (bottom), R_{B_t} as a function of drop radius, r at nine

different axial positions, z in the 30 m pipe. The total rate is accounted for the birth and death terms from the breakage and coalescence events. In these figures, the negative section of the curves indicates the death of the droplets due to the coalescence and breakage processes, while the positive section of the curves specifies the birth of the droplets owing to coalescence and breakage developments. Essentially, the plots in Fig. 5.11 until 5.13 provide an insight on the droplets behavior in terms of coalescence and breakage rates for all the cases and data sets investigated. From these figures, it clearly shows that the total coalescence rate is higher at the beginning of the pipeline and gradually decreases towards the end of the pipeline. This is stemming from the fact that large quantity of smaller droplets initially enhanced the collision rate between droplets. Moreover, film drainage is faster for small droplets due to the small surface area and for droplets with low surface energy particularly, for case I and II. While in case III, the efficiency of coalescence significantly increases with increasing energy of collision (energy model) from the turbulent eddies (energetic collision) as shown in data set ge12275a to data set ge12284a. It is worth noting that, case III produced the highest birth rate of coalescence among the three cases and data sets simulated, which is approximately in the range of $R_{C_t} \approx 90 - 120$ $\mathrm{m^{-1}s^{-1}}$. This suggests that, case III has the highest probability for coalescence to occur than case II and case I due to the higher magnitude of total coalescence rate produced. By taking into account the mechanism of energy-induced coalescence from the energy model by Simon, (2004), the coalescence efficiency may have been strongly intensified in the system which results in significant increase of overall total coalescence rate. Apart from that, at low r values, the total coalescence rate, R_{C_t} is found to be in the negative section. This is expected because smaller droplets present at the beginning of the pipeline are more likely to coalesce and forming larger droplets. Subsequently, the larger droplets formed initially from the coalescence process will breakup into smaller droplets (birth by breakage) as bigger droplets are more

likely to break than smaller ones. In general, R_{C_t} is found to decrease as z increases, which indicates that the larger droplets formed during the coalescence process are breakup into smaller droplets as breakage process becomes stronger towards the end of the pipeline until both systems equilibrate. Further evidence of this observation stems from the fact that initial droplets are too small to break which restricted the breakage process at the early stage of the pipeline. However, as z increases, breakage is growing in dominance because larger droplets are more likely to break than coalesce.

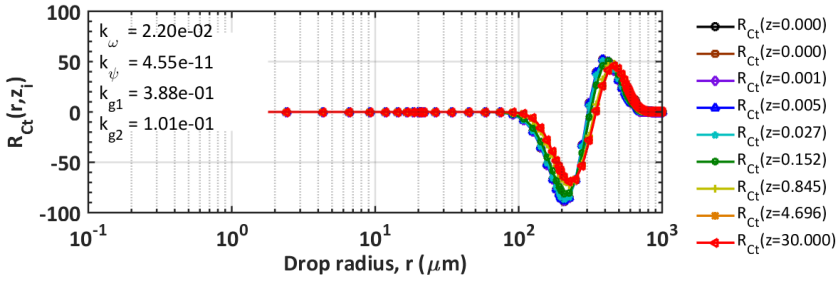

Total coalescence rate

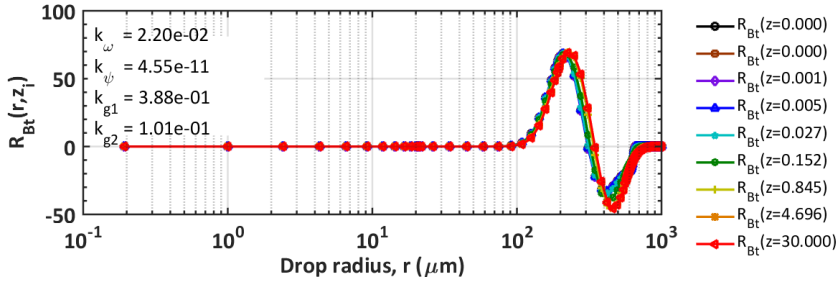

Total breakage rate

(a)

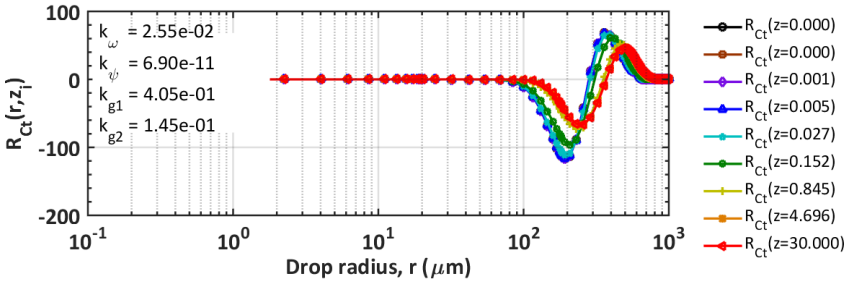

Total coalescence rate

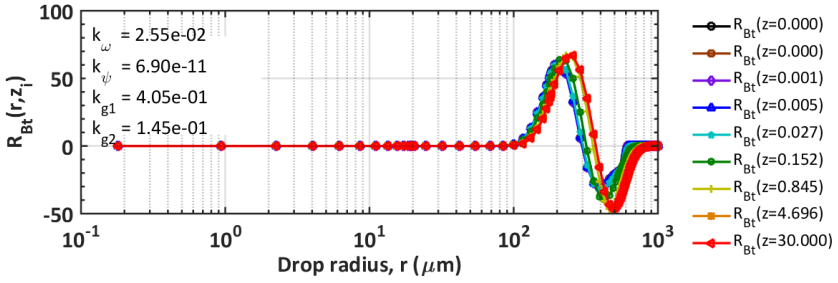

Total breakage rate

(b)

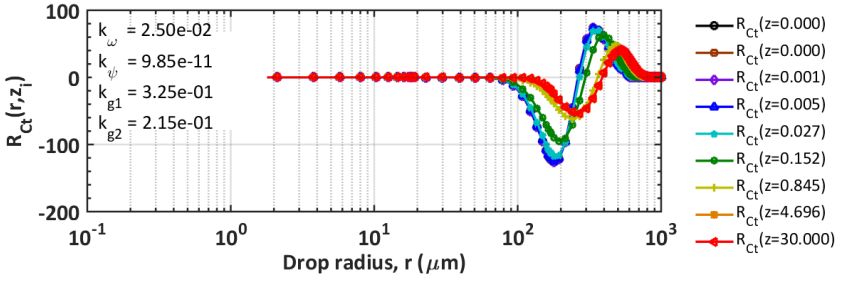

Total coalescence rate

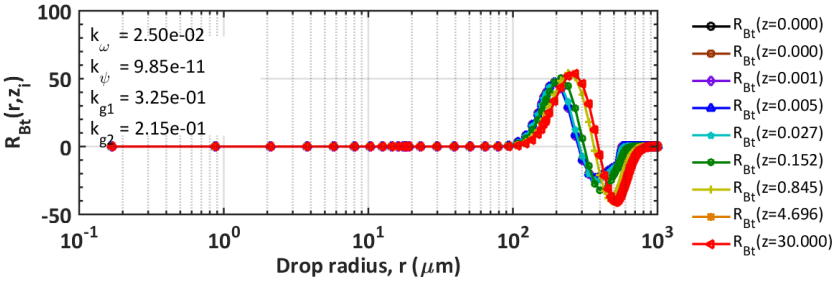

Total breakage rate

(c)

Figure 5.11 Evolution of the total coalescence rate R_{C_t} (top) and evolution of the total breakage rate, R_{B_t} for case I and data set of: (a) ge12275a, (b) ge12279a, and (c) ge12284a. Both rates are plotted as a function of droplet radius, r at nine different locations in the pipe. The fitting parameters used are shown on top left corner of the plots.

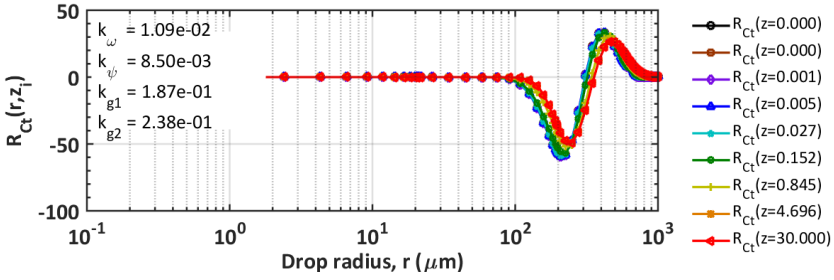

Total coalescence rate

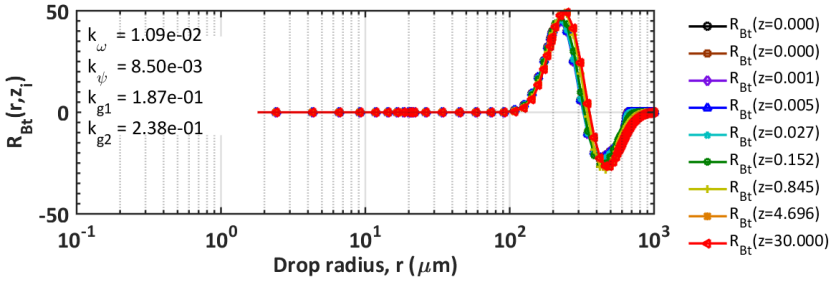

Total breakage rate

(a)

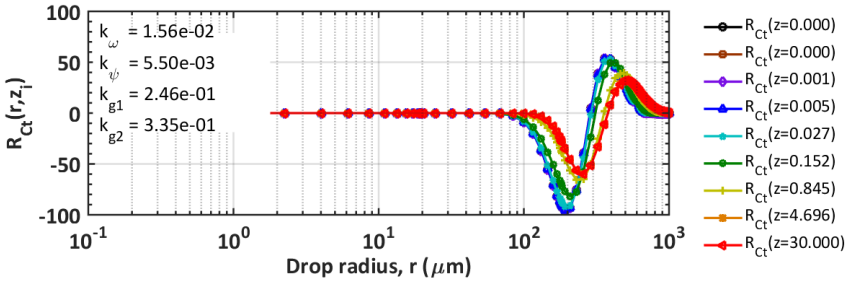

Total coalescence rate

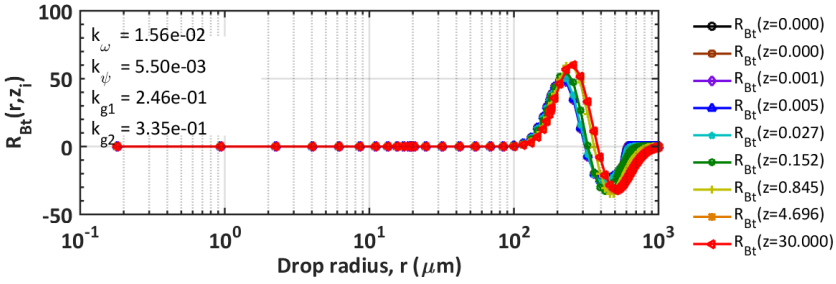

Total breakage rate

(b)

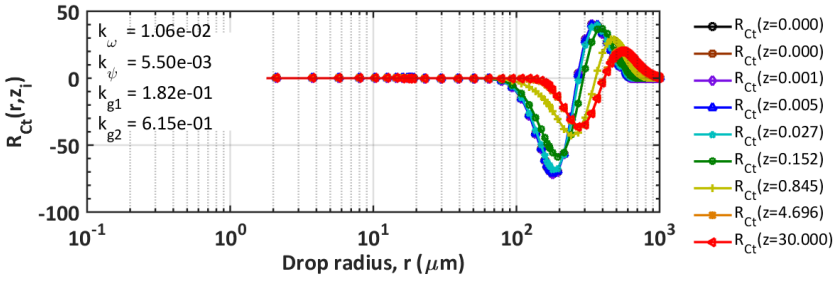

Total coalescence rate

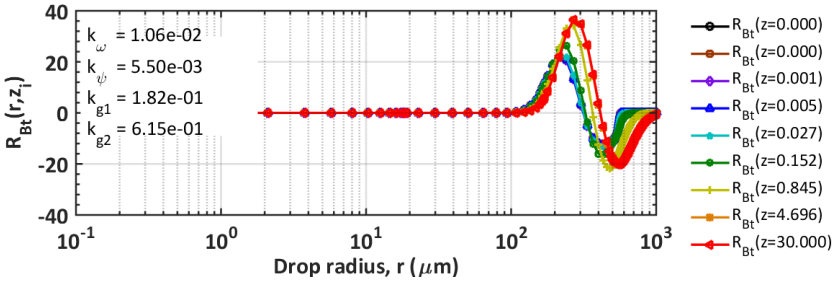

Total breakage rate

(c)

Figure 5.12 Evolution of the total coalescence rate R_{C_t} (top) and evolution of the total breakage rate, R_{B_t} for case II and data set of: (a) ge12275a, (b) ge12279a, and (c) ge12284a. Both rates are plotted as a function of droplet radius, r at nine different locations in the pipe. The fitting parameters used are shown on top left corner of the plots.

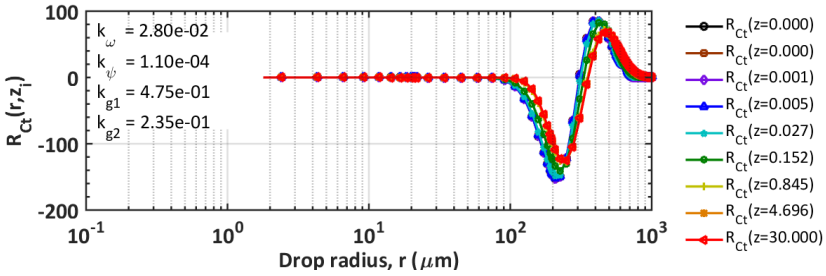

Total coalescence rate

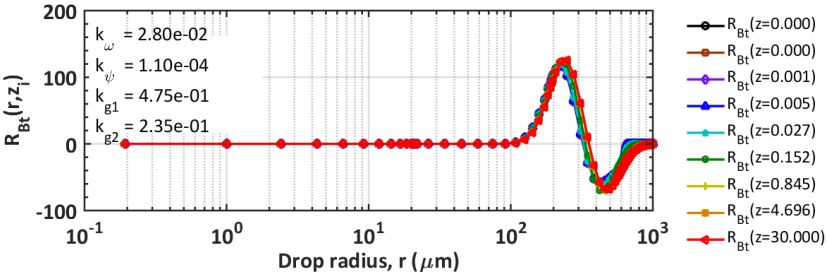

Total breakage rate

(a)

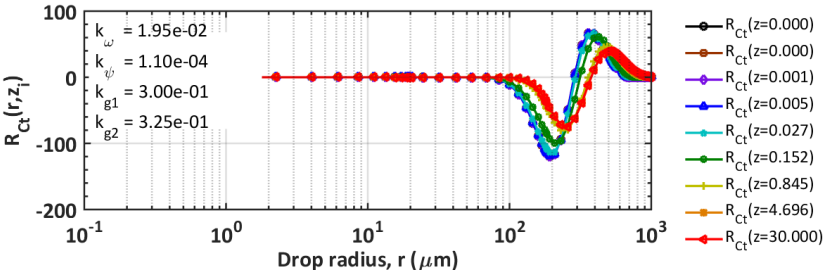

Total coalescence rate

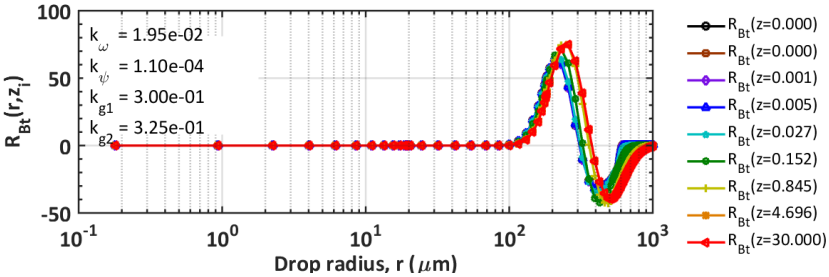

Total breakage rate

(b)

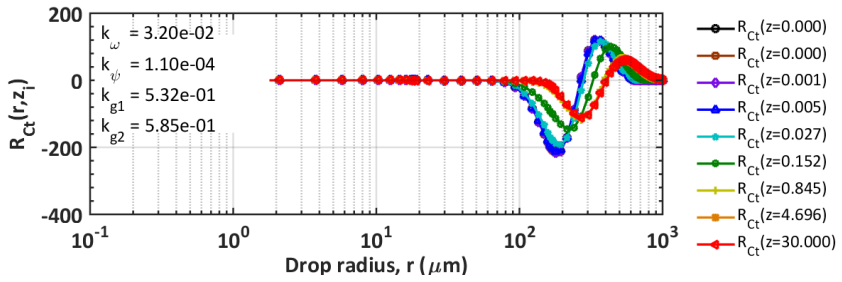

Total coalescence rate

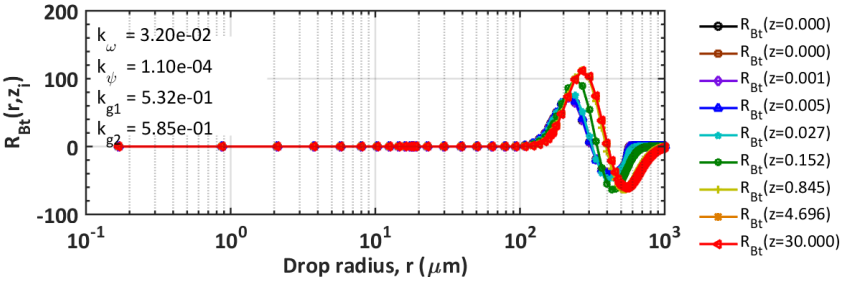

Total breakage rate

(c)

Figure 5.13 Evolution of the total coalescence rate R_{C_t} (top) and evolution of the total breakage rate, R_{B_t} (bottom) for case III and data set of: (a) ge12275a, (b) ge12279a, and (c) ge12284a. Both rates are plotted as a function of droplet radius, r at nine different locations in the pipe. The fitting parameters used are shown on top left corner of the plots.

The bottom sections of Fig. 5.11(a), (b), and (c), until Fig. 5.13(a), (b), and (c) show the dynamic evolution of the drop density distribution in terms of total breakage rate in the 30 m pipeline for all the data sets and cases. As depicted in Fig. 5.11 until Fig. 5.13, the total breakage rate, R_{B_t} is found to have increased towards the end of the pipeline, in other words R_{B_t} behaves in an exactly opposite trend to R_{C_t}. The similar behaviour can be observed for all the cases and data sets. This suggests that breakage becomes dominant and stronger as z increases. Ideally, breakage occurs due to the interaction between the larger droplets and

turbulent eddies. Therefore, increase in number of larger droplets from coalescence process at the early stage of the pipeline has significantly affects the breakage to grow in dominance as they travel throughout the axial position, z. This is true considering larger eddies are responsible for breakup and with the presence of larger size droplets from coalescence process initially, the tendency of breakage to occur towards the end of the pipeline increased. It is worth noting that, very small eddies do not have sufficient energy to affect breakage compared to large eddies (Prince and Blanch, 1990). In this respect, the breakage process is highly influenced by the size of droplets and the turbulent energy in the system. According to Kumar et al., (1991), a drop will break under the influence of turbulent inertial stresses and under this condition, the physical of the droplets can no longer held together which results in deformation of the droplet as illustrated in Fig. 5.14. With that in mind, one would expect faster breakage rate when the emulsion contains larger size of droplets and high energy dissipation rate (ε) in the system. It should be emphasized that that these events are highly dependent on the initial distributions for each case and the set of fitting parameters. On the other hand, the positive curve (birth) of R_{B_t} in the same figure (Fig. 5.13(a), (b) and (c)) for case III is observed to produce the highest rate compared to case I and II with approximately in the range of $R_{B_t} \approx 80 - 120$ m^{-1}s^{-1} for all the data sets simulated. This indicates that, the model simulated in case III promotes higher breakage rate compared to the other cases, similar to the event observed in total coalescence rate (i.e., higher rate). The results provide further confirmation that case III may predict high drop rates and the mean radii in the system.

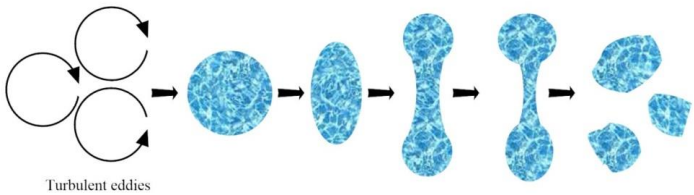

Figure 5.14 Drop breakage chronologies by turbulent kinetic energy

5.3 Chapter summary

This chapter discussed the regression of the dynamic evolution of the drop size density distribution of oil-water emulsion in a 30 m turbulent pipe flow. From the results, the drop behavior over the turbulently flow in pipe are found to be very promising and the models simulated have shown a good agreement with the experimental data. The fitting parameters tested are fitted accordingly the drops volume density distribution at the final location perfectly. The best fit results between the experimental data and simulation demonstrated that the methodologies proposed in this modelling work (as discussed in Chapter 3) have proved to be working effectively. Hence, the models can be considered reliable and robust from all the results depicted. One manuscript (Part III) has been prepared for this discussion and can be found in Appendix D of this thesis.

CHAPTER 6

6 CONCLUDING REMARKS

In this recent work, the dynamic evolution of the drop size density distribution of liquid-liquid emulsions in turbulent pipe flow was investigated. The results and discussions of this work are divided into two main parts, in which Part I covered the model behavior and parametric effects and Part II discussed the comparison between the simulation and experimental data for various breakage and coalescence models. In Part I of this research, the general form of a mathematical model to simulate the dynamic evolution of drop size density distribution in turbulently flowing liquid-liquid dispersions through pipeline was presented using the method of population balance equation (PBE). In the context of model development, possible methodology is elucidated incorporating the breakage process due to turbulent fluctuations and coalescence process from the film drainage between droplets. Moreover, the properties of the mixture liquids and the flow conditions are also incorporated in order to understand the overall system behavior of the drop sizes evolution in liquid-liquid dispersions. The model also suggests that the evolution of number density distribution, volume density distribution, mean radii, standard deviations, total coalescence and breakage rates, and total growth rates for a liquid-liquid system are take place in isotropic turbulence condition at any position over a long distance pipeline. The performances of both breakage and coalescence processes are presented based on how fitting parameters, k_{g_1} and k_{ω} k_{ψ} and k_{g_2} are change from case to case (i.e., case I, case II, and case III). In addition, for any position in the pipeline, the model is able to simulate the evolution of breakage and coalescence processes in terms of birth and death rates as well as their total growth rates. At the same time, the advantages of solving the PBE in the form of volume density distribution f_v compared to number density distribution f_n are also discussed as well as the

error analysis of using the spectral element in the orthogonal collocation method (i.e., $N_t = 6$) to identify the best numerical solutions. One of the important contributions of this model work is coming from the suggestion of converting the solution for PBE from number density distribution f_n to volume density distribution f_v. The results have shown that, solving the PBE in the form of f_v provide more stability and consistency to numerical solutions as volume remains constant due to volume conservation, while, f_n changed significantly during drop growth process as number is not conserved (i.e., not consistent). In brief, the study provides an insight of the modelling strategies and the solutions to the PBE towards understanding and describing the overall system behavior of the drop size density distribution in turbulently flowing liquid-liquid dispersions.

On top of that, the discussions in Part I (Chapter 4) of this thesis are continued with the study of the model performance under various parametric effects to acquire understanding and to elucidate the overall system behavior. In this respect, several parameters are varied such as energy dissipation rate, ε, volume fraction, ϕ, and four fitting parameters, k_ω, k_ψ, k_{g_1}, and k_{g_2}. The performances of both breakage and coalescence processes are also assessed and evaluated based on these parametric effects. The model is also modified to incorporate the damping effect with the factor of $(1 + \phi)$ to account for turbulent intensities at high volume fraction suggested by Coulaloglou and Tavlarides (1977). Overall, the results are considered satisfactory as they are in good agreement with the experimental data and theoretical studies. The results shown that, the mean radii increase as volume fraction increases and decrease when energy dissipation rate increases. This is followed by coalescence gradually growing in dominance as dispersed volume fraction increases and conversely when energy dissipation rate is set higher. Apart from that, sum of squares (SSQ) plots of the regression behavior are also presented and analyzed. The results indicate that the interaction between all four fitting parameters is crucial in finding the best local minima. In

general, the four fitting parameters play an important role in changing the behavior of coalescence and breakage models. Essentially, the study adds detail in understanding of the interplay between various parametric effects on the coalescence and breakage mechanisms and their relationship that contribute to the overall behavior of the drop size distributions. The results are encouraging and provide useful information for the understanding of the model in simulating and solving the dynamic evolution of liquid-liquid emulsions in turbulent pipe flow.

Finally, the regression of experimental drop size density distribution in turbulent pipe flow is investigated. In this present work, the performance of two different breakage kernels and three separate coalescence kernels by Coulaloglou and Tavlarides (1977), Hsia and Tavlarides (1980), Vankova et al., (2007), Prince and Blanch (1990), Chesters (1991), and Simon (2004) are assessed and evaluated. The model and experimental data are directly compared in terms of volume density distribution at final location in the pipe. Overall, satisfactory agreement is observed in all of the model's predictions with the experimental pipe flow data. Based on the analysis of the results, turbulent fluctuation is the best mechanism for breakage process, wherein, film drainage is the suitable mechanism to describe for coalescence process particularly, in turbulently flowing oil-water emulsions in pipe flow. However, discrepancies are discovered in terms of mean radii and total drop rate predicted between the models studied. The models in Case III are found to promote higher breakage and coalescence rates compared to case I and case II. Aside that, case II and case III are found to produce higher mean radii in comparison to case I. The film drainage model employed in case I from Coulaloglou and Tavlarides (1977) at immobile interfaces is found to be the better model to describe the oil-water system in pipes. This is true considering that, the model incorporates the viscous shear stress effect between two different liquids (viscous liquid) as well as the effect from local volume fraction $(1 + \phi)$. It is also worth noting that,

every model investigated in each case produced reasonable results for all the data sets of different velocity conditions. However, one should expect differing in the magnitude of the fitting parameters and higher mean radii as well as greater changes in total drop rate. In addition, the model and experimental data indicate that the difference in degree of velocity for data set of ge12275a, ge12279a, and ge12284a can affect the rate of coalescence and breakage. That is, increased in velocity leads to higher coalescence and breakage rates as well as faster equilibrium of mean radii (L_{eq}).

CHAPTER 7

7 SUGGESTIONS AND RECOMMENDATIONS FOR FUTURE WORK

It is recommended for the future work to study the dynamic evolution of the drop size distribution by taking into account the aspects of angular and radial effects in the pipe flow. It is because Schümann, (2016) and Lovick and Angeli (2004) have shown from the experimental evidence that, droplets at the center of the pipe are larger than the droplets found near the wall of the pipe. This is due to the fact that high shear rate close to the wall promote the breakup process of the particles and leads to smaller droplet size. Another essential aspect to consider in the future work is the physical state of the matter (i.e., gas, liquid, solid). Variation in terms of the phases, for instance gas-liquid system may provide profound understanding in modeling a more complicated three phase flow system (i.e., gas-oil-water system or gas-liquid-solid system) which is becoming more common in the industries, particularly in petroleum production. The study of gas-liquid system in turbulently flowing pipeline will provide many significant information such that, the bubble size density distribution, the interactions behaviour between bubbles in pipes, and the status of breakage and coalescence rates in the system throughout the pipeline that benefitted the designs of critical equipment such as multiphase separator.

Finally, is it also suggested that, one should consider the experimental data of drop size density distribution (either number or volume density distribution) to be measured at the midway of the pipeline apart from the inlet and the outlet. This measurement will provide additional information of the drop size behaviour at the midway of the pipeline. Taking into account the midway distribution will greatly contribute in finding the best fit at the final location of the drop size density distribution. Hence, robust regression results can be expected.

REFERENCES

Abidin, M. I. I. Z., Raman, A. A. A., Nor, M. I. M., 2015. Mean drop size correlations and population balance models for liquid-liquid dispersion. AIChE. J. 61(4), 1129-1145.

Æther, L., 2002. Coalescence and breakup of drops and bubble. Ph.D. Dissertation. Norwegian university of science and technology, NTNU, Norway.

Akinola, F., Borissova, A., Wang, X. Z., 2013. Extended method of moment for general population balance models including size dependent growth rate, aggregation and breakage kernels. Comp. Chem. Eng. J. 56, 1-11.

Alopaeus, V., Koskinen, J., Keskinen, K. I., 1999. Simulation of the population balances for liquid-liquid systems in a nonideal tank. Part I Description and qualitative validation of the model. J. Chem. Eng. Science. 54, 5887-5899.

Alopaeus, V., Koskinen, J., Keskinen, K. I., Majander, J., 2002. Simulation of the population balances for liquid-liquid systems in a nonideal tank. Part II – parameter fitting and the use of the multiblock model for dense dispersion. J. Chem. Eng. Science. 57, 1815-1825.

Alexopoulos, A.H., Roussos, A.I., Kiparissides, C., 2004. Part I: dynamic evolution of the particle size distribution in particulate processes undergoing combined particle growth and aggregation. J. Chemical Engineering Science. 59, 5751–5769.

Andersson, R., Andersson, B., 2006. On the breakup of fluid particles in turbulent flows, AIChE J. 52, 2020-2030.

Angeli, P., Hewit, G. F., 1999. Flow structure in horizontal oil–water flow. Int. J. Multiphase Flow 26, 1117–1140.

Arirachakaran, S., Oglesby, K. D., Malinowsky, M. S., Shoham, O., Brill, J. P., 1989. An Analysis of oil/water flow phenomena in horizontal pipes. SPE-18836. Presented at the SPE Production Operation Symposium, Oklahoma,U.S.A.

Asiagbe, K. S., 2018. Numerical simulation of gas-liquid bubbly flows. Ph.D. Thesis. University of Leeds, UK.

Attarakih, M. M., Drumm, C., Bart, H. J., 2009. Solution of the population balance equation using the sectional quadrature method of moments (SQMOM). J. Chem. Eng. Sci. 64, 742−752.

Azizi, F., Taweel, A, M., 2011. Turbulently flowing liquid-liquid dispersions. Part I: drop breakage and coalescence. Chem. Eng. J. 166, 715-725.

Azizi, F., Taweel, A, M., 2010. Algorithm for the accurate numerical solution of PBE for drop breakup and coalescence under high shear rates. Chem. Eng. Science J. 65, 6112-6127.

Bilicky, Z., Kestin, J., 1987. Transition criteria for two-phase flow patterns in vertical upward flow. Int. J. Multiphase Flow. 13, 283-294.

Becher, P., 2001. Emulsions: theory and practice. Third edition. Oxford university press, New York, NY.

Bennett, M. K., Rohani, S., 2001. Solution of population balance equations with a new combined Lax-Wendroff/Crank-Nicholson method. J. Chem. Eng. Sci. 56, 6623−6633.

Bochev, P., Gunzburger, M. D., 2009. Least-squares finite element methods. Springer, New York.

Boxall, J. A., Koh, C. A., Sloan, E. D., Sum, A. K., Wu, D. T., 2010. Measurement and Calibration of Droplet Size Distributions in Water-in-Oil Emulsions by Particle Video Microscope and a Focused Beam Reflectance Method. Ind. Eng. Chem. Res. 49(3), 1412-1418.

Briceño, M., Salager, J. L., Bertrand, J., 2001. Influence of the dispersed phase content and viscosity on the mixing of concentrated oil-in-water emulsions in the transition flow regime. J. Chem. Eng. Res. Des. 79(8), 943-948.

Carrica, P. M., Drew, D., Bonetto, F., Lahey Jr, R. T., 1999. A polydispersed model for bubbly two-phase flow around a surface ship. Int. J. Multiphase flow. 25, 257-305.

Chan, D. Y. C., Klaseboer, E., Manica, R., 2011. Film drainage and coalescence between deformable drops and bubbles. Soft Matter J. 6, 2235-2264.

Chatzi, E., Lee, J. M., 1987. Analysis of interactions for liquid-liquid dispersions in Agitated vessels. Ind. Eng. Chem. Res. 28, 1704-1711.

Chatzi, E., Gavrielides, A. D., Kiparissides, C., 1989. Generalized model for prediction of the steady-state drop size distributions in batch stirred vessels. Ind. Eng. Chem. Res. 26(11), 2263-2267.

Chen, Z., Prüss, J., Warnecke, H. J., 1998. A population balance model for disperse systems: drop size distribution in emulsion. Chem. Eng. Science. J. 53(5), 1059-1066.

Chesters, A. K., 1991. The modelling of coalescence processes in fluid-liquid dispersions. A review of current understanding. J. Chem. Eng. Research and Design. 69, 259-270.

Clift, R., Grace, J. R., Weber, M. E., 1978. Bubbles, drops and particles, Academic press. New York, USA.

Cristini, V., Blawzdziewicz, J., Loewenberg, M., Collins, L. R., 2003. Breakup in stochastic Stokes flows: sub-Kolmogorov drops in isotropic turbulence. J. Fluid Mechanics. 492, 231–250.

Colin, C., Riou, X., Fabre, J., 2004. Turbulence and shear-induced coalescence in gas-liquid pipe flows. Fifth international conference on multiphase flow. IMCF'04, Yokohama, Japan. May 30 – June 4.

Coulaloglou, C.A., Tavlarides, L.L. 1977. Description of interaction processes in agitated liquid-liquid dispersions. J. Chem. Eng. Science 32, 1289 -1297.

Davis, R. H., Schonberg, J. A., Rallison, J. M., 1989. The lubrication force between two viscous drops. J. Physics of Fluids. 1, 77-81.

Deju, L., Cheung, S.C.P., Yeoh, G.H., Qi, F., Tu, J., 2015. Comparative analysis of coalescence and breakage kernels in vertical gas-liquid flow.

DeRoussel, P., Khakhar, D. V., Ottino, J. M., 2001. Mixing of viscous immiscible liquids. Part 1: Computational models for strong–weak and continuous 4ow systems. J. Chem. Eng. Science; 56(19), 5511–5529.

Derjaguin, B. V., Kussakov, M. M., 1939. Anomalous properties of thin poly-molecular films. Acta Physicochim. URRS. 10, 25-30.

Dorao, C. A., Jakobsen, H. 2006a. A least squares method for the solution of population balance problems. J. Chem. Eng. Science. 30, 535-547.

Dorao, C. A., Jakobsen, H. 2006b. Application of the least-squares method for solving population balance problems in $\mathbb{R}^{d+1}$. J. Chem. Eng. Science. 61, 5070-5081.

Dowding, P. J., Goodwin, J. W., Vincent, B., 2001. Factors governing emulsion droplet and solid particle size measurements performed using the focused beam reflectance technique. J. Coll. Surf. A: Phys. Eng. Aspects. 192, 5-13.

Eastwood, C. D., Armi, L., Lasheras, J. C., 2004. The breakup of immiscible fluids in turbulent flows. J. Fluid Mechanics. 502, 309-333.

Elseth, G., 2001. An experimental study of oil-water flow in horizontal pipes. Ph.D. thesis. Telemark University College, Porsgrunn, Norway.

Farr, R.S., 2013. Random close packing fractions of lognormal distributions of hard spheres. Powder Technology. 245, 28-34.

Flores, J.G., Chen, X.T., Sarica, C., Brill, J. P., 1999. Characterization of oil/water flow pattern in vertical and deviated wells. SPE-56108. SPE Prod. Facilities. 14(2), 102-109.

Flórez-Orrego, D., Arias, W., López, D., Velásquez, H. I., 2012. Experimental and CFD study of a single-phase cone-shaped helical coiled heat exchanger: and empirical

correlation. Int. Conference. Eff. Cost. Opt. Sim. Env. Impact of Energy System. June 26-29. Perugia, Italy.

Friedlander, S. K., 1977. Smoke, Dust and Haze, Book, Wiley, New York.

Fu, X.Y., Ishii, M., 2002. Two-group interfacial area transport in vertical air-water flow: I. Mechanistic model. Nucl. Eng. Des. 219(2),143–168.

Galinat, S., Masbernat, O., Guiraud, P., Dalmazzone, C., Nöik, C. 2005. Drop break-up in turbulent pipe flow downstream of a restriction. J. Chem. Eng. Science. 60, 6511-6528.

Gavrielatos, I., Dabirian, R., Mohan, R. S., Shoham, O., 2017. Separation kinetics of oil/water emulsions stabilized by nanoparticles. Preceeding, ASME, Fluids Eng. Division Summer meeting, Waikoloa, Hawaii, USA.

Ghannam, H., Chahboun, A., Diani, M., Addou, M., 2017. Lattice Boltzmann simulations of liquid drop shape on an inclined surface. Int. Conference. Auto. Control Eng. Comp. Science (ACECS). Proceeding Eng. And Tech. 21, 9-13.

Grimes, B. A., 2011. Population balance model for batch gravity separation of crude oil and water emulsions. Part I: model formulation. J. Disp. Science Tech. 33, 578-590.

Gunawan, R., Fusman, I., Braatz, R. D., 2004. High resolution for multidimensional population balance equations. AIChE. J. 50(11), 2738-2749.

Hadnađev, T. D., Dokić, P., Krstonošić, Hadnađev, M., 2013. Influence of oil phase concentration on droplet size distribution and stability of oil-in-water emulsions. Eur. J. Lipid Sci. Technol. 115, 313-321.

Hagesaether, L., Jakobsen, H. A., Svendsen, H. F., 1999. Theoretical analysis of fluid particle collisions in turbulent flow. Chem. Eng. Sci. 54, 4749-4755.

Hart, A., 2014. A review of technologies for transporting heavy crude oil and bitumen via pipelines. J. Petrol. Explor. Prod. Technol. 4, 327-336.

Hemmingsen, P. V., Auflem, I. H., Sæther, Ø., Westvik, A., 2005. Emulsions and emulsion stability: Droplet size distributions of oil-in-water emulsions under high pressures by video microscopy. Taylor and Francis Group. Boca Raton, USA.

Hesketh, R. P., Etchells, A. W., Russell, T. W. F., 1991. Experimental observations of bubble breakage in turbulent flow. J. Ind. Eng. Chem. Res. 30, 835-841.

Hinze, J. O., 1959. Turbulence. 2nd Edition. McGraw Hill. New York.

Howarth, W.J., 1964. Coalescence of drops in a turbulent flow field. J. Chem. Eng. Science. 19, 33-38.

Hulbert, H. M., Katz, S., 1964. Some problems in particle technology: a statistical mechanical formulation. J. Chemical Engineering Science. 9, 555–574.

Hsia, M. A., Tavlarides, L. L., 1980. A simulation model for homogeneous dispersions in stirred tanks. Chem. Eng. J. 20, 225-236.

Ioannou, K., 2006. Phase inversion phenomenon in horizontal dispersed oil/water pipeline flows. Ph.D. Thesis. University College London, UK.

Ismail, A. S. I., Ismail, I., Zoveidavianpoor, M., Mohsin, R., Piroozian, A., Misnan, M. S., Sariman, M. Z., 2015a. Experimental investigation of oil–water two-phase flow in horizontal pipes: Pressure losses, liquid holdup and flow patterns. J. Petroleum Sci. Eng. 127, 409-420.

Ismail, A. S. I., Ismail, I., Zoveidavianpoor, M., Mohsin, R., Piroozian, A., Misnan, M. S., Sariman, M. Z., 2015b. Review of oil-water through pipes. J. Flow Meas. Inst. 45, 357-374.

Jakobsen, H. A., 2008. Chemical reactor modeling: multiphase reactive flows. Berlin, Springer-Verlag.

Jakobsen, H. A., 2014. Chemical reactor modeling: multiphase reactive flows. Second edition. Springer, Switzerland.

Jeelani, S. A. K., Hartland, S., 1998. Effect of dispersion properties on the separation of batch liquid-liquid dispersions. Industrial. Eng. Chem. Res. 37(2), 547-554.

Jeelani, S. A. K., Hartland, S., 1991. Effect of approach velocity on binary and interfacial coalescence. Chemical Engineering Research and Design: transactions of the institution of chemical engineers: Part A 69, 271-281.

Jeffreys, G. V., Davies, G. A., 1971. Coalescence of liquid droplets and liquid dispersion. Recent advances in liquid-liquid extraction book. Edited by: Handson, C. Pergamon Press, New York. 495-584.

Jiang, B., 1998. The least-square finite element method: Theory and applications in computational fluid dynamics and electromagnetics. Springer. Berlin.

John, V., Suciu, C., 2014. Direct discretizations of bi-variate population balance systems with finite difference schemes of different order. J. Chem. Eng. Sci. 106, 39−52.

Karn, A., Shao, S., Arndt, R. E. A., Hong, J., 2016. Bubble coalescence and breakup in turbulent bubbly wake of a ventilated hydrofoil. J. Exp. Thermal and Fluid Science. 70, 397-407.

Kamp, A. M., Chesters, A. K., Colin, C., Fabre, J., 2001. Bubble coalescence in turbulent flows: A mechanistic model for turbulence-induced coalescence applied to microgravity bubbly pipe flow. Int. J. Multiphase Flow. 27, 1363-1396.

Kamp, J., Villwock, J., Kraume, M., 2017. Drop coalescence in technical liquid/liquid applications: a review on experimental techniques and modeling approaches. J. Review in Chem. Eng. 33(1), 1-47.

Khatibi, M., 2013. Experimental study on droplet size of dispersed oil-water flow. Master thesis. NTNU, Norway.

Kocamustafaogullari, G., Ishii, M., 1995. Foundation of the interfacial area transport equation and its closure relations. Int. J. Heat and Mass Transfer. 38, 481-493.

Kokal, S., 2005. Crude-oils emulsion: state-of-the-art review. SPE production and facilities. 20, 5-13.

Komosawa, I., Otake, T., Kamojima, M., 1980. Wake behaviour and its effect on interaction between spherical-cap bubbles. J. Chem. Eng. Japan. 13, 103-109.

Konno, M., Arai, K., Saito, S., 1983. Scale effect on breakup process in liquid-liquid agitated tanks. J. Chem. Eng. Jpn. 16, 312-319.

Korovessi, E., Linninger, A. A., 2005. Batch processes. Book, CRC/Taylor and Francis Group. NW. USA.

Kostoglou, M., Karabelas, A. J., 2007. On the breakage of liquid-liquid dispersions in turbulent pipe flow: Spatial patterns of breakage intensity. J. Ind. Eng. Chem. Res. 46, 8220-8228.

Kumar, S., Kumar, R., Gandhi, K. S., 1991. Alternative mechanisms of drop breakage in stirred vessels. Chem. Eng. Science J. 46(10), 2483-2489.

Kumar, S., Ramkrishna, D., 1997. On the solution of population balance equations by discretization-III. Nucleation, growth and aggregation of particles. J. Chem. Eng. Science. 52, 4659 – 4679.

Kumar, J., Warnecke, G., Peglow, M., Tsotsas, E., 2008. A note on sectional and finite volume methods for solving population balance equations. Micro-Macro-Interactions in structured media and particle systems. Editors: Bertram, A., Tomas, J. Springer.

Lane, G. L., Schwarz, M. P., Evans, G. M., 2005. Numerical modelling of gas-liquid flow in stirred tanks. J. Chem. Eng. Science. 60, 2203-2214.

Lasheras, J. C., Eastwood, C., Martinez-Bazan, C., Montanes, J. L., 2002. A review of statistical models for the break-up and immiscible fluid immersed into a fully developed turbulent flow. Int. J. Multiphase Flow. 28, 247-278.

Lee, C. H., Erickson, L. E., Glasgow, L. A., 1987. Bubble breakup and coalescence in turbulent gas-liquid dispersions. J. Chem. Eng. Comm. 59, 65-84.

Lee, J. C., Hodgson, T. D., 1968. Film flow and coalescence – I. Basic relation, film shape and criteria for interface mobility. Chem. Eng. Science. 23, 1375-1387.

Lehr, F., Mewes, D., 1999. A transport equation for the interfacial area density in two-phase flow. In: Second European Congress of Chemical Engineering, October 5-7, Montpellier, France.

Lehr, F., Millies, M., Mewes, D., 2002. Bubble-size distributions and flow fields in bubble columns. AIChE J. 48, 2426-2443.

Levich, V. G., 1962. Physiochemical hydrodynamics. Prentice Hall, Eaglewood Cliffs, NJ.

Liao, Y., Lucas, D., 2009. A literature review of theoretical models for drop and bubble breakup in turbulent dispersions. J. Chem. Eng. Sci. 64, 3389-3406.

Liao, Y., Lucas, D., 2010. A literature review on mechanism and models for the coalescence process of fluid particles. J. Chem. Eng. Sci. 65, 2851-2864.

Liao, Y., Rzehak, R., Lucas, D., Krepper, E., 2015. Baseline closure model for dispersed bubbly flow: bubble coalescence and breakup. Chem. Eng. Science. 122, 336-349.

Lim, Y. I., Le Lann, J. M., Meyer, X. M., Joulia, X., Lee, G., Yoon, E. S., 2002. On the solution of population balance equations (PBE) with accurate front tracking methods in practical crystallization processes. J. Chem. Eng. Sci. 57, 3715−3732.

Liu, S., Li, D., 1999. Drop coalescence in turbulent dispersion. J. Chemical Engineering Sci. 54, 5667-5675.

Lovick, J., Angeli, P., 2004. Droplet size and velocity profiles in liquid-liquid horizontal flows. J. Chemical Engineering Science. 59, 3105-3115.

Luo, H., 1993. Coalescence, breakup and liquid circulation in bubble column reactors. Ph.D. Dissertation. Norwegian university of science and technology. Norway.

Luo, H., Svendsen, H. F., 1996. Theoretical model for drop and bubble breakup in turbulent dispersions. AIChE J. 42(5), 1225- 1233.

Luo, H., Svendsen, H. F., 1996b. Modeling and simulation of binary approach by energy conversation analysis. J. Chem. Eng. Communications. 145(1), 145-153.

Maaß, S., Gäbler, A., Zaccone, A., Paschedag, A. R., Kraume, M., 2007. Experimental investigations and modeling of breakage phenomena in stirred liquid-liquid systems. Chem. Eng. Res. Des. 85, 703-709.

Maaß, S., Wollny, S., Voigt, A., Kraume, M., 2011. Experimental comparison of measurement techniques for drop size distributions in liquid/liquid dispersions. J. Exp. Fluids. 50, 259-269.

Maaß, S., Paul, N., Kraume, M., 2012. Influence of the dispersed phase fraction on experimental and predicted drop size distributions in breakage dominated stirred systems. J. Chem. Eng. Science. 76, 140-153.

Maaß, S., Kraume, M., 2012. Determination of breakage rates using single drop experiments. J. Chem. Eng. Science. 70, 146-164.

Maaß, S., Wollny, S., Voigt, A., Kraume, M., 2011. Experimental comparison of measurement techniques for drop size distributions in liquid/liquid dispersions. J. Exp. Fluids. 50, 259-269.

Marchisio, D. L., Fox, R. O., 2005. Solution of population balance equations using the direct quadrature method of moments. J. Aerosol Sci. 36, 43-73.

Martínez-Bazán, C., Montañés, J. L., Lasheras, J. C., 1999. On the breakup of an air bubble injected into a fully developed turbulent flow. J. Fluid Mech. 401, 157-182.

McGraw, R., 1997. Description of Aerosol Dynamics by the Quadrature Method of Moments. Aerosol Sci. Technol. 27, 255-265.

Mesbah, A., Kramer, H. J. M., Huesman, A. E. M., Van den Hof, P. M. J., 2009. A control-oriented study on the numerical solution of the population balance equation for crystallization processes. J. Chem. Eng. Science. 64, 4262-4277.

Naeeni, S. K., Pakzad, L., 2019. Experimental and numerical investigation on mixing of dilute oil in water dispersions in a stirred tank. J. Chem. Eng. Research and Design. 147, 493-509.

Narsimhan, G., 2004. Model for drop coalescence in a locally isotropic turbulent flow field. J Colloid Interface Sci. 272,197–209

Narsimhan, G., Gupta, J.P., Ramkrishna, D., 1979. A model for transitional breakage probability of droplets in agitated lean liquid-liquid dispersions. J. Chem. Eng. Sci. 34, 257-265.

Narsimhan, G., Ramkrishna, D., and Gupta, J.P., 1980. Analysis of drop size distributions in lean liquid-liquid dispersions. AIChE Journal. 26, 991-1000.

Nere, N. K., Ramkrishna, D., 2005. Evolution of drop size distributions in fully developed turbulent pipe flow of a liquid-liquid dispersion by breakage. Ind. Eng. Chem. Res. 44, 1187-1193.

Nere, N. K., Ramkrishna, D., 2006. Solution of population balance equation with pure aggregation in developed turbulent pipe flow. J. Chem. Eng. Science. 61, 96-103.

Nguyen, T. T., Laurent, F., Fox, R., Massot, M., 2016. Solution of population balance equations in applications with fine particles: mathematical modeling and numerical schemes. J. Comp. Physics. 325, 129-156.

Oolman, T. O., Blanch, H. W., 1986. Bubble coalescence in stagnant liquids. Chemical Engineering Communications. 43, 237-261.

Omar, H. M., Rohani, S., 2017. Crystal population balance formulation and solution methods: a review. J. Crystal growth and design. ACS publications. 17(7), 4028-4041.

Opedal, N. V. D. T., Sørland, G., Sjöblom, J., 2009. Methods for droplet size distribution determination of water-in-oil emulsions using low-field NMR. J. Basic Principles of Diff. Theory, Exp. App. 9(7), 1-29.

Orrego, D. F., Arias, W., Lopez, D., Velasquez, H., 2012. Experimental and CFD study of a single-phase cone-shaped helical coiled heat exchanger: an empirical correlation. Proceedings of the International conference on efficiency, cost, optimization, simulation, and environmental impact of energy systems, Perugia, Italy.

Otsubo, Y., Prud'homme, R. K., 1994. Effect of drop size distribution on the flow behaviour of oil-in-water emulsions. Rheol. Acta J. 33(4), 303-306.

Pal, R., 1996. Effect of droplet size on the rheology of emulsions. AIChE J. 42(11), 3181-3190.

Pal, R., Rhodes, E., 1989. Viscosity/concentration relationship for emulsions. Journal of Rheology. 33, 1021-1045.

Park, J. Y., Blair, L. M., 1975. The effect of coalescence on drop size distribution in an agitated liquid-liquid dispersion. J. Chem. Eng. Science. 30, 1057-1064.

Piela, K., Delfos, R., Ooms, G., Westerweel, J., Oliemans, R. V. A., Mudde, R. F., 2006. Experimental investigation of phase inversion in oil-water flow through a horizontal pipe. Int. J. Multiphase Flow. 32, 1087-1099.

Pinar, Z., Dutta, A., Bény, G., Öziş, T., 2015. Analytical solution of population balance equation involving growth, nucleation and aggregation in terms of auxiliary equation method. J. Applied Math. Info. Sciences. 9(5), 2467-2475.

Plasencia, J. 2013. Experimental study on two phase oil-water dispersed flow. Ph.D. Dissertation. Norwegian university of science and technology. Norway.

Prince, M. J., Blanch, H. W., 1990. Bubble coalescence and break-up in air-sparged bubble columns. AIChE J. 36()10, 1485-1499.

Prince, M. J., Walters, S., Blanch, H. W., 1989. Bubble break-up in air-sparged biochemical reactors. In first generation of bioprocess engineering. Edited by Ghose, T.K.

Pumir, A., Wilkinson, M., 2016. Collisional aggregation due to turbulence. Annual review of condensed matter physics. 7, 141-170.

Qamar, S., Wernecke, G., 2007. Numerical solution of population balance equations for nucleation, growth and aggregation processes. J. Comp. Chem. Eng. 31, 1576-1589.

Raikar, N. B., Bhatia, S. R., Malone, M. F., McClements, D. J., Almeida-Rivera, C., Bongers, P., Henson, A. M., 2010. Prediction of emulsion drop size distributions with population balance equation models of multiple drop breakage. J. Colloids and Surfaces A: Physicochemical and Eng. Aspects. 361, 96-108.

Raikar, N. B., Bhatia, S. R., Malone, M. F., Henson, M. A., 2009. Experimental studies and population balance equation models for breakage prediction of emulsion drop size distributions. J. Chem. Eng. Science. 64, 2433-2447.

Raikar, N. B., 2010. Prediction and manipulation of drop size distribution of emulsions using population balance equation models for high pressure homogenization. PhD Thesis. University of Massachusetts, U.S.A.

Ramkrishna, D. 1985. The status of population balances. Reviews for chemical engineering. 3(1), 49-95.

Ramkrishna, D. 2000. Population Balances: Theory and Applications to Particulate Processes in Engineering. Academic Press, New York, NY.

Ramkrishna, D., Singh, M. R., 2014. Population balance modeling: current status and future prospects. Annu. Rev. Chem. Biomol. Eng. J. 5, 123-146.

Ramadhan, H., Umar, Z., Sarieddine, M., Salama, G., Fahes, M., Nasrabadi, H., Manson, S., Haouche, M., Cheneviere, P., 2012. Study of oil/water emulsions in horizontal pipes. Vol. EEP59, Qatar foundation annual research forum proceedings.

Randolph, A. D., 1964. A population balance for countable entities. Can. J. Chem. Eng. 42(6), 280–281.

Randolph, A.D., 1969. Effect of crystal breakage on crystal size distribution in a mixed suspension crystallizer. Ind. Eng. Chem. Fund. 8, 58-63.

Randolph, A. D., Larson, M. A., 1988. Population balances: theory of particulate processes. 2nd edition. Analysis and techniques of continuous crystallization. Academic Press, San Diego.

Rehman, S. M., Qamar, S., 2014. Application of the method of characteristics to population balance models considering growth and nucleation phenomena. J. Applied mathematics. 5, 1853-1862.

Ribeiro, M. M., Regueiras, P. F., Guimarães, M. M. L., Madureira, C. M. N., Cruz_Pinto, J. J. C., 2011. Optimization of breakage and coalescence model parameters in a steady-state batch agitated dispersion. Ind. Eng. Chem. Res. 50, 2182-2191.

Rigopoulos, S., 2010. Population balance modelling of polydispersed particles in reactive flows. J. Process in Energy and Combust. Science. 36, 412-443.

Rigopoulos, S., Jones, A. G., 2003. Finite element scheme for solution of the dynamic population balance equation. A.I.Ch.E. Journal. (49),1127–1139.

Saboni, A., Gourdon, C., Chesters, A. K., 1995. Drainage and rupture of partially mobile films during coalescence in liquid-liquid systems under a constant interaction force. J. Colloid and Interface Science. 175, 27-35.

Salomon, D., 2011. The computer graphics manual. Springer, London, UK.

Sagert, N. H., Quinn, M. J., 1979. The coalescence of H2S and CO2 bubble in water. Canadian J. Chem. Eng. 54, 392-398.

Sajjadi, B., Abdul Raman, A. A., Raja Ehsan Shah, R. S., Ibrahim, S., 2013. Review on applicable breakup/coalescence models in turbulent liquid-liquid flows. Rev. Chem. Eng. J. 29(3), 131-158.

Schramm, L. L. 1992. Petroleum Emulsions: Basic Principles in Emulsions: Fundamentals and Applications in the Petroleum Industry. American Chemical Society, Washington, DC.

Schümann, H., Khatibi, M., Tutkun, M., Pettersen, B. H., Yang, Z., Nydal, O. J., 2015. Droplet size measurements in oil-water dispersions: A comparison study using FBRM and PVM. J. of Dispersion Science and Tech. 1-45.

Schümann, H., 2016. Experimental investigation of transitional oil-water pipe flow. PhD thesis. Norwegian university of science and technology (NTNU), Norway.

Schwartzberg, H., Treybal, R. E., 1968. Fluid and particle motion in turbulent stirred tanks. Ind. Eng. Chem. Fundamen. 7(1), 1-6.

Simon, M., 2004. Koaleszenz von tropfen und tropfenschwärmen. Ph. D. Dissertation. Technischen Universität Kaiserslautern. Germany.

Singh, P. N., Ramkrishna, D., 1977. Solution of population balance equations by MWR. J. Comp. Chem. Eng. 1, 23-31.

Solsvik, J., Jakobsen, H. A., 2014. Bubble coalescence modeling in the population balance framework. J. Dispersion Science and Tech. 35(11), 1626-1642.

Solsvik, J., Jakobsen, H. A., 2015. The foundation of the population balance equation: a review. J. Dispersion Science and Tech. 36, 510-520.

Solsvik, J., Becker, P. J., Sheibat-Othman, N., Mohallick, I., Farzad, R., Jakobsen, H., 2015. Viscous drop breakage in liquid-liquid stirred dispersions: population balance modeling. J. Dispersion Science and Technol. 36(4), 577-594.

Solsvik, J., Borka, Z., Becker, P. J., Sheibat-Othman, N., Jakobsen, H., 2014. Evaluation of breakage kernels for liquid-liquid systems: solution of the population balance equation by the least-square method. Canadian. J. Chem. Eng. 92, 234-249.

Solsvik, J., Tangen, S., Jakobsen, H., 2013. On the constitutive equations for fluid particle breakage. J. Rev. Chem. Eng. 29(5). 241-356.

Solsvik, J., Jakobsen, H. A., 2016. A review of the statistical turbulence theory required extending the population balance closure models to the entire spectrum of turbulence. AIChE. J. 62(5), 1795-1820.

Solsvik, J., Skjervold, V. T., Jakobsen, H. A., 2017. A bubble breakage model for finite Reynolds number flows. J. Dispersion Science and Tech. 38(7), 973-978.

Søntvedt, T., Valle, A., 1994. Capacities of troll oil flow lines with high water cuts. Predictions based upon recorded pipe flow friction factors for stable troll oil dispersions. Report no. R-068557, Norsk Hydro ASA. Norway.

Sovova, H., 1981. Breakage and coalescence of drops in a batch stirred vessel II comparison of model and experiment. J. Chem. Eng. Science. 36(9), 1567-1573.

Tsouris, C., Tavlarides, L. L., 1994. Breakage and coalescence models for drops in turbulent dispersions. AIChE Journal. 40(3), 395-406.

Tsouris, C., Tavlarides, L. L., 2013. Fluid mechanics of mixing: modelling, operations, and experimental techniques. Modelling and control of multistage mixer extractors. Bokk edited by King, R. Springer science and business media.

Valentas, K.J., Bilous, O., Amundson, N.R., 1966. Analysis of breakage in dispersed phase systems. I&EC Fundam. 5, 271 – 279.

Valentas, K. J., Amundson, N. R., 1966. Breakage and coalescence in dispersed phase systems. Ind. Eng. Chem. Fundamen. 5(4), 533-542.

Vankova, N., Tcholakova, S., Denkov, N. D., Vulchev, V. D., Danner, T., 2007. Emulsification in turbulent flow 2. Breakage rate constants. J. Colloid and Interface Science. 313, 612-629.

Vay, K., Frieß, W., Scheler, S., 2012. Understanding reflection behavior as a key for interpreting complex signals in FBRM monitoring of microparticle preparation processes. Int. J. Pharmaceutics. 437, 1-10.

Von Smoluchowski, M., 1917.Versuch einer mathematischen theorie der Koagulationskinetik kolloider Lösungen. Z. Phys. Chem. 92, 129–68.

Villermaux, E., 2007. Fragmentation. J. Annual review fluid mechanics. 39, 419-446.

Vikas, V., Wang, Z. J., Fox, R. O., 2013. Realizable high-order finite-volume schemes for quadrature-based moment methods applied to diffusion population balance equations, J. Computational Physics. 249, 162-179.

Venneker, B. C. H., Derksen, J. J., Van Den Akker, H. E. A., 2002. Population balance modeling of aerated stirred vessels based on CFD. AIChE J. 48(4), 673-685.

Vuong, D. H., Zhang, H. Q., Li, M., 2009. Experimental study on high viscosity oil/water flow in horizontal and vertical pipes. In: SPE-124542-MS-P, SPE Annual Technical Conference and Exhibition held in New Orleans, LA, U.S.A.

Wang, T., Wang, J., Jin, Y., 2005. Population balance model for gas-liquid flows: influence of bubble coalescence and breakup models. Ind. Eng. Chem. Res. 44, 7540-7549.

Wang, G., Yang, F., Wu, K., Ma, Y., Peng, C., Liu, T., Wang, L.P., 2020. Estimation of the dissipation rate of turbulent kinetic energy: a review. J. Chem. Eng. Science. 229, 116-133.

Worlitschek, J., Buhr, J., 2005. Crystallization studies with focused beam reflectance measurement and multimax. Application note. Mettler Toledo GmbH, AutoChem.

Yeoh, G. H., Cheung, C. P., Tu, J., 2014. Multiphase flow analysis using population balance modeling. Book, Elsevier Ltd. UK.

Yuan, C., Laurent, F., Fox, R. O., 2012. An extended quadrature method of moments for population balance equations. J. Aerosol Sci. 51, 1−23.

Yu, G. Z., Mao, Z. S., 2004. Sedimentation and coalescence profiles in liquid-liquid batch settling experiments. Chem. Eng. Tech. 27, 407-413.

Zhang, J., Xu, S., Li, W., 2012. High shear mixers: A review of typical applications and studies on power draw, flow pattern, energy dissipation and transfer properties. J. Chem. Eng. and Processing. 57-58, 25-41.

Zhu, Z., Dorao, C. A., Jakobsen, H. A., 2008. A least-squares method with direct minimization for the solution of the breakage–coalescence population balance equation. J. Math. Computers. Sim. 79, 716-727.

APPENDIX A

DIMENSIONLESS ANALYSIS

A1 Dimensionless analysis

In order to transform the system equations into dimensionless form, five dimensionless variables are introduced for the equations. These include dimensionless axial position in the pipe, dimensionless radius of droplet, dimensionless drop volume, and dimensionless number as well as volume number density distributions. For the scaling purposes, a characteristic length and velocity are defined to transform the model into a dimensionless form. In this respect, the characteristic length of the axial coordinate of the pipe (external coordinate) is described as the total length of the pipe, L, and the characteristic velocity of the system is defined as the average velocity in the pipe, U. On the other hand, the characteristic radius in the scaling process is given by R_{max} which describe the maximum size of drop radius in the system. From the definitions above, the scaling relationships can be expressed as follows:

A1.1 Dimensionless variables:

(a) Dimensionless axial position in the pipe:

$$\lambda = \frac{z}{L} \tag{1a}$$

(b) Dimensionless radius (droplet):

$$\xi = \frac{r}{R_{max}} \tag{2a}$$

(c) Dimensionless drop volume:

$$\bar{v} = \frac{4}{3}\pi r^3 = \left(\frac{4}{3}\pi R_{max}^3\right)\xi^3 = V_{max}\xi^3 \qquad (3a)$$

The number density distribution $\overline{f_n}$ can be scaled from the definition of initial number density distribution, N_{d0} at the initial position in pipe ($z = 0$) as follows:

$$N_{d0}(z) = \int_0^{R_{max}} f_{n_0}(r', z)dr' \qquad (4a)$$

(d) Dimensionless number density distribution:

$$\overline{f_n} = \frac{R_{max}}{N_{d0}} f_n \qquad (5a)$$

(e) Dimensionless volume density distribution:

$$\overline{f_v} = R_{max}.f_v \qquad (6a)$$

Hence, from Eqn. (6a), the dimensionless number density distribution can be formulated in terms of dimensionless volume density distribution as follows:

$$\overline{f_n} = \frac{\overline{f_v}}{N_{d0}V_{max}\xi^3} \qquad (7a)$$

A2 Dimensionless population balance equation

Dimensionless population balance equation (droplet transport equation) is given by:

$$\frac{\partial \bar{f}_v(\xi,\lambda)}{\partial \lambda} = \left[\bar{v}P_{C_b}(\xi,\lambda) - P_{C_d}(\xi,\lambda) + \bar{v}P_{B_b}(\xi,\lambda) - P_{B_d}(\xi,\lambda)\right] \quad (8a)$$

The dimensionless PBE above is valid under condition of, $0 \le \lambda \le 1,\ 0 \le \xi \le 1$

The initial condition is given by:

At $\lambda = 0, \quad \bar{f}_v(\xi,0) = \bar{f}_{v_0}(\xi), \quad$ for $0 \le \xi \le 1$

In the Eqn. (8a) above, P_{C_b} and P_{C_d} represent the dimensionless birth and death rates due to coalescence respectively, while, P_{B_b} and P_{B_d} are the dimensionless birth and death rates due to breakage, respectively.

A3 Dimensionless coalescence birth and death rates

The dimensionless coalescence birth and death rates can be written as:

$$P_{C_b}(\xi,\lambda) = \xi^3 \int_0^{\xi/\sqrt[3]{2}} \bar{r}_c\left(\xi', \left[\xi^3 - \xi'^3\right]^{1/3}\right) \frac{1}{\bar{v}'} \bar{f}_v(\xi',\lambda) \frac{1}{\bar{v}''} \bar{f}_v\left(\left[\xi^3 - \xi'^3\right]^{1/3}, \lambda\right) \frac{\xi^2}{\xi''^2} d\xi' \quad (9a)$$

$$P_{C_d}(\xi,\lambda) = \bar{f}_v(\xi,\lambda) \int_0^1 \bar{r}_c(\xi,\xi') \frac{1}{\bar{v}'} \bar{f}_v(\xi',\lambda)\, d\xi' \quad (10a)$$

Where, dimensionless rate of coalescence is given as:

$$\bar{r}_c(\xi', \xi'') = \bar{\omega}_c(\xi', \xi'')\bar{\psi}_e(\xi', \xi'') \tag{11a}$$

By substituting the expression for $\bar{\omega}_c(\xi', \xi'')$ and $\bar{\psi}_e(\xi', \xi'')$ into Eqn. (11a), dimensionless rate of coalescence $\bar{r}_c(\xi', \xi'')$ can be written in details as follows:

$$\bar{r}_c(\xi', \xi'') = \chi_w(\xi' + \xi'')^2\left[\xi'^{2/3} + \xi''^{2/3}\right]^{1/2} exp\left[-\chi_\psi\left(\frac{1}{2\left(\frac{1}{\xi'} + \frac{1}{\xi''}\right)}\right)^{5/6}\right] \tag{12a}$$

Where χ_w and χ_ψ are dimensionless parameters and can be expressed as follows:

$$\chi_w = k_w \frac{4\sqrt[3]{2}\varepsilon^{1/3}R_{max}^{7/3}N_{d0}L}{U}\ (V_{max}.N_{d0}) \tag{13a}$$

$$\chi_\psi = k_\psi \frac{{\rho_c}^{1/2}\varepsilon^{1/3}R_{max}^{5/6}}{2^{1/6}\sigma^{1/2}} \tag{14a}$$

A4 Dimensionless breakage birth and death rates

The dimensionless breakage birth and death rates can be written as:

$$P_{B_b}(\xi, \lambda) = \xi^3 \int_{\xi}^{1} 2\bar{\beta}\,(\xi, \xi')\bar{g}(\xi')\frac{1}{\bar{v}}\bar{f}_v(\xi', \lambda)\,d\xi' \tag{15a}$$

$$P_{B_d}(\xi,\lambda) = \left[\bar{g}(\xi)\,\bar{f}_v\,(\xi,\lambda)\right] \tag{16a}$$

In Eqns. (15a) and (16a), the dimensionless rate of breakage, $\bar{g}(r)$ and dimensionless daughter size distribution, $\bar{\beta}(r,r')$ can be expressed as follows;

$$\bar{g}(r) = \chi_{g1}\frac{1}{\xi^{2/3}}exp\left[-\chi_{g2}\frac{1}{\varepsilon^{5/3}}\right] \tag{17a}$$

$$\bar{\beta}(r,r') = 7.2\,\frac{\xi^2}{\xi'^3}exp\left[-4.5\frac{\left(\xi^3-\xi'^3\right)^2}{\xi'^6}\right] \tag{18a}$$

Where χ_{g1} and χ_{g2} are dimensionless parameters and can be written as follows:

$$\chi_{g1} = k_{g1}\frac{\varepsilon^{1/3}L}{R_{max}^{2/3}(1+\phi)U} \tag{19a}$$

$$\chi_{g2} = k_{g2}\frac{\gamma(1+\phi)^2}{\rho_d\varepsilon^{2/3}R_{max}^{5/3}} \tag{20a}$$

In Eqns. (13a) and (14a), the expression of χ_w represents the ratio of the residence time for a drop in the pipe to the average time between droplet collisions. While the expression of χ_ψ indicates the ratio of the film drainage time constant to the droplet contact time constant. Whereas, in Eqns. (19a) and (20a), the expression of χ_{g1} represents a comparison of the droplet residence time in the pipe to the breakage time (frequency) of the drop in the turbulent flow field. While, χ_{g2} signifies the ratio of the surface energy of the drop to the mean turbulent kinetic energy in an eddy.

Substitute all the equations above for dimensionless coalescence and breakage processes into the general equation shown in Eqn. (8a). Hence, the complete expression of dimensionless population balance equation in terms of volume density distribution can be written as follows:

$$\frac{\partial \bar{f}_v(\xi,\lambda)}{\partial \lambda} = \xi^3 \int_0^{\xi/\sqrt[3]{2}} \frac{\xi^2}{\xi''^2} \bar{r}_c\left(\xi', \left[\xi^3 - \xi'^3\right]^{1/3}\right) \frac{1}{\bar{v}'} \bar{f}_v(\xi',\lambda) \frac{1}{\bar{v}''} \bar{f}_v\left(\left[\xi^3 - \xi'^3\right]^{1/3}, \lambda\right) d\xi'$$

$$- \bar{f}_v(\xi,\lambda) \int_0^1 \bar{r}_c(\xi,\xi') \frac{1}{\bar{v}'} \bar{f}_v(\xi',\lambda)\, d\xi' + \xi^3 \int_\xi^1 2\bar{\beta}(\xi,\xi') \bar{g}(\xi') \frac{1}{\bar{v}'} \bar{f}_v(\xi',\lambda)\, d\xi'$$

$$- \left[\bar{g}(\xi)\, \bar{f}_v(\xi,\lambda)\right] \qquad (21a)$$

A5 Normalized number density, $\overline{N_d}(\lambda)$ and dimensionless volume fraction, $\phi(\lambda)$

$$\overline{N_d}(\lambda) = \frac{N_d(\lambda)}{N_{d0}} = \int_0^1 \bar{f}_n(\xi',\lambda)\, d\xi' = \int_0^1 \frac{\bar{f}_v}{\bar{v}'}(\xi',\lambda)\, d\xi' \qquad (22a)$$

$$\phi(\lambda) = N_{d0} V_{max} \int_0^1 \xi'^3 \bar{f}_n(\xi',\lambda)\, d\xi' = \int_0^1 \bar{f}_v(\xi',\lambda)\, d\xi' \qquad (23a)$$

A6 Dimensionless mean drop radii $\bar{\mu}_N$ and $\bar{\mu}_V$

$$\bar{\mu}_N(\lambda) = \frac{R_{max}}{\overline{N_d}(\lambda)} \int_0^1 \xi' \bar{f}_n(\xi',\lambda)\, d\xi' = \frac{R_{max}}{\overline{N_d}(\lambda)} \int_0^1 \xi' \frac{\bar{f}_v}{\bar{v}'}(\xi',\lambda)\, d\xi' \qquad (24a)$$

$$\bar{\mu}_V(\lambda) = R_{max}\frac{N_{d0}}{\phi(\lambda)}V_{max}\int_0^1 \xi'^4 \bar{f}_n(\xi',\lambda)\, d\xi' = \frac{R_{max}}{\phi(\lambda)}\int_0^1 \xi' \bar{f}_v(\xi',\lambda)\, d\xi' \quad (25a)$$

A7 Dimensionless standard deviation number, $\bar{\sigma}_N$ and volume distributions, $\bar{\sigma}_V$

$$\bar{\sigma}_N(\lambda) = \sqrt{\frac{R_{max}^2}{\overline{N_d}(\lambda)}\int_0^1 \left(\xi' - \frac{\bar{\mu}_N}{R_{max}}\right)^2 \bar{f}_n(\xi',\lambda)\, d\xi'}$$

$$= \sqrt{\frac{R_{max}^2}{\overline{N_d}(\lambda)}\int_0^1 \left(\xi' - \frac{\bar{\mu}_N}{R_{max}}\right)^2 \frac{\bar{f}_v}{\bar{v}'}(\xi',\lambda)\, d\xi'} \quad (26a)$$

$$\bar{\sigma}_V(\lambda) = \sqrt{R_{max}^2\frac{N_{d0}}{\phi(\lambda)}V_{max}\int_0^1 \left(\xi' - \frac{\bar{\mu}_V}{R_{max}}\right)^2 \xi'^3 \bar{f}_n(\xi',\lambda)\, d\xi'}$$

$$= \sqrt{\frac{R_{max}^2}{\phi(\lambda)}\int_0^1 \left(\xi' - \frac{\bar{\mu}_V}{R_{max}}\right)^2 \bar{f}_v(\xi',\lambda)\, d\xi'} \quad (27a)$$

Apart from that, mass balance is also calculated to ensure that there are no droplets entering or leaving the system during the simulation. This is crucial for the system to warrant the mass remains conserve throughout the pipe lengths. The mass balance is determined by taking into account the mass created and the mass disappeared from the coalescence and breakage processes so that the condition is met for the following expressions:

$$P_{C_b}(\xi,\lambda) - P_{C_d}(\xi,\lambda) = 0 \quad (28a)$$

$$P_{B_b}(\xi,\lambda) - P_{B_d}(\xi,\lambda) = 0 \tag{29a}$$

The ratio of the coalescence mass balance M_C is determined by dividing the dimensionless volume integral for coalescence birth rate, P_{C_b} against the dimensionless coalescence loss rate, P_{C_b}. The same method applied to calculate the breakage mass balance, M_B and both ratios can be written as follows:

$$M_C = \frac{P_{C_b}(\xi,\lambda)}{P_{C_d}(\xi,\lambda)} \tag{30a}$$

$$M_B = \frac{P_{B_b}(\xi,\lambda)}{P_{B_d}(\xi,\lambda)} \tag{31a}$$

To ensure that the local volume fraction, ϕ remains constant, the mass balance ratio for both coalescence and breakage, M_C and M_B are multiplied by the dimensionless coalescence and breakage birth rates, P_{C_b} and P_{B_b} respectively, as written below:

$$P_{C_b} = P_{C_b} \times M_C \tag{32a}$$

$$P_{B_b} = P_{B_b} \times M_B \tag{33a}$$

APPENDIX B
(1st MANUSCRIPT)

This paper is awaiting publication and is not included in NTNU Open

APPENDIX C
(2nd MANUSCRIPT)

This paper is awaiting publication and is not included in NTNU Open

APPENDIX D
(3rd MANUSCRIPT)

This paper is awaiting publication and is not included in NTNU Open

ISBN 978-82-326-5407-9 (printed ver.)
ISBN 978-82-326-5403-1 (electronic ver.)
ISSN 1503-8181 (printed ver.)
ISSN 2703-8084 (online ver.)

NTNU

Norwegian University of
Science and Technology